Title	Development of a burst-tolerant spectrometer system for DeeMe experiment
Author(s)	長尾, 大樹
Citation	大阪大学, 2024, 博士論文
Version Type	VoR
URL	https://doi.org/10.18910/98711
rights	
Note	

Development of a burst-tolerant spectrometer system for DeeMe experiment

Osaka University
Daiki Nagao

3 September, 2024

Abstract

In the Standard Model (SM) of particle physics, the lepton family number is conserved in initial and final state. The lepton flavor violation of neutrino (neutrino oscillation) was observed by the Super Kamiokande experiment. However, the charged lepton flavor violation (cLFV) is still limited by $O(10^{-54})$ taking into account the neutrino oscillation. On the other hand, some theoretical models beyond the SM predict the μ-e conversion ($\mu + N \rightarrow e + N$), one of the cLFV, with the branching ratio $O(10^{-14})$.

DeeMe is an experiment to search the μ-e conversion at J-PARC Material and Life Science Experimental Facility (MLF). In this experiment, a muon production target made of graphite in MLF is also utilized as the muon stopping target. The single event sensitivity of DeeMe with the graphite target is aimed to be $O(10^{-13})$ for 1 year and $O(10^{-14})$ for 4 years. The μ-e electron has monochromatic energy $E_{\mu e} = 105.06$ MeV and lifetime $\tau = 2.0$ μs for muonic C atom. The secondary beamline (H-Line) in MLF muon section derives the electrons around $E_{\mu e}$ from the muon production target directly, so that the prompt-burst electrons also achieve and saturate DeeMe's detectors. In order to avoid saturation of the detectors, we had constructed burst-tolerant MWPCs and developed data acquisition system and analysis tools for our burst-tolerant spectrometer.

In June 2017, we had the performance test of the MWPCs to utilize as a spectrometer including the DAQ system at J-PARC MLF D-Line. The muon beam was stopped in a stopping target and the momentum of the electrons decayed from the muonic atom in the target were observed by the spectrometer. In this performance test, we obtained Michel spectrum with μ^+ for calibration and decay-in-orbit spectrum from graphite target with μ^- by a measurement. As a preparation for μ-e conversion measurement at H-Line, we developed the analysis framework for our spectrometer by using the real data of well-known momentum spectrum of muon decay. In this thesis, this experiment and analysis framework development with real data will be described.

Acknowledgements

Contents

List of Figures

6

8

9

11

12

List of Tables

Chapter 1

Introduction

1.1 The Standard Model of particle physics

The aim of particle physics is to find the fundamental rule of matter and forces. The Standard Model (SM) is the model most successful theory in particle physics. According to the SM, the elementary particles with spin 1/2, fermions, composing materials are six quarks, six leptons, and their antimatters. On the other hand, the particles named gauge bossons mediate the fundamental forces (weak, strong, and electromagnetic).

1.1.1 Lepton family number

Leptons are classified by their charge and generation as shown in Table 1.1. The charged leptons are e^-, μ^-, and τ^- and their charge is $-e = -1.602 \times 10^{-19}$ C, where their anti-particles e^+, μ^+, and τ^+ have $+e = 1.602 \times 10^{-19}$ C. They have pair neutrinos, non-charged leptons, such as ν_e, ν_μ, and ν_τ. The lepton family numbers L_e, L_μ, and L_τ are defined for each generations and e^- and ν_e have $L_e = +1$. similarly, the pairs of μ^- and τ^- have $L_\mu = +1$ and $L_\tau = +1$, respectively. The anti-particles e^+, μ^+, τ^+,$\bar{\nu}_e$, $\bar{\nu}_\mu$, and $\bar{\nu}_\tau$ also have lepton family number $L_l = -1$ ($l=e$, μ, or τ). The family numbers L_l must be conserved in any reaction of elementary particles such as muon decay in vacuum $\mu^- \rightarrow e^- + \nu_\mu + \bar{\nu}_e$, according to the SM.

Table 1.1: Properties of leptons.

Spin	Charge	Generations		
		I	II	III
1/2	0	ν_e	ν_μ	ν_τ
1/2	-1	e	μ	τ

1.1.2 Neutrino oscillation

In 1998, neutrino oscillation had been observed in Super Kamiokande experiment. In neutrino oscillation process, lepton family number is not conserved.

The neutrinos ν_e, ν_μ, ν_τ are mixed states of mass eigenstates (ν_1, ν_2, ν_3). The mixing is denoted by using PMNS matrix U_{PMNS} [4][5] with three mixing angles $\theta_{12}, \theta_{23}, \theta_{13}$ and a phase angle δ_{CP}, which is related to the CP violation,

$$
\begin{pmatrix} \nu_e \\ \nu_\mu \\ \nu_\tau \end{pmatrix} = U_{\mathrm{PNMS}} \begin{pmatrix} \nu_1 \\ \nu_2 \\ \nu_3 \end{pmatrix}.
\tag{1.1}
$$

The matrix has 3×3 elements $U_{\alpha i}$ $(\alpha = e, \mu, \tau$ and $i = 1, 2, 3)$, which denoted as

$$
\begin{aligned}
U_{\mathrm{PMNS}} &= \begin{pmatrix} U_{e1} & U_{e2} & U_{e3} \\ U_{\mu 1} & U_{\mu 2} & U_{\mu 3} \\ U_{\tau 1} & U_{\tau 2} & U_{\tau 3} \end{pmatrix} \\
&= \begin{pmatrix} c_{12}c_{13} & s_{12}c_{13} & s_{13}e^{-i\delta_{\mathrm{CP}}} \\ -s_{12}c_{23} - c_{12}s_{13}s_{23}e^{-i\delta_{\mathrm{CP}}} & c_{12}c_{23} - s_{12}s_{13}s_{23}e^{-i\delta_{\mathrm{CP}}} & c_{13}s_{23} \\ s_{12}s_{23} - c_{12}s_{13}c_{23}e^{-i\delta_{\mathrm{CP}}} & -c_{12}s_{23} - s_{12}s_{13}c_{23}e^{-i\delta_{\mathrm{CP}}} & c_{13}c_{23} \end{pmatrix},
\end{aligned}
\tag{1.2}
$$

where c_{ij} and s_{ij} are $\cos\theta_{ij}$ and $\sin\theta_{ij}$ respectively. The probability of the neutrino oscillation $\nu_\alpha \to \nu_\beta$ is denoted as

$$
P(\nu_\alpha \to \nu_\beta) = \left| \sum_i U_{\beta i} U_{\alpha i}^* e^{-iE_i t} \right|^2,
\tag{1.3}
$$

where E_i is total energy of ν_i.

1.2 Charged Lepton Family number Violation

1.2.1 Muon LFV

The lepton flavor violation had been observed as the neutrino oscillation. However, charged Lepton Family number Violation (cLFV) is heavily suppressed in the SM yet. The cLFV is a clear evidence of new physics beyond the SM and cLFV in muon section is searched by many experiments. Major cLFV processes are $\mu \to e\gamma$, $\mu \to eee$, and μ-e conversion.

The branching ratio of $\mu \to e\gamma$ is [6][7][8]

$$B(\mu \to e\gamma) = \frac{3\alpha_e}{32\pi} \left| U_{e2}^* U_{\mu2} \frac{\Delta m_{21}^2}{M_W^2} + U_{e3}^* U_{\mu3} \frac{\Delta m_{31}^2}{M_W^2} \right|^2 \tag{1.4}$$

with considering the neutrino oscillation, where M_W is mass of weak boson, and Δm_{21}^2 and Δm_{31}^2 are the differences of neutrino mass squared

$$\Delta m_{21}^2 \quad = m_2^2 - m_1^2 = 7 \times 10^{-5} \text{eV}^2 \tag{1.5}$$

$$\Delta |m_{31}^2| \quad = |m_3^2 - m_1^2| = 2.5 \times 10^{-3} \text{eV}^2 \tag{1.6}$$

The branching ratio is calculated as $Br(\mu \to e\gamma) = O(10^{-54})$ in the SM [9].

However, several new physics models beyond the SM predict observable branching ratio such as supersymmetry (SUSY) [10]. According the SUSY theory, the "superpartner" particles of the elementally particles in the SM are defined such as "slepton" $\tilde{l}$ for lepton, "squark" $\tilde{q}$ for quark, "gauginos" $\tilde{B}$, $\tilde{W}$, $\tilde{G}$ for gauge bosons, and "higgsinos" $\tilde{H}$ for Higgs boson. Where the slepton and squark are scalar boson and gauginos and higgsinos are felmion with spin-1/2. The sleptons mixing mediated by off-diagonal elements of the slepton mass matrix leads muon cLFV.

1.2.2 μ-e conversion

The μ-e conversion process is decay of a trapped muon in a muonic atom without emitting neutrino.

$$\mu^- + N(A, Z) \to e^- + N(A, Z) \tag{1.7}$$

The emitted electron from μ-e conversion has mono-energy $E_{\mu e}$

$$E_{\mu e} = m_\mu - E_b - E_{\text{rec}} \tag{1.8}$$

where E_b is binding energy of muon in a nucleus and E_{rec} is recoil energy. $E_{\mu e}$ equals to 105.06 MeV for muonic C atom. The branching ratio $B_{\mu e}$ is defined as the ratio of the decay width of muon capture process ($\mu^- + N(A, Z) \rightarrow \nu_\mu + N(A, Z - 1)$),

$$B_{\mu e} = \frac{\Gamma(\mu^- + N(A, Z) \rightarrow e^- + N(A, Z))}{\Gamma(\mu^- + N(A, Z) \rightarrow \nu_\mu + N(A, Z - 1))}. \tag{1.9}$$

1.3   Experimental status

1.3.1 $\mu^+ \rightarrow e^+ \gamma$

For the $\mu \rightarrow e\gamma$ process, MEG experiment constructed at Paul Scherrer Institute (PSI) gives the current upper limit of the branching ratio $B(\mu \rightarrow e\gamma) < 4.2 \times 10^{-13}$ at 90% confidence level [11].

The physics run of MEG-II, upgrade experiment of MEG, run has started from 2021 and they reported the first result of the upper limit of the branching ratio $B(\mu \rightarrow e\gamma) < 7.5 \times 10^{-13}$ with the first run in 2021 and $B(\mu \rightarrow e\gamma) < 3.1 \times 10^{-13}$ with the combination of the result in 2021 and MEG [12]. They expect to obtain more than 20 times larger statistics until 2026.

1.3.2 $\mu^\pm \rightarrow e^\pm e^- e^+$

On $\mu^\pm \rightarrow e^\pm e^- e^+$, the current upper limit is set to 1.0×10^{-12} by SINDRUM experiment at PSI [13].

The Mu3e experiment is planned at PSI [14]. They aim to start the Phase I from 2025 with the sensitivity of 2×10^{-15} and the Phase II from 2029 with that of 10^{-16}.

1.3.3 μ-e conversion

The current upper limit of μ-e conversion is given by SINDRUM-II experiment at PSI at 7×10^{-13} for Au [15] and 4.3×10^{-12} for Ti [16]. The experiment at TRIUMF also gives a limit 4.3×10^{-12} for Ti [17].

For improving the sensitivity by order 1-3, several experiments have been proposed in J-PARC and Fermilab. COMET experiment at J-PARC has two experimental stage called Phase-I and Phase-II [18]. They expect the single event sensitivity of 3×10^{-15} in Phase-I, and 3×10^{-17} in Phase-II.

The muon beam produced by 8-GeV proton beam is lead to the stopping target by the transport solenoid and forms muonic atoms. Then the emitted electrons from the muonic atoms are observed by a cylindrical drift chamber. In the COMET experiment, aluminum will be used as the muon stopping target. They have finished the construction of the 8-GeV proton beam line and expect to start data taking in 2026.

Mu2e experiment at Fermilab is also parted in "Run 1" and "Run 2", and they aim to reach the single event sensitivity of 6×10^{-16} for Run 1 and $O(10^{-17})$ for Run 2 [19][20]. The muon stopping target is made of aluminum and their method to detect μ-e conversion electron is similar to COMET experiment. Their first scientific run is expected to start from 2025.

DeeMe experiment has been constructed in J-PARC and aims to reach the sensitivity of $O(10^{-13})$ for one year with graphite target. In DeeMe experiment, the muon production target works as the muon stopping target (detail in Chapter 2). The detector and the beamline have been completed in 2020. The commissioning for beamline and detector has started.

1.4   Muon Decay In Orbit

One of the most serious background for μ-e conversion experiment is the muon decay-in-orbit (DIO):

$$\mu^- + N \to e^- + \nu_\mu + \bar{\nu}_e + N. \tag{1.10}$$

Maximum momentum of the electron from free muon decay is 52.8 MeV/c, though the momentum of DIO electron from a muonic atom reaches to $E_{\mu e}$ as kinetic energy taken by neutrinos decreases. The momentum spectrum of DIO has been calculated theoretically by Watanabe [1], Shanker [21], and Czarnecki [22]. The shape of DIO electron momentum spectrum is proportional to $(E_\mu - E_e)^5$ at the end point.

1.4.1   Free muon decay

The Lagrangian density of the free muon decay ($\mu^- \to e^- + \bar{\nu}_e + \nu_\mu$) can be written as

$$\mathcal{L} = -\frac{G_\mu}{\sqrt{2}}[\bar{\nu}_\mu \gamma^\mu (1 - \gamma^5)\mu] \; [\bar{e}\gamma_\mu (1 - \gamma^5)\nu_e], \tag{1.11}$$

where $G_\mu = 1.1663788 \times 10^{-5}$ GeV^{-2} is the Fermi constant, $\bar{\nu}_\mu$, μ, $\bar{e}$ and ν_e are the wave functions of each particle. The decay rate of the free muon not polarized is

$$\frac{d\Gamma}{dx} = \frac{m_\mu}{4\pi^3} W_{e\mu}^4 G_F^2 \sqrt{x^2 - x_0^2} \left\{ x(1-x) + \frac{2}{9}\rho(4x^2 - 3x - x_0^2) + \eta x_0(1-x) \right\}, \quad (1.12)$$

where $W_{e\mu} = (m_\mu^2 + m_e^2)/(2m_\mu)$, $x = E_e/W_{e\mu}$, $x_0 = m_e/W_{e\mu}$ and ρ and η are called Michel parameters. In the SM, the Michel parameters are given as $\rho = 3/4$ and $\eta = 0$. The spectrum of this decay rate is shown in Figure 1.1. Integration of the Equation (1.12) over dx will give the total decay rate

$$\Gamma_0 = \frac{G_F^2 m_\mu^5}{192\pi^3}. \quad (1.13)$$
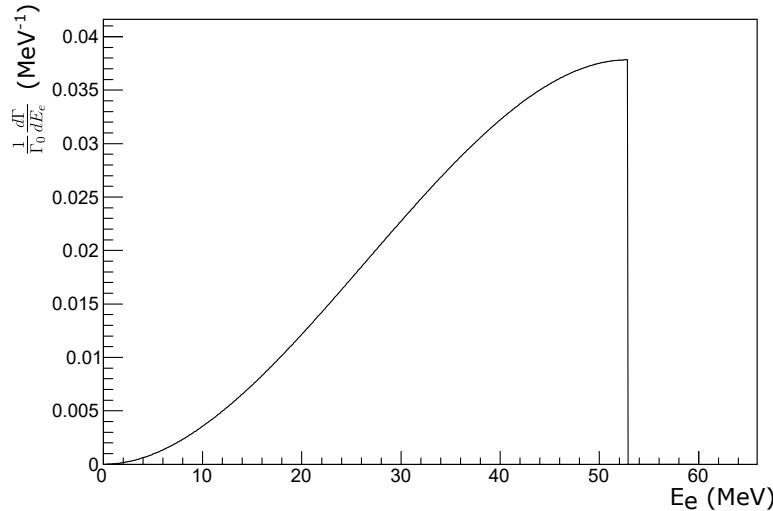
Figure 1.1: The energy spectrum of the free muon decay.

1.4.2 Watanabe-Shanker spectrum

Watanabe calculated the DIO electron momentum spectrum for several material such as O, C [1] as shown in Figure 1.2. In this calculation, the nuclear-recoil effects were completely neglected because the recoil energy should not affect to the DIO electron in low energy region. The high momentum region

which used for background estimation in the μ-e conversion experiments was not calculated by Watanabe. The spectrum such calculated by Watanabe for Al, hereafter called Watanabe-Al, was confirmed in TWIST experiment in TRIUMF [2]. The measured spectrum in TWIST experiment agrees well with the Watanabe spectrum as shown in Figure 1.3.

On the other hand, Shanker studied the DIO momentum focused on the high-energy end in 1982 [21]. The nuclear-recoil effect was included in his calculation. The calculations of Watanabe and Shanker were numerically combined at 90 MeV to evaluate the DIO spectrum in a arbitrary way and the combined spectrum is called "Watanabe-Shanker spectrum" in the μ-e conversion experiments.

Note that the Watanabe spectrum was not calculated for C element that will be used for the target in DeeMe experiment so that the Watanabe-O spectrum connected with Shanker-C spectrum had been used to evaluate the DIO background for DeeMe experiment when it was designed.
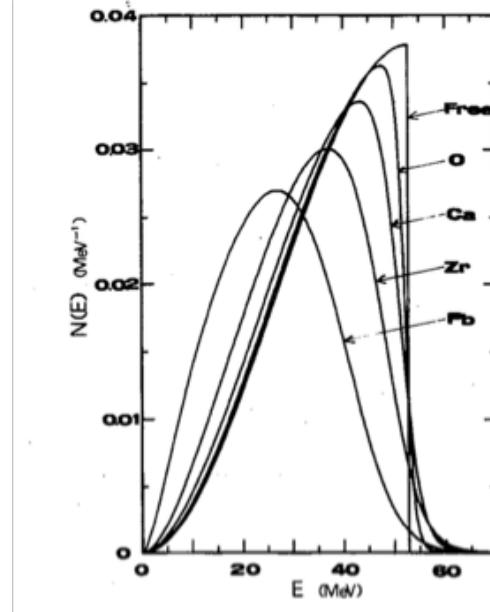
Figure 1.2: The DIO spectra for several elements calculated by Watanabe [1].
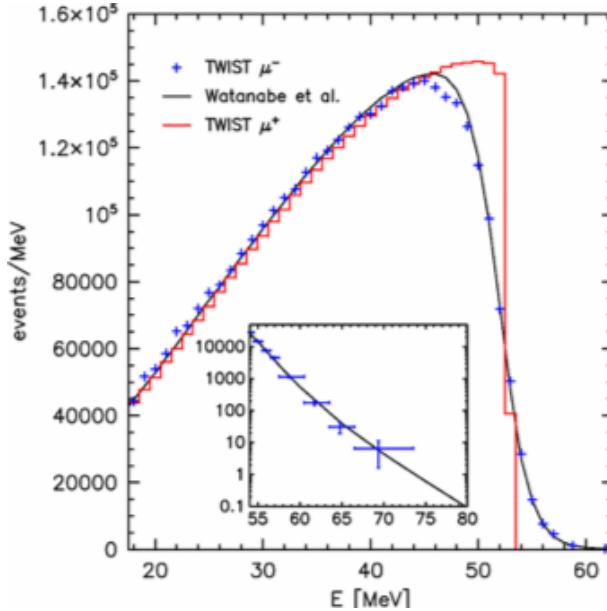
Figure 1.3: The DIO spectra measured in the TWIST experiment and calculated theoretically [2].

1.4.3 Czarnecki spectrum

After the DeeMe experiment proposed, Czarnecki *et al.* evaluated the DIO spectrum for muonic carbon in detail [22]. They calculated the spectra considering the nuclear-recoil effect in full energy range (0 to end point) for C, Al, and Si as shown in Figure 1.4.

The spectrum calculated for Al was compared with the spectrum measured in TWIST experiment and they were also consistent [23]. The difference of these two spectra for Al is very small and has not been observed yet.

1.4.4 Watanabe-C spectrum

As mentioned before, Watanabe did not calculated DIO spectrum for C in the original paper. In order to see difference of the DIO spectrum between the way Watanabe calculated and Czarncki calculated. Watanabe-C spectrum was calculated by Uesaka. Figure 1.5 shows the Watanabe-C spectrum is different from Czarnecki-C spectrum in 52.8 MeV to the end-point region.
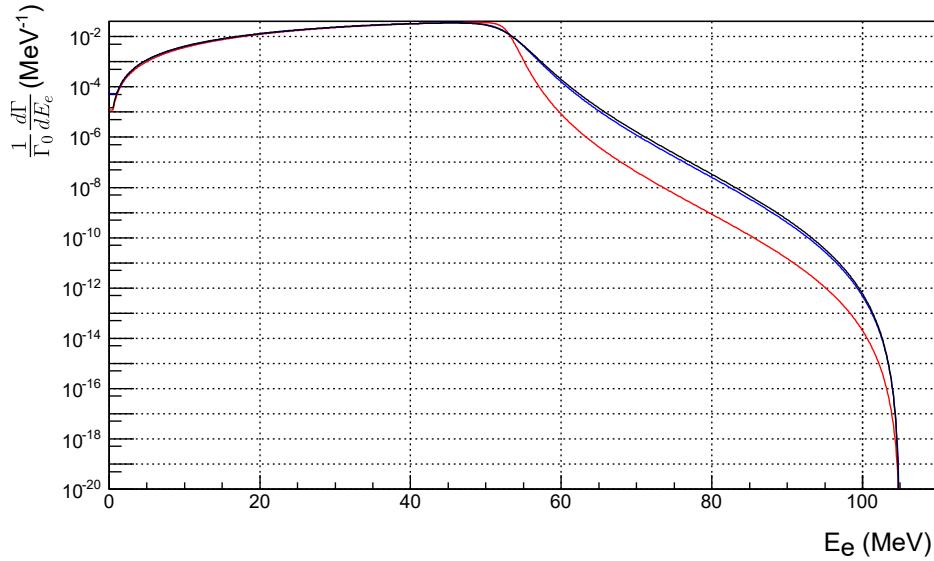
Figure 1.4: The momentum spectrum of DIO electron calculated by Czarnecki. Red, blue, and black lines show muonic C, Al, and Si atom respectively.
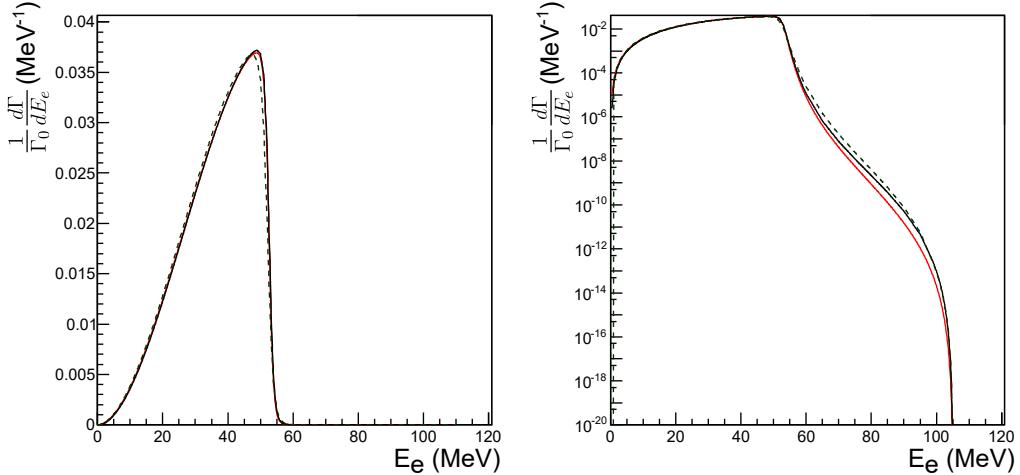
Figure 1.5: The momentum spectra of DIO electron calculated for C by Czrnecki (red line), Uesaka-Shanker (black line), and Watanabe-Shanker (broken line). Left shows linear scale and right shows logarithmic scale.

1.5 Overview

This paper focuses on a preparatory experiment for DeeMe, an experiment aimed at measuring μ-e conversion. An overview of the DeeMe experiment itself and burst-tolerant MWPCs, which are essential for the DeeMe, is provided in Chapter 2. This experiment had used the detectors as a spectrometer capable of momentum reconstruction for the first time. The objective was to obtain operational technique of the burst-tolerant spectrometer and to create an analysis framework which can be utilized in the μ-e conversion measurement. In this experiment, muons from the J-PARC MLF D-Line were stopped in a target, and the Michel decay spectrum from μ^+ decay was observed for calibration. Additionally, DIO momentum measurements using μ^- were conducted for the first time. The experimental setup and measurement conditions are detailed in Chapter 3, and the analysis procedures are explained in Chapter 4. Furthermore, Chapter 5 compares the DIO momentum distribution with the theoretical spectrum using MC simulation. In Chapter 6, systematic errors that may also be expected in the H-Line experiment are examined.

Chapter 2

DeeMe experiment

As mentioned in the previous chapter, the purpose of this study is to conduct a performance test of the detectors and establish the development environment in preparation for DeeMe experiment, which aims to search for the μ-e conversion. This chapter will first outline the experimental plan of DeeMe, describe the required detectors, and discuss the necessary analyses.

2.1 Overview

DeeMe is an experiment to search for μ-e conversion at Japan Proton Accelerator Research Complex (J-PARC) Material and Life Science Experimental Facility (MLF). This experiment utilizes high intensity pulsed proton beam from Rapid Cycling Synchrotron (RCS), where the repetition of the beam is 25 Hz.

The concept of DeeMe experiment is shown in Figure 2.1. The 3-GeV pulsed proton beam from RCS hits the production target placed in the Muon Science Establishment (MUSE) facility. The material of the production target is graphite (C). The pions produced by the beam decay into muons and the muons stop in the production target to form muonic C atoms. Then the decay electrons from the muonic atoms are transported to a spectrometer by H-Line with eliminating low momentum background particle. The momentum of electron is measured by our spectrometer.

The decay modes of a muon in a muonic C atom are DIO (92 %) and muon capture (8 %). The energy of signal electron $E_{\mu e}$ is 105.06 MeV and the lifetime of the muonic C atom is 2.0 μs. The signal electron can be

discriminated by its time and momentum information. By utilizing only the production target, it is possible to simplify the entire apparatus of experiment. Additionally, with the high-intensity proton beam at J-PARC, DeeMe is expected to update the upper limit of the branching ratio.
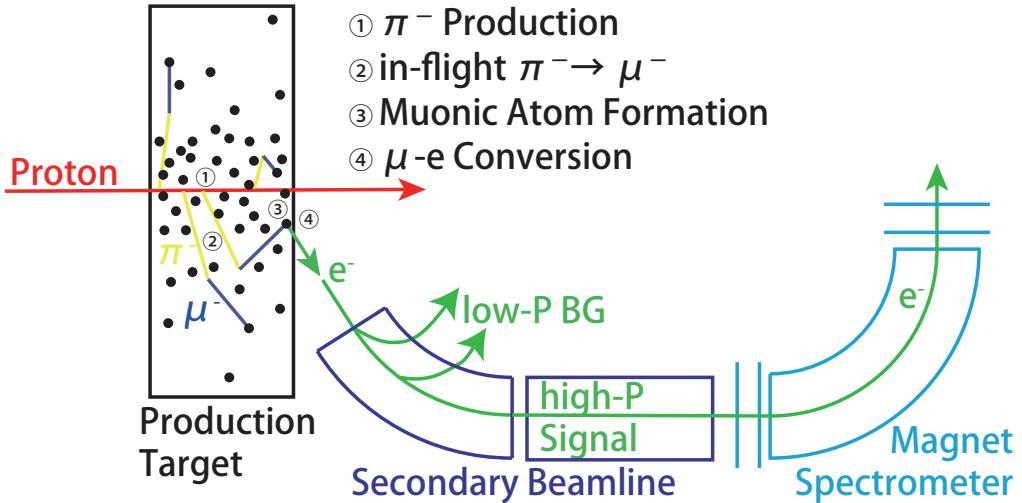
Figure 2.1: The schematic view of DeeMe experiment.

2.2 Experimental facilities

J-PARC provides a high intensity pulsed proton beam for researches in various fields such as particle physics, material and life science. J-PARC has three accelerator, i.e., 400 MeV linear accelerator (LINAC), 3 GeV synchrotron (RCS), and 50 GeV synchrotron (Main Ring: MR) as shown in Figure 2.2.

The negative hydrogen atoms H^- are produced at a source in LINAC, then they are accelerated to 400 MeV in the RF cavity forming a "bunch". The accelerated bunches are injected to the next accelerator, RCS, with 25 Hz injection cycle. Before the proton beam is induced to the circulating orbit of RCS, the charge of the bunched H^- beam are converted into positive by passing them through a charge strip foil. The proton beam is accelerated to 3 GeV and then extracted to MLF and MR. The beam extracted from RCS

to MR is accelerated to 50 GeV. The 50 GeV beam is utilized in the Hadron Beam Facility and Neutrino beam line aiming at Kamiokande.

DeeMe utilizes the 3-GeV pulsed proton beam in MLF MUSE. In this section, RCS and MLF, important facilities for DeeMe, are explained.
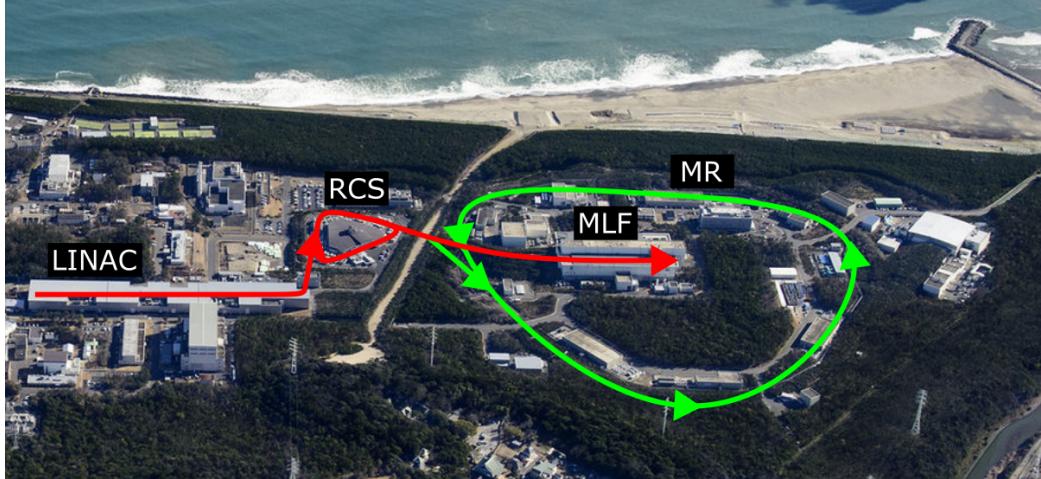
Figure 2.2: The bird's eye view of J-PARC. (C)J-PARC Center.

2.2.1 J-PARC RCS

The H^- beam from LINAC is lead to RCS and converted to proton by the charge strip foil [24]. The proton beam is accelerated to 3 GeV in RCS and extracted to MLF or Main Ring (MR). The designed beam intensity is 1 MW, that beam power is realized by several trial operations. Recent actual beam power is around 700–800 kW.

There are two RF buckets in the RCS ring. These two bunches accelerated in the RCS ring are extracted to MLF/MR by fast extraction. The fast extraction is an extraction method by which all protons in two bunches are extracted in one turn. Due to the fast extraction, no proton exists out of the bunched proton beam in principle.

2.2.2 J-PARC MLF

A rotating graphite target is utilized as muon production target in MUSE. MUSE has four beamlines named U-Line, S-Line, D-Line and H-Line [25].

The S-Line (Surface muon beamline) utilizes so-called "surface" muons which are produced from the pion stopped in very surface of the production target. U-Line (Ultra-slow muon beamline) provides muons of low kinetic energy 10^2–10^3 eV. D-Line utilizes the surface muon and decay muon from in-flight pion decay (detail in Section 3).

H-Line is a beamline for fundamental physics such as DeeMe, MuSEUM [26], and g-2/EDM [27]. H-Line has three solenoid magnets (HS1–3), two bending magnets (HB1–2), and triplet quadruple magnets (HQ1–3) [28]. The muon capture solenoid magnet (HS1) have large aperture of about 130 mSr in order to realize the high intensity beam. The muons and electrons up to 120 MeV/c are available and the momentum acceptance of H-Line is $\pm 5\%$ for the flat-top region at the entrance of the final focusing section HQ1–3. For DeeMe experiment, due to the momentum range and acceptance, the background from DIO and delayed-proton can be estimated by using the momentum spectrum. Its construction had finished in 2021, the commissioning run has started. The schematic time structure of proton beam is shown in Figure 2.3.
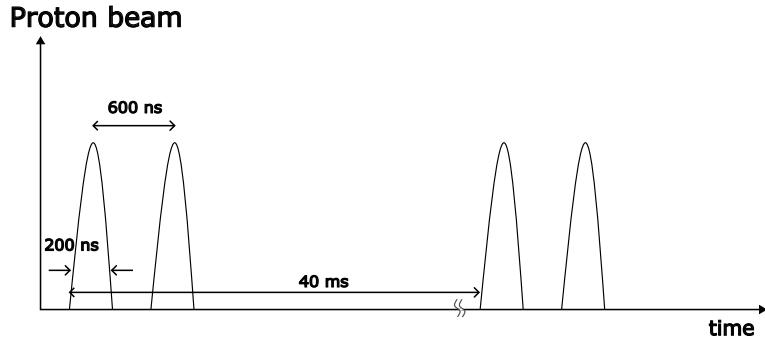
Figure 2.3: Time distribution of proton beam from RCS and electron at detector.

2.3   Spectrometer

The spectrometer system of DeeMe contains a dipole magnet and four multi-wire proportional chambers (MWPCs). The electrons with its momentum p from H-Line beam window are bent in uniform magnetic field B of the

magnet. They are rotated by the Lorentz force as

$$\frac{p}{\rho} = qB, \tag{2.1}$$

where ρ is the radius of the circular motion of the charged particle and q is the charge of the particle. Now, for DeeMe experiment, p is 105 MeV/c for the signal momentum and $q = e = -1.6 \times 10^{-19}$ C. The tracks of the charged particles are reconstructed by the hit positions on the four MWPCs. The momentum of the electron can be calculated from the bending angle of the track and the known magnetic field.

2.3.1 Bending magnet

Our dipole magnet was utilized at PIENU experiment in TRIUMF and it was transported to J-PARC in 2014. Its size is 2500 mm × 2350 mm × 700 mm and the size of the field region is 930 mm × 760 mm. The field height is 300 mm. The strength of magnetic field is planned to be 0.4 T for 105 MeV/c electron to bend by 70 degree.

The magnetic field map of this magnet was calculated by OPERA-3D, which is a software to calculate magnetic field by Finite Element Method. Its performance test and confirmation of consistency between real and calculated field map were conducted at MLF in 2015 [29].

2.3.2 Burst-tolerant MWPC

Due to the design of DeeMe experiment, the prompt burst of secondary charged particles produced by 3-GeV primary proton beam bunch reaches to our experimental hall. Our MWPCs have to detect electron right after they are exposed to prompt burst 10^8 charged particles in a pulse where its instantaneous hit rate is estimated at 70 GHz/mm^2. To avoid saturation of the MWPC by the burst, we had developed burst-tolerant MWPCs, which can control its gas multiplication by switching high-voltage applied to its potential wires [3]. The gas gain is amplified to $O(10^4)$ quickly right after the prompt burst and keeps the level while the delayed electrons coming from μ-e decay are observed. The other period, it is usually $O(1)$ to avoid saturation. The repetition of the proton beam is 25 Hz and interval of two banches is 600 ns. Thus, the HV of the potential wires is quickly decreased to 0 V at start of analysis time window as shown in Figure 2.4.
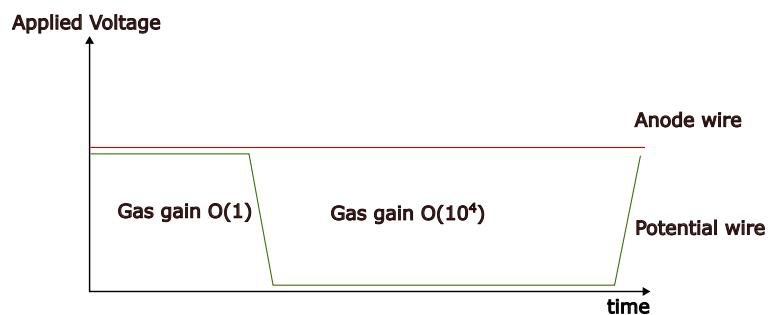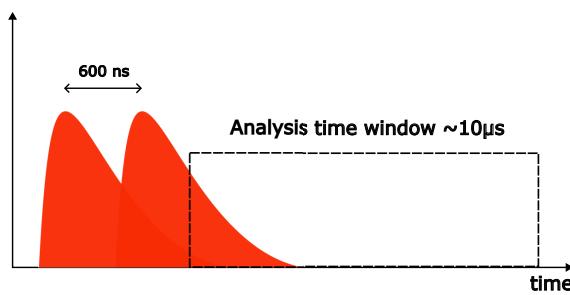
Figure 2.4: Time structure of the electrons from the production target (top) and the schematic view of the HV-switching of the MWPC (bottom).

We developed two types of MWPC, one is MWPC-713 and the other is MWPC-724. Figure 2.5 shows an outline of the structure of our MWPC and a summary of the materials in the MWPCs is shown in table 2.1. Both of two types of MWPC have 136 anode wires and 137 potential wires and they are W coated with Au. The diameter of anode wire is 15 μm and of potential wire is 50 μm. The wire pitches of MWPC-713 and MWPC-724 are 0.7 mm and 0.75 mm respectively. A distance between the strip plane and a cathode plane made of an aluminum foil 9 μm on a polyimide film 25 μm is 3 mm. Both outsides of the detection region are covered by 12.5 μm thick PET film. The waveforms are read out from cathode strips and one of two cathode planes is readout for X direction and the other is readout for Y direction. The numbers of strips are 80 for X-plane and 16 for Y-plane and the strip widths are 3 mm for X-plane and 15 mm for Y-plane. The position resolution is estimated to be 640 μm according to [3]. Inside of the chamber is filled mixed gas with Ar:isoC$_4$H$_{10}$:C$_3$H$_8$O$_2$=70:20:10.

In the early stage of the development, the gas mixture ratio was set to argon:ethane = 1:2 as mentioned in Section 3.2.3, but in order to operate the detector with lower HV and reduce the trip frequency, the quencher was changed to isobutane. Additionally, the isobutane, an organic gas, forms solid or liquid polymers on the cathode planes when it recombines after ionization. This causes a contamination of the cathode planes surface and discharge, so methylal (C$_3$H$_8$O$_2$) was mixed in.

Before adding methylal, a bench test of the MWPC was conducted by injecting electrons at a rate corresponding to the bursts expected in the H-Line during the OFF timing of the detector for the purpose of observation the waveform after prompt burst. As a result, sustained pulses, will be referred to as afterpulses in this paper, were observed immediately upon turning it ON. This was thought to be due to the amount of excited argon exceeding the quenching capacity. Consequently, photons not absorbed by quenching gas produce electrons from the cathode surface via the photoelectric effect and these electrons reproduce primal ionization. As an alternative approach, a well-known method involves adding a small amount of molecules containing highly electronegative atoms (mainly fluorine or bromine) to absorb the electrons emitted from the cathode before they cause an avalanche near the anode wires. Methylal, containing oxygen with high electronegativity second only to fluorine, was expected to have a similar effect, and its addition successfully suppressed afterpulses. Through these optimizations of the gas mixture, it was found that the detector exhibited the expected switching per-

30

formance even in the H-Line environment. Note that the first gas mixture, argon and ethane, is utilized in this paper.

The waveform of MWPC reveals a damped oscillation because of HV switching, and the shape of the oscillation is invariant for every HV-switching. Thus, the baseline oscillation of the raw waveform can be removed by offline analysis (details of this analysis is described in Section 4.1). The waveform is recorded by 12 fast analog-to-digital converter (fast ADC or FADC) boards with MIDAS DAQ system [30]. One FADC board has 32 channels to readout the waveform from the MWPC which has 80 channels for X-axis and 16 channels for Y-axis. The FADC boards record the waveforms from $4 \times (80 + 16)$ channels in 80 μs length for each trigger, where trigger signal is synchronized with the beam injection trigger to MUSE.

A bench test to evaluate the efficiency of MWPC had been done at Kyoto University Research Reactor Institute (KURRI) in 2018. The efficiency increases quickly to ~ 1 in 1 μs after switching as Figure 2.6.
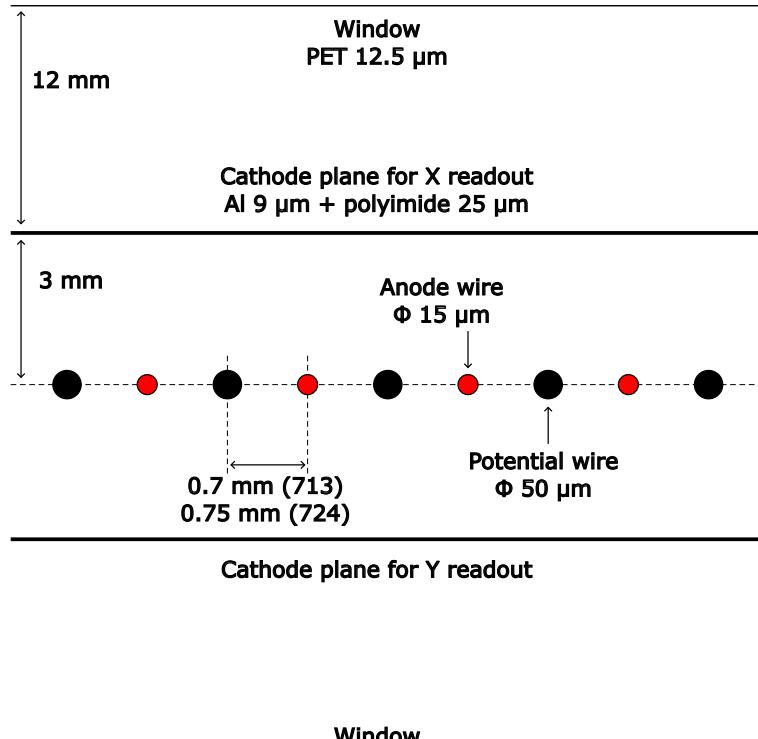
Figure 2.5: The schematic view of the structure of our MWPCs.
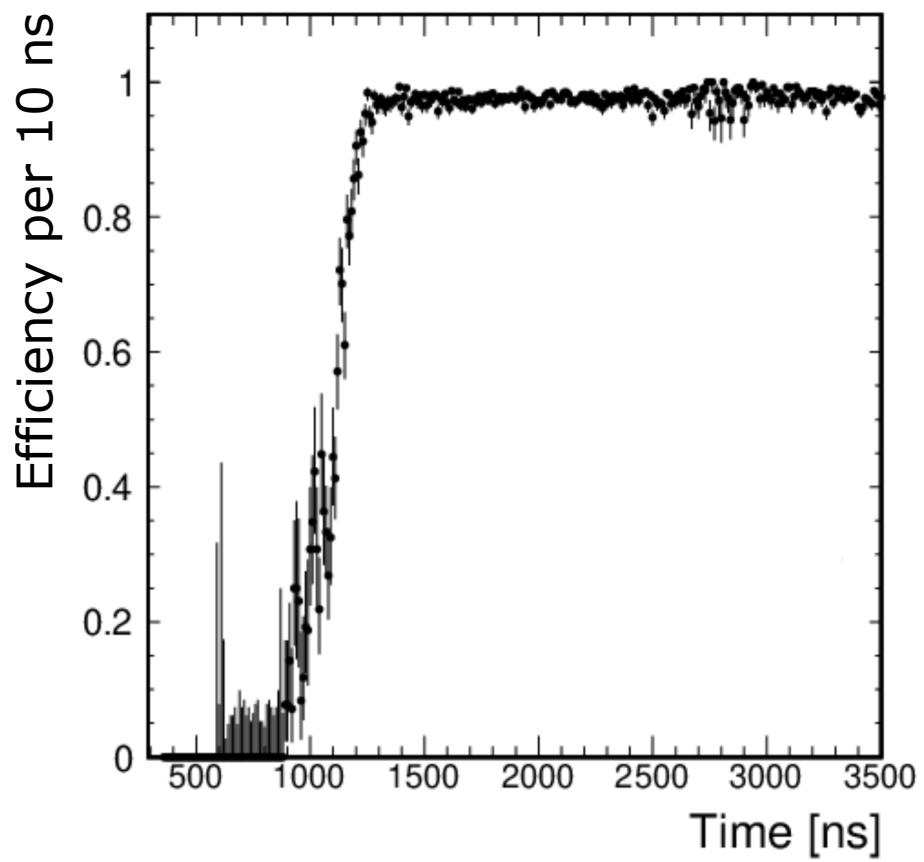
Figure 2.6: Time dependence of detection efficiency of the MWPCs evaluated in a bench test [3].

Table 2.1: Summary of the materials of the detectors and their converted thickness to kapton.

Material	Thickness (μm)	Radiation length (g/cm^2)	density (g/cm^3)	Kapton-equivalent thickness (μm)
Plastic film	12.5×4	39.95	1.38	50
Al strip	9×2	24.01	2.70	85.7
Wires (W)	1.43 (713)	6.76	19.3	20
	1.53 (724)			21.4
Mixed gas	24×10^3 (713)	23.08	0.0013	20
(Ar+ethane)	26×10^3 (724)			22

2.4 Sensitivity

The single event sensitivity (SES) is defined as below;

$$\text{SES} = \frac{1}{f_{\mu-\text{atom}} \times N_p \times B_{\text{muon capture}} \times f_{\text{det}}}, \tag{2.2}$$

where $f_{\mu-\text{atom}}$ is the production fraction of muonic atom in the target per one proton, N_p is the number of produced protons in RCS, $B_{\text{muon-capture}}$ is the branching ratio of the muon capture process, and f_{det} is the rate of the detected signal electrons to μ-e conversion electrons produced in the target. The branching ratio $B_{\text{muon-capture}}$ is 0.08 for the muonic C atom and the number of protons N_p is obtained by using beam power P_p =1 MW and beam energy $K_p = 3$ GeV for one year ($t = 2 \times 10^7$ s)

$$N_p = \frac{P_p t}{K_p e} = 4.2 \times 10^{22} \tag{2.3}$$

$f_{\mu-\text{atom}}$ and f_{det} are estimated by the MC simulation as 4.9×10^{-6} and 6.5×10^{-4} respectively. We expect SES= 1×10^{-13} [31][32].

2.5 Background

The momentum spectra of the signal electron and backgrounds are shown in Figure 2.7.

33

DIO momentum of high momentum tail is proportional to $(E_{\mu e} - E_e)^5$. DIO background can be distinguished by momentum information from the μ-e conversion electron. On the other hand, the DIO spectrum at the end point can be utilized for evaluation of yield of the muonic atom because the DIO electrons are produced from the same source, the muonic atom, as the μ-e conversion electron. In DeeMe experiment ,the DIO momentum distribution will be compared with the Monte-Carlo simulation by using well-known theoretical curve.
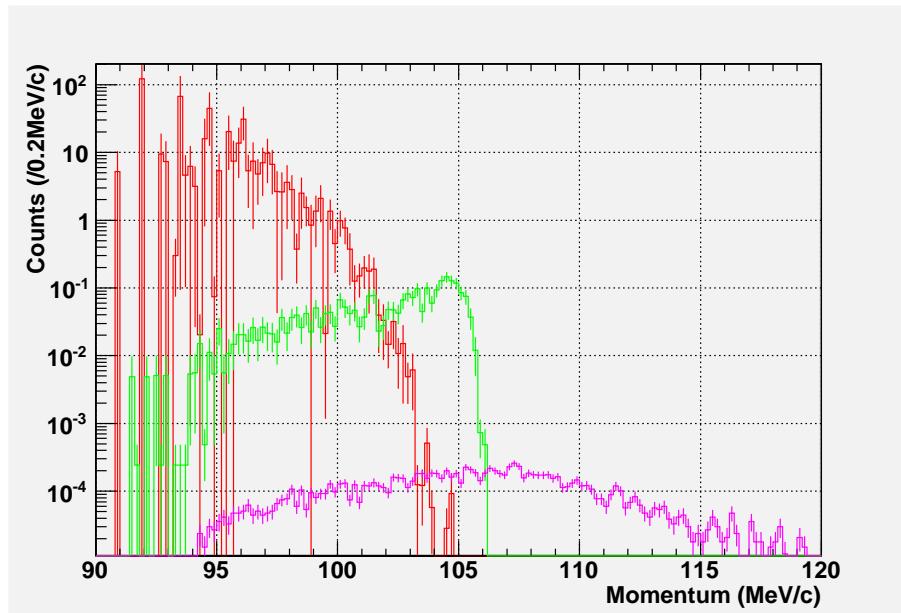
Figure 2.7: Estimated momentum spectra of signal (green) and backgrounds (red and purple line are DIO and delayed proton), where $B_{\mu e} = 3 \times 10^{-14}$ and 2×10^7 s of beam time with 1 MW proton beam are assumed.

The cosmic ray induced background is suppressed because of the duty factor 1/20000.

The prompt burst is distinguished by HV-switching MWPC instead of momentum information. However, if there is residual proton in RCS, that proton produces background electron whose momentum spectrum can reach to $E_{\mu e}$. This background cannot be distinguished by momentum and time information so that it is monitored by a beam loss monitor placed at the extraction point of RCS. The measurement by the beam loss monitor and

MC simulation revealed that the amount is 0.027 event/year.

Chapter 3

Performance test of the spectrometer system

This experiment was conducted as a preliminary step for DeeMe experiment, aiming to test the detectors and DAQ, as well as to develop an analysis framework that can be used in the main experiment. This chapter describes the experimental apparatus, setup, and acquired dataset of the performance test of the spectrometer employing the burst-tolerant MWPCs. The development of the analysis system will be discussed in the next chapter.

3.1 Overview

We had conducted bench tests on one from each of the four MWPCs at a laboratory (KURRI, KURNS) and they worked well as we expected. Then we planned integration tests of the detectors, magnet, and data acquisition system (DAQ) at J-PARC MLF D-Line to verify the performance of our spectrometer system, especially the following three points: 1. Whether the MWPCs operate simultaneously, 2. Whether the DAQ system functions properly, and 3. Whether results can be analyzed from the data. In addition, analysis tools were expected to be developed by using the data obtained from real spectrometer.

We had planned to observe the Michel-decay spectrum of positrons decayed from positive muons and the DIO spectrum with muonic carbon atom for evaluation of this integration test because the shapes of these spectra are known well enough to be compared with the results of the tests.

The momentum region of measured DIO spectrum was decided around 55 MeV/c. The DIO spectrum around the end-point momentum was more useful considering μ-e conversion experiment at H-Line experiment, but D-Line is a facility provides muon beam to users for various purposes and the period to occupy the beamline is typically several days. The muon intensity provided by D-Line was 10^5 /s at 30 MeV/c and the decay rate at the end-point region is less than $O(10^{-10})$ as shown in Section 1.4. Thus, it was totally not enough time to observe the DIO spectrum at the end-point momentum. In addition, the momentum region around 55 MeV/c is expected to show the seeping of DIO spectrum.

3.2 Setup

The setup of this measurement in D2 area is shown in Figure 3.1. The muon beam from the D2 beamline passed through a thin beam window and extracted from vacuum to atmosphere was stopped in the target located downstream of the beam window. The electrons produced by the muon decay in the muon stopping target were emitted from the muon stopping target in 4π direction and the electrons toward the spectrometer were detected by four switching MWPCs (WC0-3) where a sector bending magnet (SBM) was placed between WC1 and WC2. Note that the sector bending magnet used in this measurement was not the same to the PACMAN magnet that will be used in the μ-e conversion search measurement of the DeeMe experiment because the PACMAN was too large to be placed in D2 area.

A hodoscope containing two scintillation counters (HC0, HC1) was set by side of the muon stopping target in the opposite side of the spectrometer for the estimation of the muon yield stopped in the muon stopping target by using electrons from the muon decay.

The coordinate system of the experimental setup is defined by referring to the sector magnet as shown in Figure 3.1. The Z-axis of the system upstream of the entrance of the sector magnet is along the axis of the magnet entrance marked on the iron yoke of the magnet. The Z-axis of the system downstream of the exit of the sector magnet is along the axis of the magnet exit, which is also marked on the iron yoke. The Z-axis in the magnet is not straight line but curved as the magnet pole curves, thus the Z-axis of the whole system is not a simple straight line, that is rather like a beam-center axis in beam optics. The origin of the Z-axis is defined at the entrance of the sector

Beam window

Muon stopping target

WC0

Y

Z

X

WC1

Beam axis

HC0   HC1

SBM

WC2

X

Y

WC3

Z
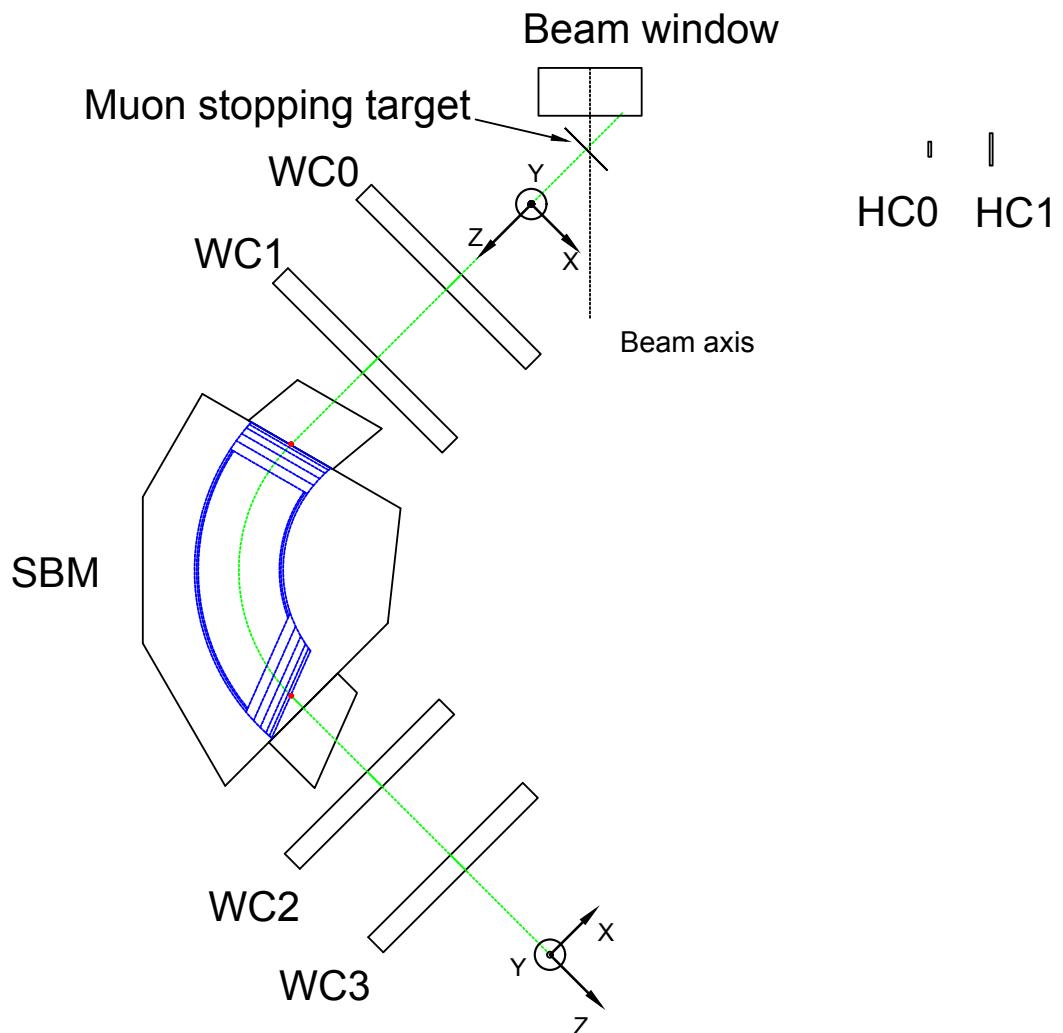
Figure 3.1: The setup of DIO momentum experiment at D-Line.

magnet. Y-axis is defined along vertically upward and $y = 0$ plane is at the median of the sector magnet. X-axis is defined as orthogonal to both Y- and Z-axis in the right-hand Cartesian coordinate system. Note that the X-axes for different Z positions are not parallel due to the nature of the Z-axis definition. The most important coordinate is X-axis because the magnetic field of the magnet bends the charged particles to X direction.

The each instrument position was measured with the error 0.1 mm for X and Y and 1 mm for Z. The positions of each instrument (target, WC0-3, SBM, and HC0-1) were measured before and after the data taking. The measured positions of MWPCs are shown in Table 3.1.

Table 3.1: Positions of the detectors, where z positions indicate the distance between the median of each MWPC or the target and the nearest edges of the pole of spectrometer which is shown in Figure 3.1 with red dot.

	x [cm]	y [cm]	z [cm]
Muon stopping target	0	0	-137.7
WC0	0.32	0.0	-77.4
WC1	0.30	0.0	-37.4
WC2	-0.51	0.0	31.6
WC3	-0.03	0.0	71.6

3.2.1 Beam Line

D-Line, which had been utilized in this experiment, is a muon beamline for multi-purpose from fundamental physics to non-destructive element analysis[33]. The layout of D-line at the time this experiment was performed is shown in Figure 3.2. Both positive and negative muons are available with this beam line. D-Line can deliver muon called "decay-muon" with the momentum of up to 120 MeV/c and "surface-muon" with ∼30 MeV/c. The decay-muon beam is produced by collecting the muon from pion decay in-flight in the solenoid section of the beamline. The surface-muon is the muon emitted from pion decay in subsurface of the target.

The electron spectrometer for this measurement was installed in the D2 area, one of two available experimental area are located at the exits of D-Line. The beamline was set at "decay-muon" mode with a beam momentum

at 30 MeV/c. The muon-electron separator was turned on. The negative-muon intensity was 1×10^5 /s at 220 kW of proton beam power.

In order to control the beam intensity, the slits are installed in the beam-line. The slits are able to be moved to vertical and horizontal direction in the orthogonal plane to beamline. The slits were controlled to keep the hit rate of the WC0 about 20 hits in a cycle of pulsed proton beam in order not to lose counts by multiple hits in a short time.

3.2.2 Muon Stopping Target

A muon stopping target is in a planner shape and was placed at the down-stream of the D-line exit in D2 area as already shown in Figure 3.1. It was rotated in the horizontal plane by 45° so that the perpendicular axis of the target plane became parallel to the Z-axis of the upstream-side of the spec-trometer system. A slab of material suspended on vinyl strings from the aluminum frame as shown in Figure 3.3.

Four different types of material were used for the target: graphite, Si, SiC, and holmium. The characteristics of these materials are shown in Table 3.2. The graphite target is a 20 cm square board and its thickness is 1.0 mm. Note that the thickness is decided to maximize the muon stopping rate and to minimize the energy loss of outgoing electrons toward the spectrometer. In this thesis, data taken with Si, SiC, and Holmium are not discussed.

The holmium target was used to confirm the effect from polarization of decay muon beam. The electron momentum spectrum from muon decay generally depends on the polarization of initial muon as shown in Figure 3.4. The polarization of negative muon is conserved 20 % in graphite [34] and 0 % in holmium. We measured the Michel decay spectrum with holmium atom in order to be able to modify the spectrum for graphite to non-polarized spectrum.

Table 3.2: Muon stopping target material.

Material Name	density (g/cm^2)	purity	thickness (mm)
Graphite	1.82	>99.9999%	1.0
Si	2.33	-	1.0
SiC	3.21	> 99.9999%	0.7
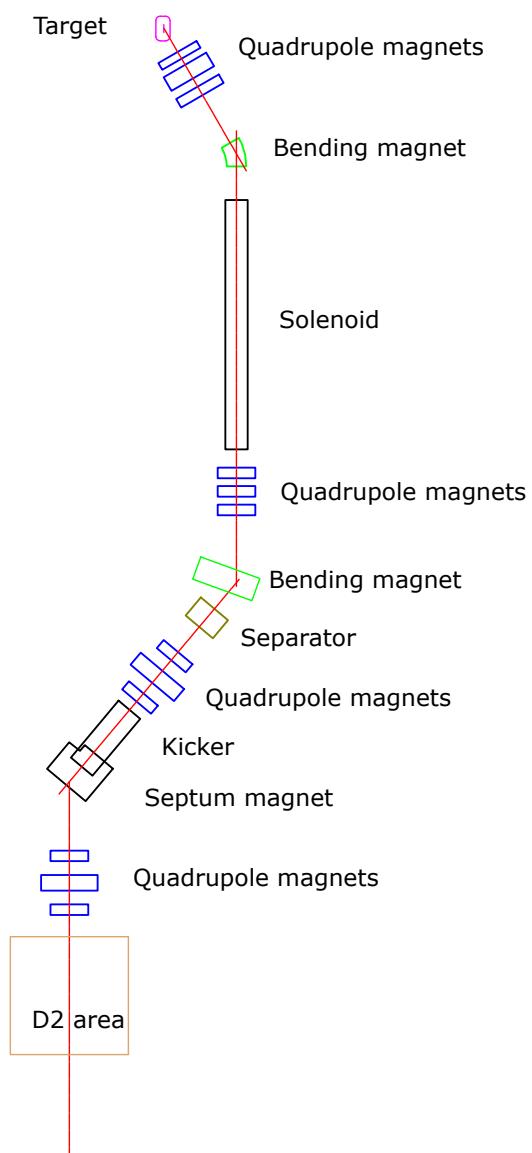
Figure 3.2: Layout of D-line.
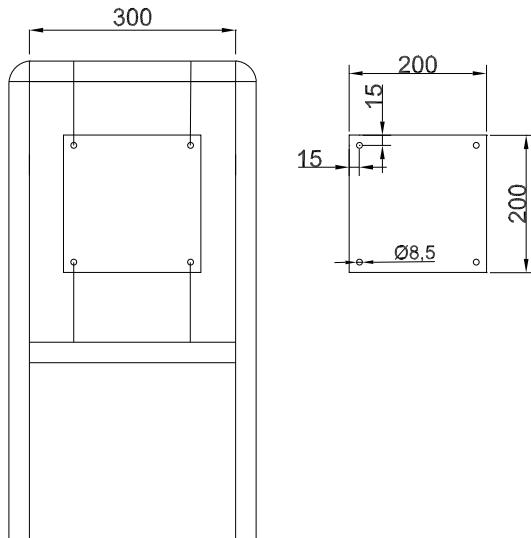
Figure 3.3: Illustration of the muon stopping target and its supporting frame.
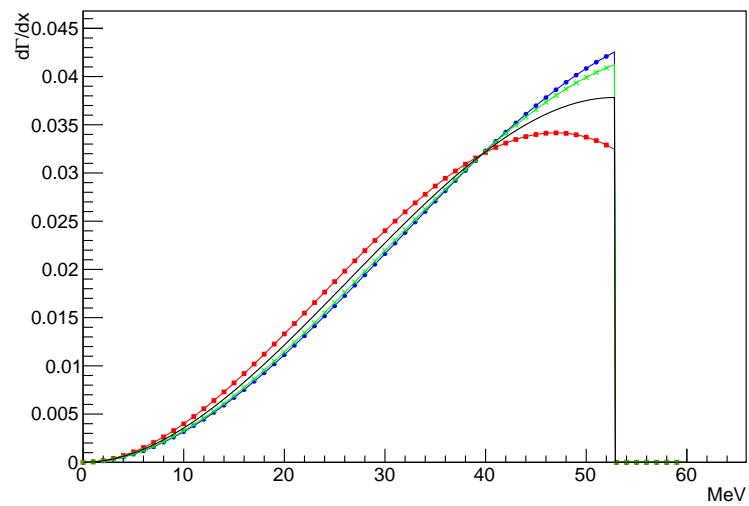
Figure 3.4: The Michel decay spectrum with some typical polarization angle θ. No polarization (black line), $\theta = 0°$ (red circle), $\theta = 180°$ (blue square) , and $\theta = 135°$ (green x).

3.2.3 Electron Spectrometer

The spectrometer consisted of the SBM and the WC0-3 as shown in Figure 3.1. Figure 3.5 shows the shape of the SBM. The SBM's radius is 600 mm and its maximum strength of magnetic field is 445 mT at 386 A. Its magnetic field was calculated as Figure 3.6 by using OPERA-3D [35]. According to the initial survey, the magnetic field including the fringe is well proportional to the current between 65 A and 386 A at least and we had applied the current in [215 A, 263 A] in this experiment. Therefore, the calculated magnetic field is simply scaled for several current values to utilize in the track fitting and the MC simulation described in the Section 4.7 and 5.3 respectively.
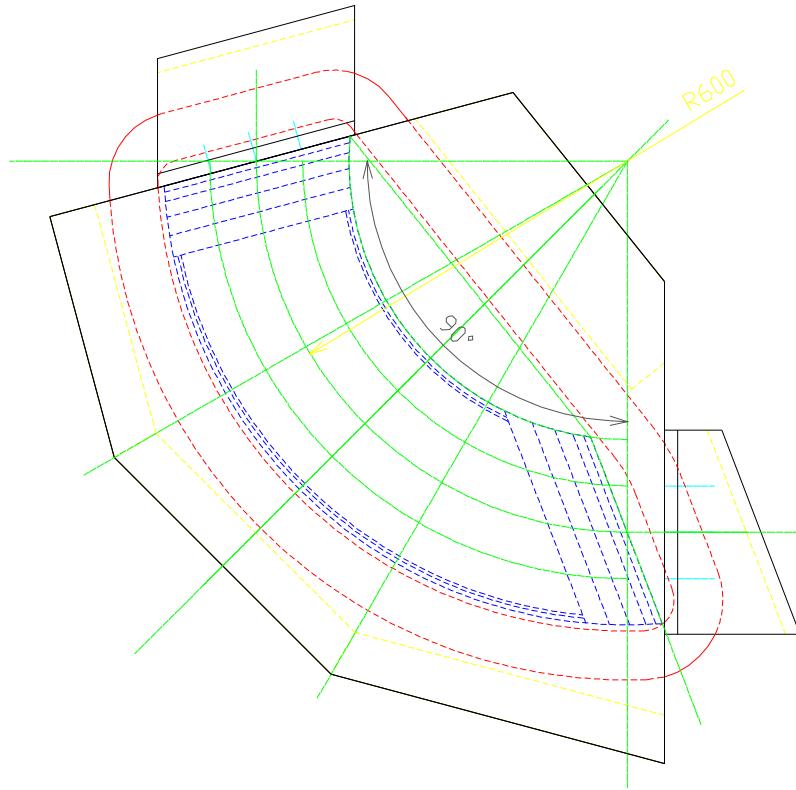
Figure 3.5: The structure of the SBM. The blue, red, and black lines show yokes, coil, and return yoke respectively.

Four HV-switching MWPCs were used as trackers of spectrometer and they were named as WC0-3 from upstream as shown in Figure 3.1. In this
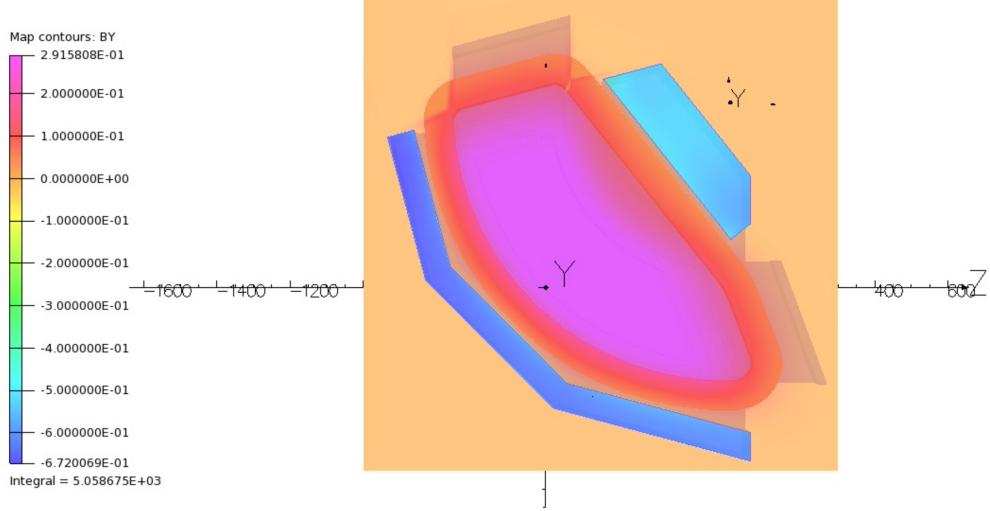
Figure 3.6: Calculated magnetic field of sector bending magnet at median plane (Y=0 cm), where the unit of the color scale is T.

experiment, the prompt burst did not hit the detectors but HV-swathing system was active to confirm their performance. Filled gas mixture was $Ar:C_2H_6 = 1:2$ in this experiment and applied HV was 1630 V for WC0 and WC1 and 1600 V for WC2 and WC3. Note that the gas mixture was updated as mentioned in Section 2.3.2 but this experiment was conducted before the optimization. The enhancement of burst tolerance of the MWPC and the construction of a system using this detector are independent topics. Therefore, this study will proceed with the discussion based on this mixture ratio.

In DeeMe experiment at H-Line, helium bags are installed between the target and each detector to decrease the multiple scattering but in this measurement there were filled with the air. The total length of the air region along Z-axis is 3,000 mm from the target to WC3. The scattering angle by the air is estimated to be 0.02 radian for 55 MeV/c electron and it is equivalent to ~ 3 cm of position uncertainty in WC3. However, considering the main purpose of this particular experiment being a first step of whole spectrometer test including a long-term data taking, the scattering effect was accepted. This effect from multiple scattering limits accuracy of the track reconstruction as will be discussed in Section 4.2.

44

3.2.4 Hodoscope

Two plastic scintillators (HC0 and HC1) were utilized as a hodoscope to observe electrons from the muon stopping target directly. Their sizes are 51 mm × 51 mm for HC0 and 110 mm × 105 mm for HC1. The distance between HC0 and HC1 is 208 mm. The number of counts and time information are utilized to obtain yield of the DIO electron and to calibrate time origin of waveform recording systems.

3.2.5 Data Acquisition System

The block diagram of data acquisition system is shown in Figure 3.7. The system consists of HV-switching MWPC, FADC and 500-MHz waveform digitizer (COPPER) system. COPPER (COmmon Pipelined Platform for Electronics Readout) was developed in KEK for the Belle experiment. It is 9U size VME board and its main part has CPU for data processing. One COPPER board has four front-end called *FINNESSE*. One FINNESSE module has 2 channels to record waveforms. The waveforms of WC0-3 and HC0-1 were recorded by 100 MHz-FADC and COPPER boards respectively.

The trigger logic and its time chart is shown in Figure 3.8 and 3.9 respectively. The beam injection timing is used as the trigger for the DAQ system. The time origin t_0 of waveform analysis shown in Figure 3.9 is defined by the start timing of the analysis time window. Note that data in a trigger do not necessarily have one track, i.e. zero or several tracks can be contained in an event. One set of the waveforms taken by a trigger is called an *event* and one set of events written into a file is named a *run*. Usually every 10000 events are combined into a run.

It has remained in this system that the different events are merged into a run, e.g., the index of trigger recorded by a FADC is i but the index recorded by the others is $i + 1$ in the same event and this is called an event mismatching. The way to handle this problem is discussed in Section 4.1.1.

3.3 Data taking

The experiment was conducted three times, March 2017, June 2017, and March 2019 and summaries of data taken are shown in Table 3.3, 3.4, and 3.5. Between June 2017 and March 2019, the preamplifier had been improved
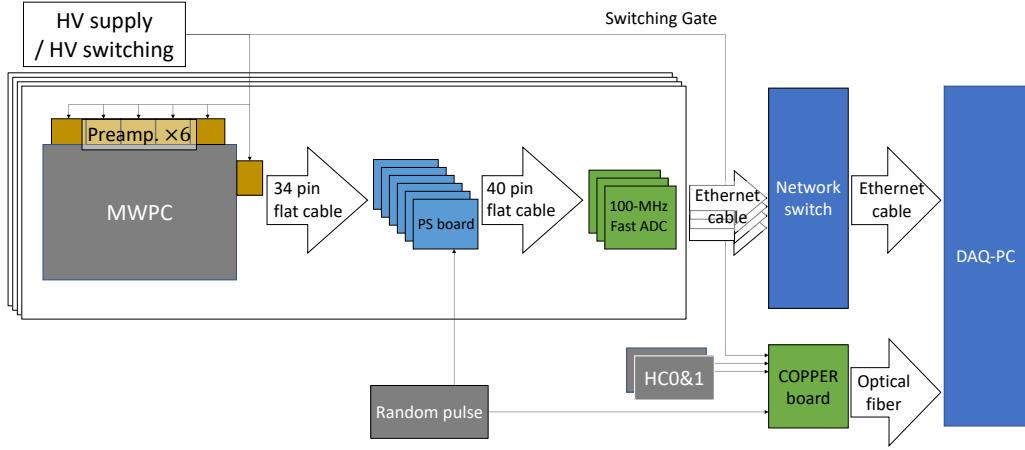
Figure 3.7: The data flow chart from the MWPCs to DAQ-PC.

and the detection efficiency, especially its time dependence, was expected to be improved.

The data set of μ^+ 52.5 MeV/c were taken for momentum calibration by using Michel edge. That of μ^+ 45 MeV/c are utilized to evaluate the acceptance of the spectrometer by using the Michel decay spectrum because its shape is well known. The μ^- 55 MeV/c data set are DIO momentum spectrum. These data set are referred as Edge, Body, and DIO in this thesis.

The list of typical magnitudes B_{Edge}, B_{Body}, and B_{DIO} of the magnetic fields used in these experiment is shown in Table 3.6. The magnitude of the magnetic field by the SBM was monitored in real-time by a NMR fixed on the lower yoke of the SBM. The values are used to determine the scaling factors of magnetic field in the tracking analysis and MC simulation.

In this study, the data with the graphite target in June 2017 is only analyzed in order for the construction of the analysis algorithm to be constructed.
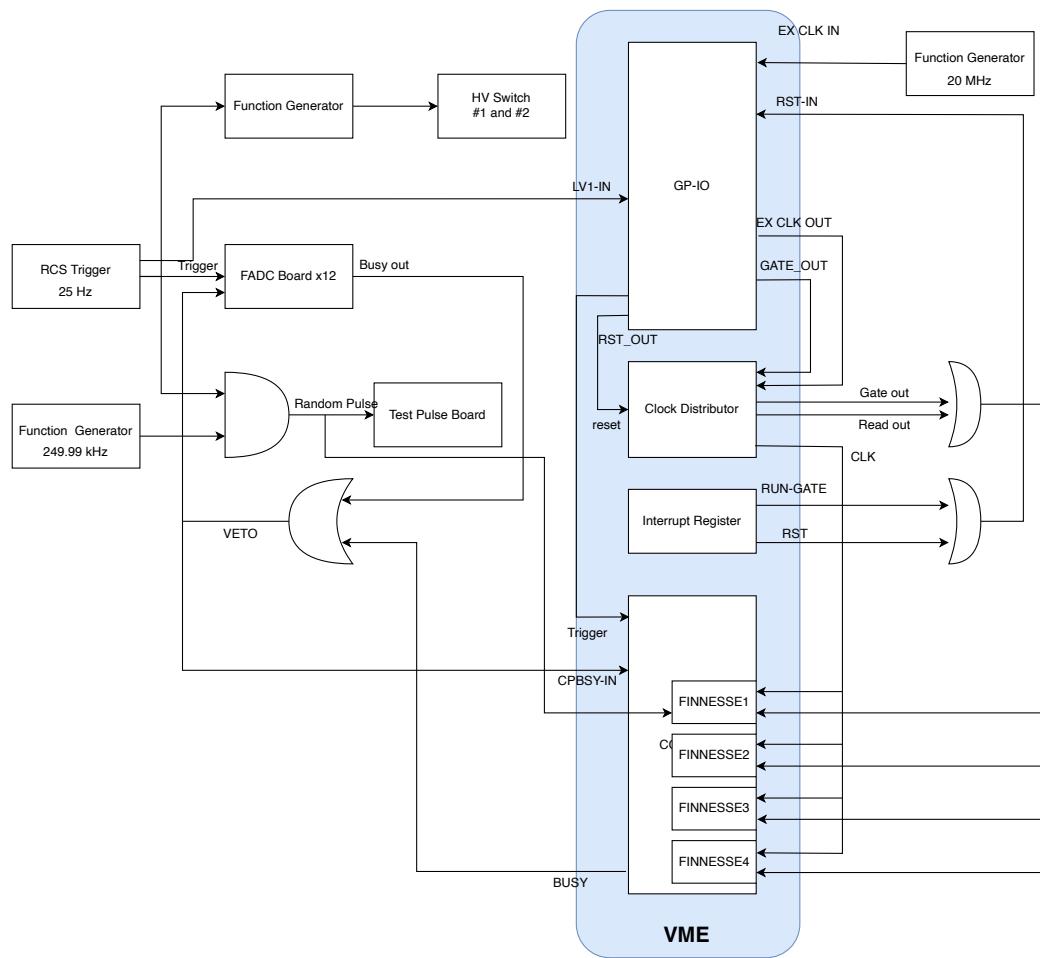
Figure 3.8: The Trigger logic diagram.
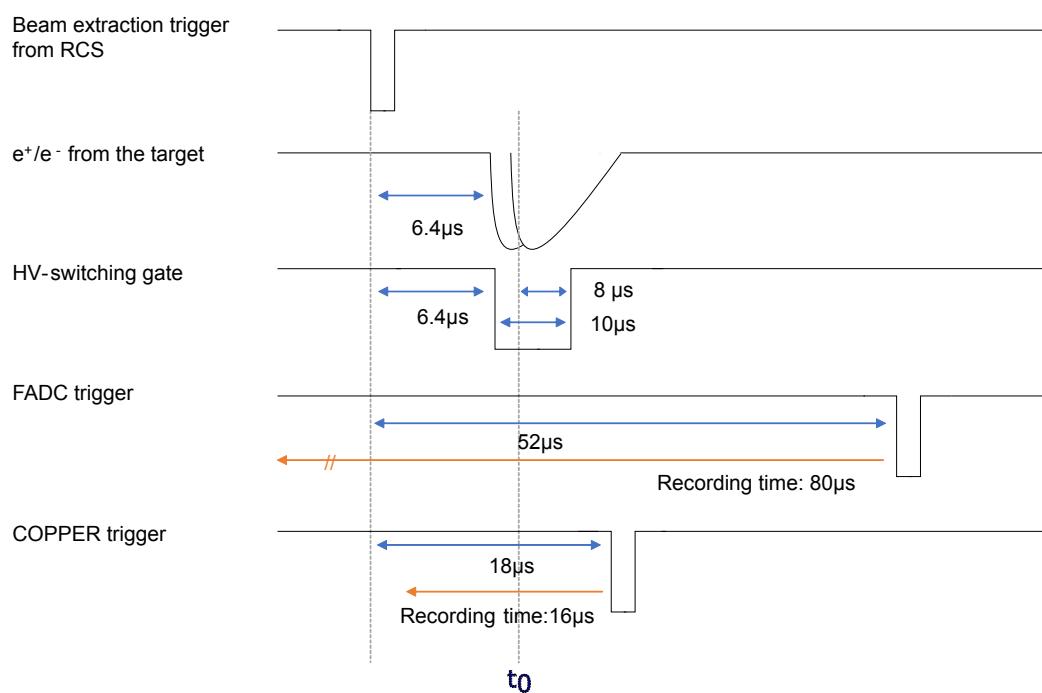
Figure 3.9: Trigger timing of each FADC.

Table 3.3: List of data set in March 2017.

Material	Beam charge	Momentum	Number of trigger
Holmium (Ho)	+	55 MeV/c	2.4×10^5
	+	45 MeV/c	3.0×10^5
	+	55 MeV/c	0.6×10^5
Graphite (C)	+	45 MeV/c	2.0×10^5
	−	55 MeV/c	12.4×10^5

Table 3.4: List of data set in June 2017.

Material	Beam charge	Momentum	Number of trigger
	+	40 MeV/c	1.5×10^5
Ho	+	45 MeV/c	3.7×10^5
	+	52.5 MeV/c	1.8×10^5
	+	60 MeV/c	1.5×10^5
	+	45 MeV/c	4.7×10^5
	−	45 MeV/c	1.8×10^5
C	+	52.5 MeV/c	2.3×10^5
	−	52.5 MeV/c	1.4×10^5
	−	55 MeV/c	6.3×10^5
	−	45 MeV/c	1.5×10^5
Si	−	52.5 MeV/c	1.3×10^5
	−	55 MeV/c	4.8×10^5
	−	45 MeV/c	1.6×10^5
SiC	−	52.5 MeV/c	1.5×10^5
	−	55 MeV/c	11×10^5

Table 3.5: List of data set in March 2019.

Material	Beam charge	Momentum	Number of trigger
	+	40 MeV/c	1.5×10^5
Ho	+	45 MeV/c	3.7×10^5
	+	52.5 MeV/c	1.8×10^5
	+	60 MeV/c	1.5×10^5
	+	45 MeV/c	4.7×10^5
	−	45 MeV/c	1.8×10^5
C	+	52.5 MeV/c	2.3×10^5
	−	52.5 MeV/c	1.4×10^5
	−	55 MeV/c	6.3×10^5
	−	45 MeV/c	1.5×10^5
Si	−	52.5 MeV/c	1.3×10^5
	−	55 MeV/c	4.8×10^5
	−	45 MeV/c	1.6×10^5
SiC	−	52.5 MeV/c	1.5×10^5
	−	55 MeV/c	11×10^5

Table 3.6: The typical magnitude of the magnetic field of SBM measured on the surface of the yoke.

	$|B|$ (mT)
B_{Edge}	289.83
B_{Body}	248.32
B_{DIO}	303.54

Chapter 4

Data Analysis

The measured data are raw waveforms including baseline oscillation from the switching noise so that the hit information should be extracted in the offline analysis. Then the relevant track should be reconstructed from the obtained hit information of WC0–3. After tracking step, event selection should be performed by using parameters obtained from track reconstruction. The analysis workflow is shown in Figure 4.1 (a). The methods of hit finding from the oscillating waveforms, the track reconstruction, and momentum analysis are explained in this chapter.

The results of the measured data are compared with that of the MC generated data of Michel decay and Czarnecki spectrum for carbon atom. In this chapter, data analysis methods and results are described. The analysis workflow of the MC simulation is shown in Figure 4.1 (b). The analysis for the MC data and the comparison between data and MC are described in the next chapter. Note that the body dataset are used in the following analysis except for momentum analysis.
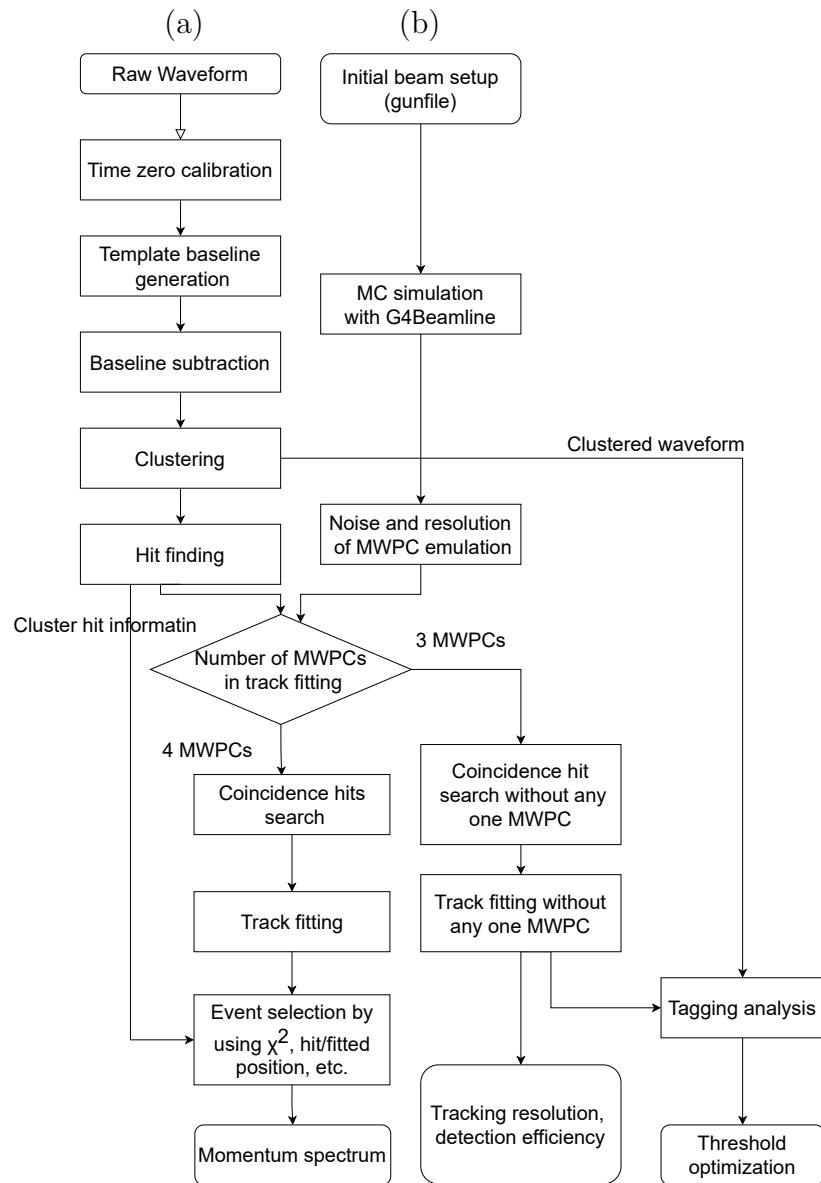
Figure 4.1: The workflow of the analysis for the real data (a) and the MC generated data (b).

4.1 Waveform analysis

In this section, the approach to extract hit information from the waveforms without any external hit-timing information is explained. In order to execute track fitting, hit position and time should be acquired by offline analysis and they are evaluated based on the channel number of MWPCs' strips and the sample point number in FADCs. In addition, the total charge induced on the strips by a particle passing through a detector is also utilized for discrimination real signals from various noises.

Because of the electrical oscillation induced to the raw waveforms by the HV-switching, the oscillation should be removed before the pulse finding. On the other hand, the baselines are the same shape as shown in Figure 4.2 if they are taken in the same condition, such as voltage applied to MWPCs and total charge of prompt burst, so that the baseline oscillation can be suppressed by subtracting template waveforms.

4.1.1 Event quality check

Before explanation of the waveform analysis, as mentioned in Section 3.2.5, the impact of the event mismatching should be evaluated. In order to monitor this event mismatching problem, we introduced random pulses to the waveforms from all strips. A test pulse has been prepared by taking coincidence of 249.99 kHz pulse wave generated by a function generator and the 25 Hz trigger. Therefore, the timing of the pulse is shifted by 1.6 μs in every event and appeared at the same time of shift for all waveforms in a event. The test pulses are overlaid on the waveforms while HV-switch off between -11 μs to -7 μs as shown in Figure 4.3 (a), so that if once event mismatching occurs, it can be detected as the difference of the timing of the test pulses. The test pulses are distributed to the FADC boards by a test pulse board which induces pulses to all channels on all FADC boards.

During this experiment, the test pulses were inspected for the event mismatching by monitoring their timings of all strips in the first and the end ~ 10 events of each run, where this inspection is performed visually. In addition, the positions of the test pulses were automatically searched by offline analysis and no event mismatching was observed.

4.1.2 Baseline subtraction

The most important things in the baseline subtraction is generation of the template waveforms. However, as previously mentioned, the baseline oscillation depends on the amount of incoming prompt bursts. Therefore, measuring the baseline shape without the beam would result in changes when the beam is introduced. To address this, the DeeMe experiment developed a method to generate templates during measurements.

Figure 4.4 shows the frequency of ADC value in a given sample point. Two ways are considered to evaluate the ADC value of the baseline from that distribution; one is taking average of some waveforms and the other is adopting the most frequent ADC value at each sample point. In the average method, the baseline may be distorted by random hits, which have higher ADC values coming from real hits. Therefore, we adopted the most frequent method in order to obtain the baseline without distortion by real pulses.

Figure 4.3 (b) shows the typical baseline-subtracted waveform.

In this analysis, 100 events are analyzed by the most frequent method to obtain a baseline template, note that these events are used again in the hit finding analysis. The template is recreated when any setting of experiment is changed such as the current through the SBM, HV applied to MWPC, and beam power. In addition, since the setup for this experiment differs from the experiment in the H-Line, prompt bursts do not directly enter the detector. Therefore, while the baseline might not significantly change with the beam rate in this particular experiment, this approach was used as a demonstration for the H-Line experiment.
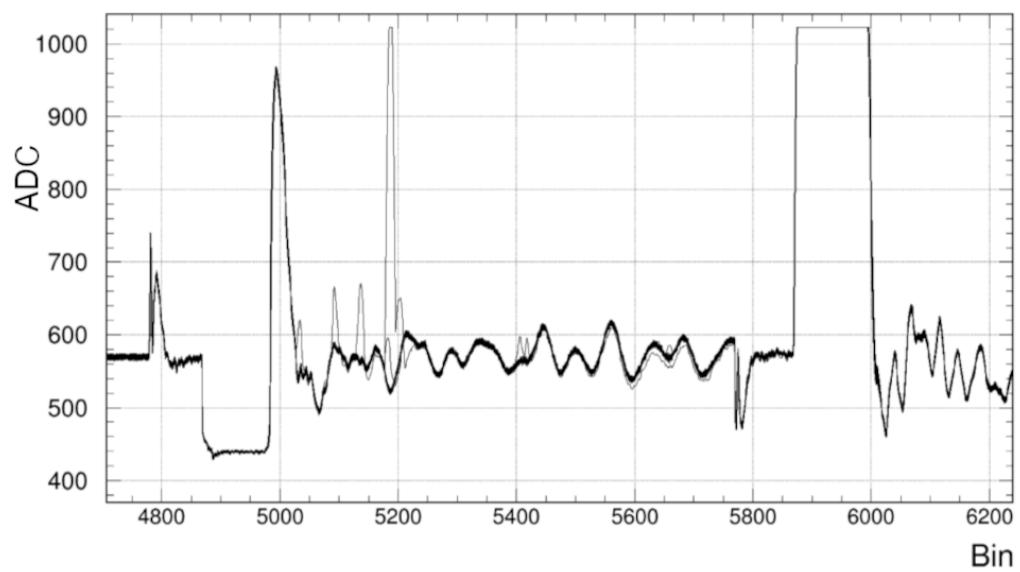
Figure 4.2: The overlay of typical 100 waveforms.
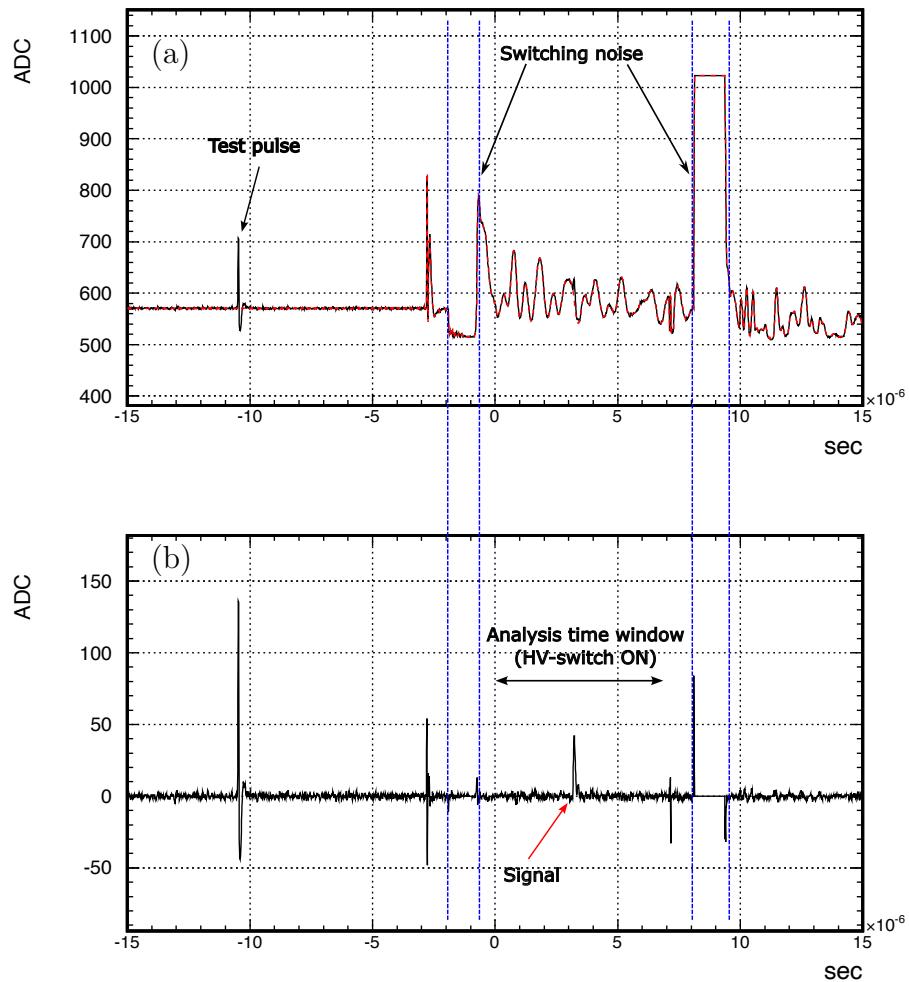
Figure 4.3: (a) The typical raw waveform (black line) and template waveform by using most probable value in each sample point (red line). (b) The subtracted waveform. The analysis time window is from $t_0 = 0$ μs to 7 μs in this figure.
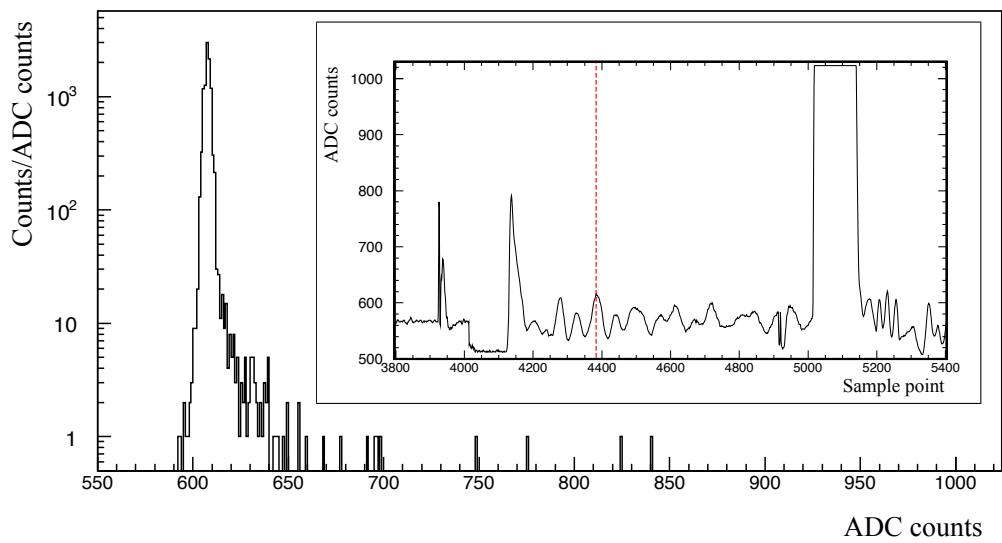
Figure 4.4: The frequency of ADC value in a given sample point indicated by a red broken line on the top right frame that shows a typical waveform of WC0 ch39. This histogram contains 10000 waveforms. The most frequent value of ADC counts is 607 and the mean value is 608. The fluctuation of baseline is 4 ADC in FWHM.

4.1.3 Calibration

As it is shown in Figure 4.3, the baseline-subtracted waveforms shows discrete pulses clearly on a flat baseline. Then the gain, offset, and time of the subtracted waveform are calibrated.

The time calibration between each run has been done [36] by using the hit time distribution of the hodoscope and the HV-switching timing. According to the calibration, the time drift for each waveform is suppressed to less than 33 ns. Note that this had been occurred by an analogue delay module and it was solved now by replacing it to digital one.

Each sample points have 10 ns width and one ADC value equals to 4 mV. The time zero is the start of the analysis time window which is 1.92 μs after the HV-switching.

4.1.4 Common noise across strips

Figure 4.5 shows the two-dimensional ADC distribution after this baseline subtraction. In the figure, we can see vertical stripe considered to come from a kind of noise is still existed with similar shape in all strips in a detector so that it is named as common noise. Common noise cannot be removed by baseline correction, suggesting that the source may be external noise not synchronized with the trigger. The common noises arise to all strips at the same time so that it can be removed by subtracting the waveform of other strips as explained in Section 4.1.5.

4.1.5 Clustering

Charge produced around an anode wire by an avalanche induces opposite charge image on cathode plane. The size of the induced charge image on the cathode plane depends on the distance D between the anode wire and cathode plane. According to [37], when a charge Q produced around an anode wire at the position x_a, the charge distribution $q(x)$ induced on the cathode plane is given by

$$q(x) = \frac{-Q}{4D}\mathrm{sech}\frac{\pi(x - x_a)}{2D}. \tag{4.1}$$

Figure 4.6 shows the charge distribution calculated from Equation (4.1) on the strips around x_a with 3 mm strip width and D is 2 mm for our MWPC.
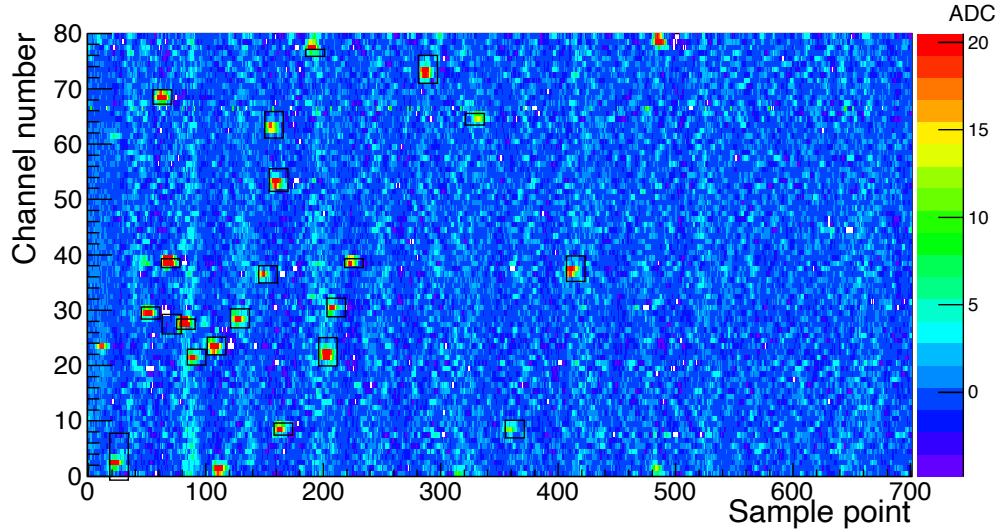
Figure 4.5: The typical 2D image of the ADC value distribution for X strips.

It shows that the original position of the avalanche, x_a, can be reconstructed by using the observed distribution of charges on five adjacent strips. Finding a group of adjacent strips is called clustering.

Figure 4.7 shows the concept of the clustering. In order to collect charge on the strip plane as much as possible, the baseline-subtracted ADC values $a_{i,j}$ of several strips are summed into a cluster ADC value $c_{i,j}$ as shown in Figure 4.7 (a), (b), and (c), where i is the strip number and j is the index number of the sample point. The number of strips summed into a cluster is 5 for X-plane. That for Y-plane is 2 because the width of a strip on Y-plane is five times wider than that on X-plane. Due to the difference of the strip width, total strip number of Y-plane is 16. The procedure of hit finding is the same for X and Y so that the X-plane case is only explained in the following explanations. The cluster ADC value $c_{i,j}$ is calculated from the array of the ADC value $a_{i,j}$,

$$c_{i,j} = \sum_{k=i_1}^{i_2} a_{k,j} - \frac{5(a_{i_1-1,j} + a_{i_2+1,j})}{2}, \tag{4.2}$$

where the second term in Equation (4.2) is common noise the summation period $[i_1, i_2]$ is $[i-2, i+2]$ for X-plane and $[i, i+1]$ for Y-plane. Because of

59

the common noise suppression, the clustering is performed between i=3 to i=76.
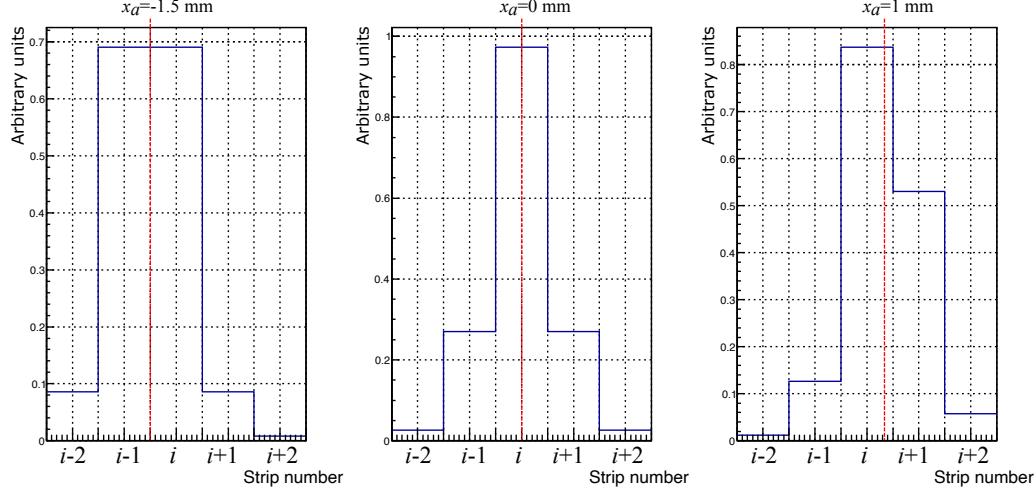
Figure 4.6: Typical charge distributions on strips evaluated from Equation (4.1) for x_a=-1.5 mm, 0 mm, and 1 mm.

In order to get a total charge in a pulse, the integrated cluster ADC value $C_{i,j}$ is defined as

$$C_{i,j} = \sum_{k=0}^{15} c_{i,j+k} \tag{4.3}$$

as shown in Figure 4.7 (d).

The hit position of a cluster is evaluated from the distribution of the charge in the cluster by using centroid method. When a cluster is detected at the strip number l $(3 < l < 76)$, the ADC values of strip number $l \pm 3$ are treated as common noise. The common noise subtraction is performed as

$$a'_{i,j} = a_{i,j} - \frac{((l+3)-i)a_{l-3,j} + (i-(l-3))a_{l+3,j}}{6}, \tag{4.4}$$

where i is restricted in $[l-2, l+2]$. Then the integrated ADC value $A'_{i,j}$ without common noise is

$$A'_{i,j} = \sum_{k=0}^{15} a'_{i,j+k}. \tag{4.5}$$

60
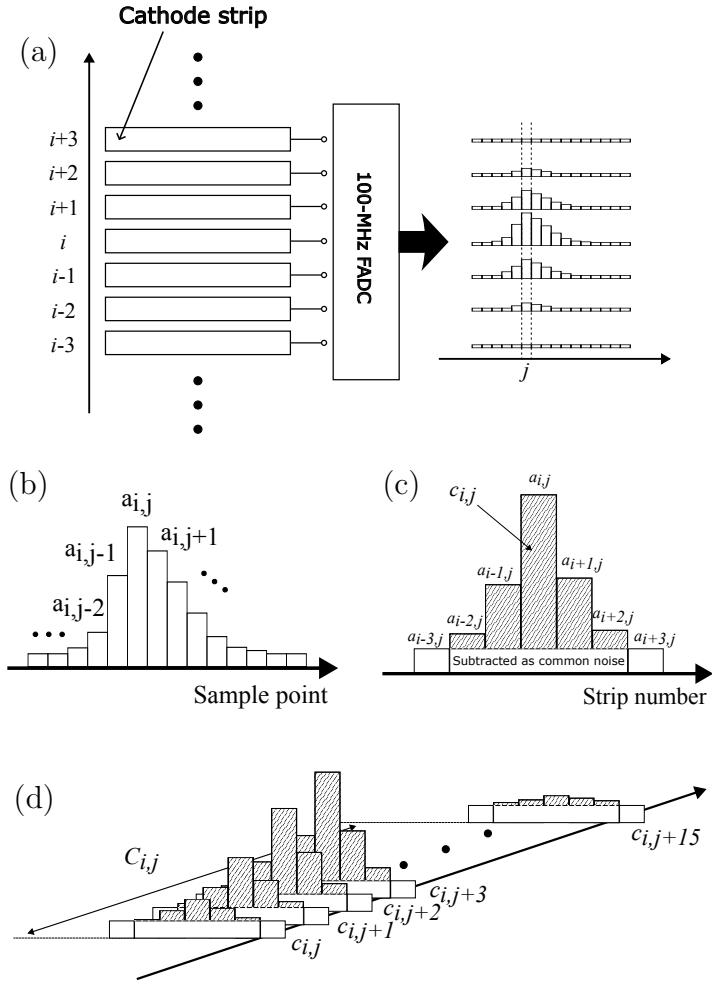
Figure 4.7: The schematic view of the clustering. (a) The charges induced on the cathode strips of WC0–3 are read out by the 100 MHz FADC boards as arrays of ADC value. (b) The baseline-subtracted ADC value $a_{i,j}$. (c) The schematic of the clustering at j. The hatched area represents the $c_{i,j}$. (d) The schematic of the time integration of $c_{i,j}$. The value of $C_{i,j}$ is defined as the summation of the hatched areas.

The $A'_{i,j}$ is used to calculate the hit position x of a cluster as below;

$$x = \frac{\sum_{k=-2}^{+2}(l+k)A'_{l+k,j}}{\sum_{k=-2}^{+2} A'_{l+k,j}}. \tag{4.6}$$

If the gains of adjacent five strips are not equal, the reconstructed hit position x may be affected because of using simple centroid method of induced charge on the strips. Therefore, the uniformity of the gain distribution is required. It will be discussed in section 4.1.7.

Note that the period of integration is fixed as Equation (4.3) and (4.5) in this analysis because the signal pulses are typically ≤ 160 ns as shown in Figure 4.8. The pulse length is defined as the period of $c_{i,j} > c_{\text{thr}}$, where c_{thr} is the threshold to determine the hit time of a cluster and used in the hit finding method as explained later.
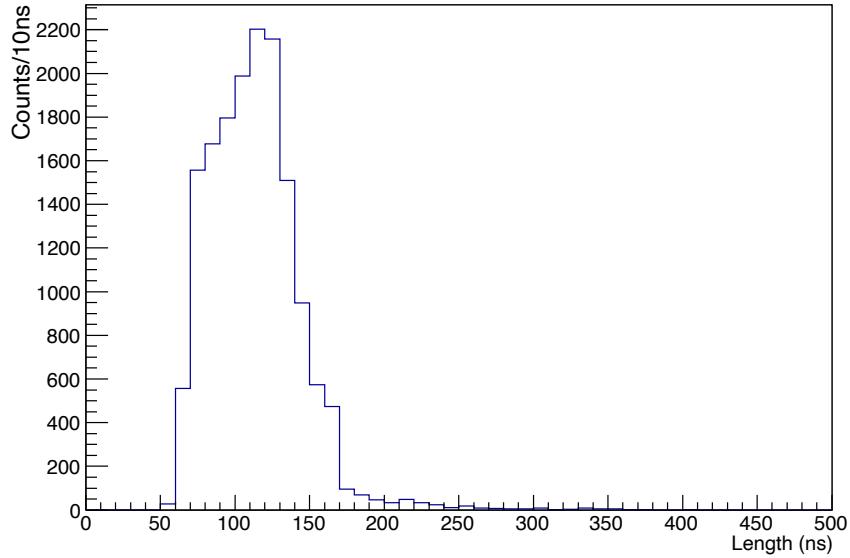
Figure 4.8: The distribution of time length of pulses.

4.1.6   Hit finding

Figure 4.9 shows a typical 2D-histogram of cluster ADC c vs. sample point on a MWPC. The squares in the figure show the hits reconstructed by the

hit finding method described as below;

1. The $c_{i,j}$ for all of i and j are scanned to search the sample point over a given threshold c_{thr}.

2. When $c_{i,j}$ over c_{thr} is found, local maximum point nearest is searched as shown in Figure 4.10. By iterating to move the center of finding region of 5×5 in strip and sample point space to highest point in that region until the max strip and sample point become center of the finding region.

3. The hit information of the central strip number i, sample point j, the charges $c_{i',j}$ $(i' = i - 2, i - 1...i + 2)$, and total charge $C_{i,j}$ on each strip are stored in a list of cluster. Then the sample point is moved to $j + 16$ to search the next hit. The processes of 1–3 are repeated until the scan is finished in all strips and sample points.

4. Overlapping hits are removed from the list of cluster if the difference of the strip number is less than the cluster size (5 for X- and 2 for Y-plane) and that of the sample point is less than 12.

5. The clusters with $C_{i,j} < C_{\text{thr}}$ are rejected from the list.

6. The central position of a cluster is calculated by centroid method using $A'_{i,j}$.

The threshold values c_{thr} and C_{thr} are used to determine the hit time and to discriminate the signals from noise. The values of c_{thr} and C_{thr} are set as Table 4.1 and the analysis to determine them will be described in Section 4.4.

Table 4.1: The threshold values c_{thr} and C_{thr} of WC0–3.

Plane	X		Y	
	c_{thr} (mV)	C_{thr} (pVs)	c_{thr} (mV)	C_{thr} (pVs)
WC0	120	4000	28	800
WC1	120	4000	28	800
WC2	80	4000	28	800
WC3	80	4000	28	800
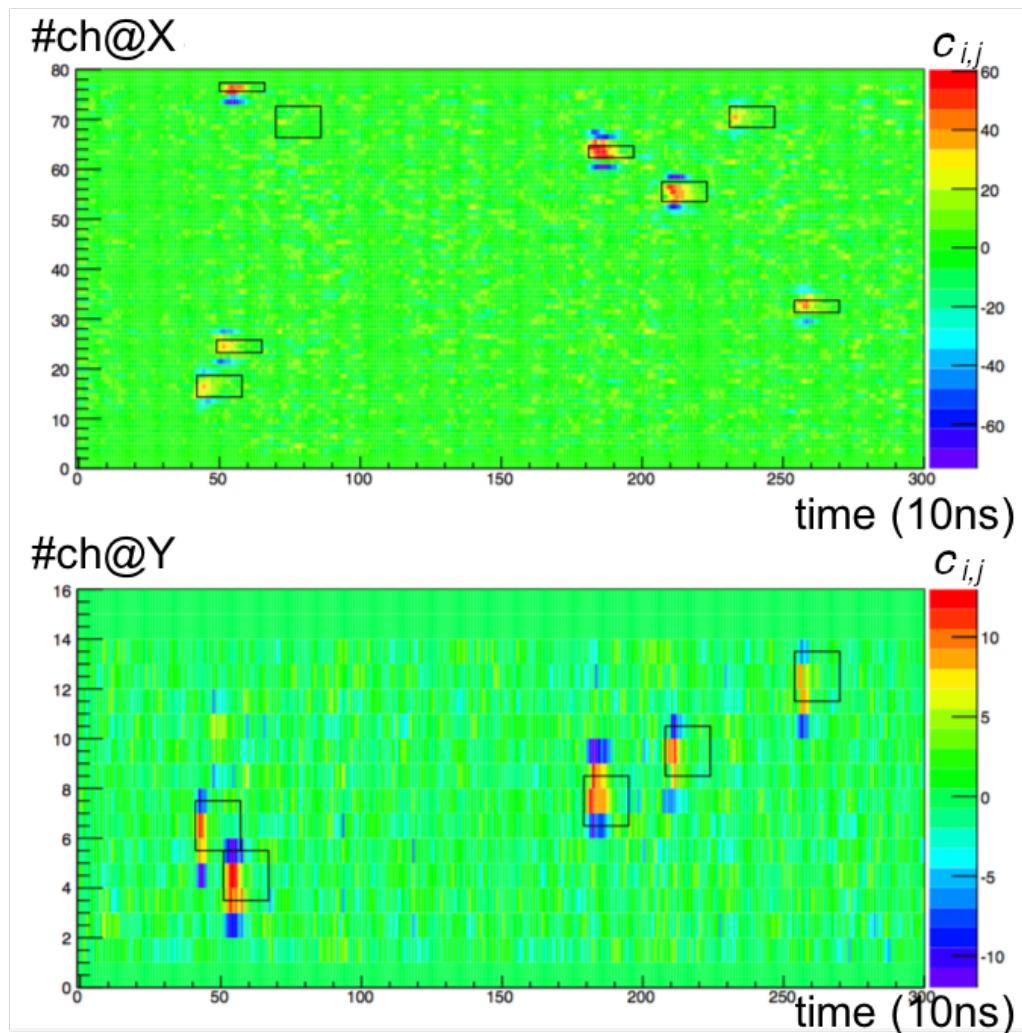
Figure 4.9: The typical 2D image of the $c_{i,j}$ value distribution for X strips (upper) and Y strips (lower). The horizontal axis is time and the vertical axis is the strip number.
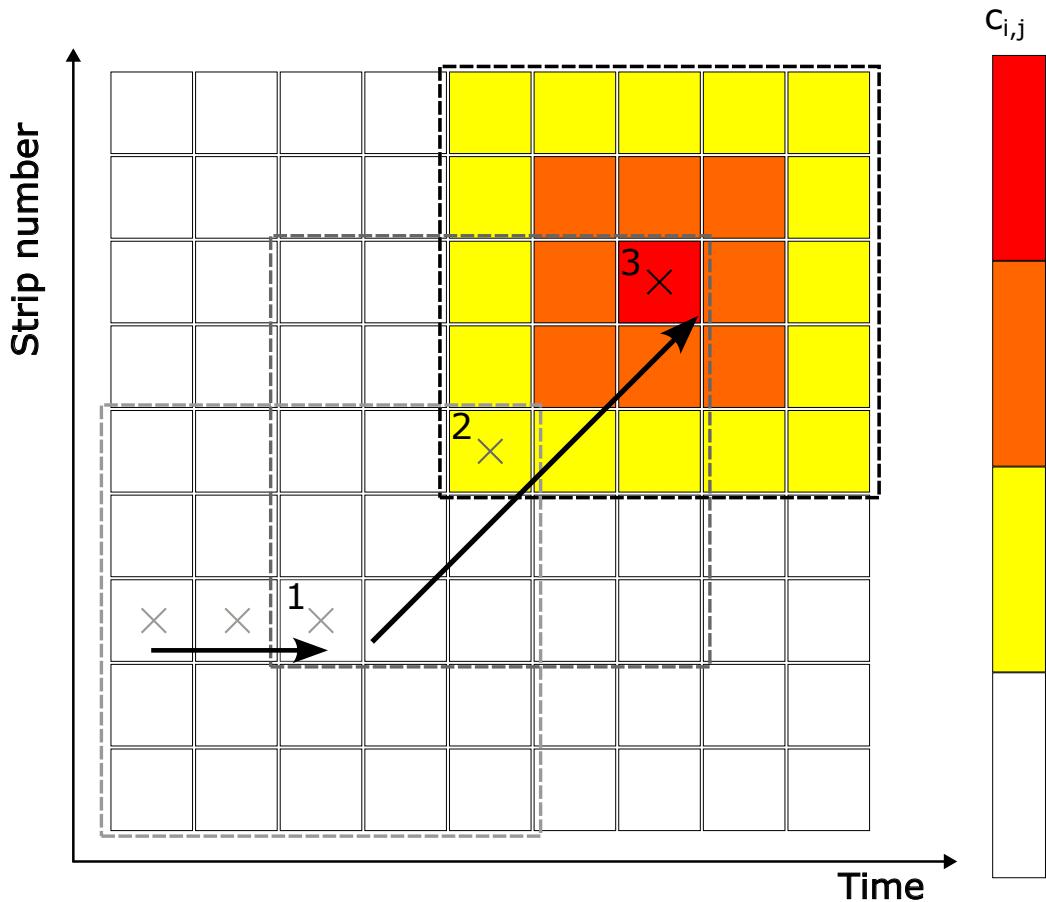
Figure 4.10: An illustration of the search method of local maximum in hit finding. 1) The window moves toward sample point to find the point $c_{i,j} > c_{\text{thr}}$. 2) The center of the window moves to the highest point in former window. 3) The step 2 is repeated until the center is the highest point in the window.

4.1.7 Gain fluctuation

Figure 4.11 shows the typical distribution of $A'_{i_c,k}$, where i_c is the central strip number of a cluster in sample point k. The values of gain of each strip are evaluated by this distribution fitted with seventh-degree polynomial and the highest values are adopted as the gain of the strip.

The gain distributions are shown in Figure 4.12. The fluctuation of the reconstructed position caused by the centroid method with non-flat gain distribution was evaluated as shown in Figure 4.13. The position fluctuations are order of 0.1 mm, which is negligible in this experiment comparing with the multiple scattering by the air, order of 1 cm as discussed in Section 3.2.3.

On the other hand, in the H-Line experiment, the material between the beam window and the WCs will be replaced with Helium gas in order to reduce the material effect. Therefore, the position uncertainty of the multiple scattering is expected to be roughly suppressed by a factor of 5, but the position fluctuation from the gain struggling is still smaller enough to be neglected. In addition, when the fluctuations are not negligible, the gain of each individual strip can be optimized just in analysis. For the simplicity, the gain correction is not performed in this analysis.
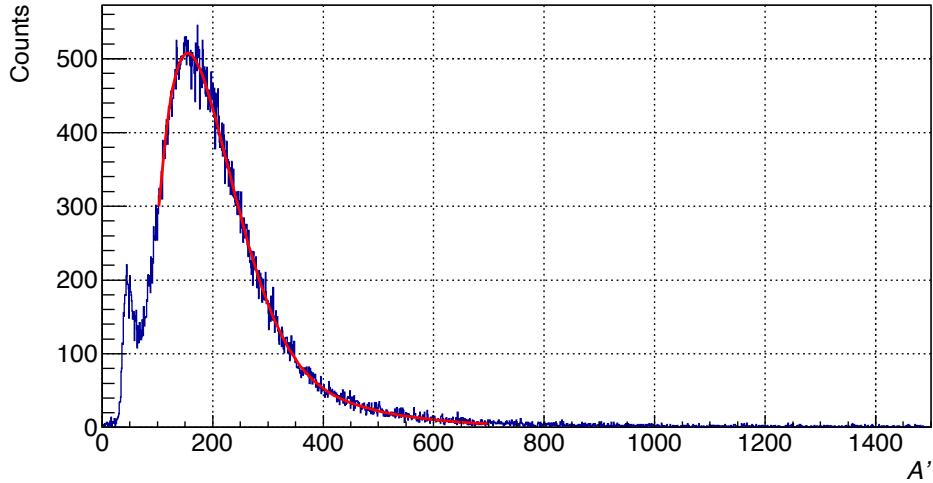
Figure 4.11: Typical $A'_{i_c,k}$ distributions on WC0 strip number=39, where the red line is the polynomial function fitted to the histogram.
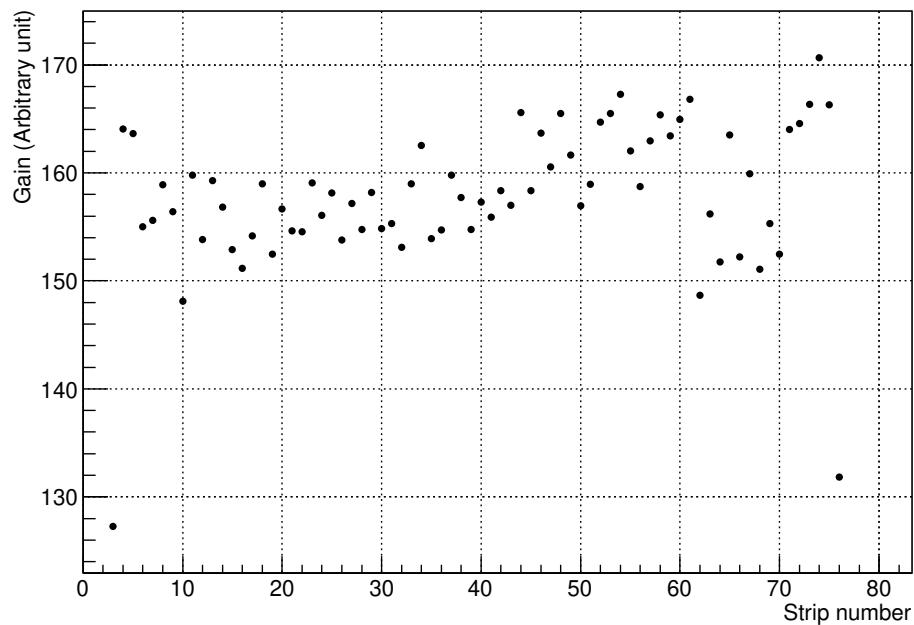
Figure 4.12: The strip gain distribution on WC0.
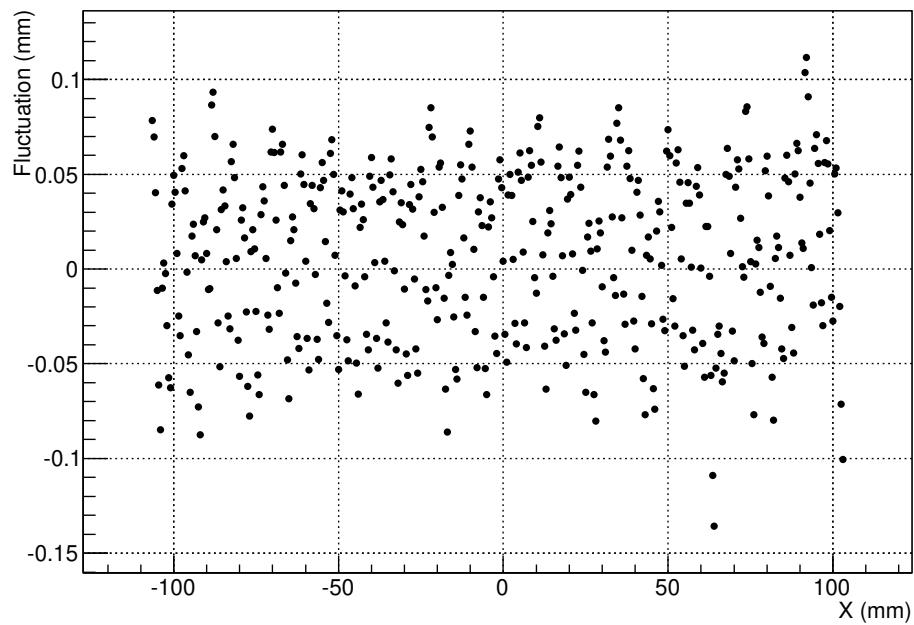
Figure 4.13: The reconstructed position error from the gain distribution evaluated from Figure 4.12.

4.1.8 Distribution of reconstructed hit position

The typical hit position distributions obtained by the clustering method described above are shown in Figure 4.14 and 4.15. Each MWPC has 240 mm × 240 mm detection window but their effective region is 3 or 1 strips smaller for X or Y plane respectively because of the clustering method. The hits $|x| > 11.1$ cm and $|y| > 10.5$ cm are rejected as a fiducial cut because the sensitive area of WC0–3 shrinks by three or one strips due to the clustering.

Extreme number of hits had been observed in Figure 4.14, especially in WC2. Discharge in the MWPC fiducial volume was suspected, but the discharge-like pulse shape was not appeared in the raw waveforms. A typical time distribution of hits on the noisy strips is shown in Figure 4.16. The strips with extremely large hit numbers contain some spike-shape distributions in the time spectrum. Thus, instability of the baseline in time direction were suspected of these spikes. Figure 4.17 shows correlation between the baseline waveform and spikes for WC2 ch66. Several but not all spikes seem to arise around the top of the baseline. However, any irregular have not been specified in the baseline of that strip. On the other hand, these timings seem to be different in each strip as shown in Figure 4.18. Therefore, the noisy strip can be suppressed by taking time-coincidence as shown in Figure 4.19. In this experiment, the peak on ch66 is also suppressed but still remains even if taking coincidence with several channels.

It had been revealed that this problem also happened in the data in 2019 experiment with the new preamplifiers. The distributions of the hit on the strip with 2019 data are shown in Figure 4.20 with the time-coincidence analysis. This simple way to suppress the noisy strips seems to work well in the latter experimental setup so that taking time-coincidence in hit finding should be required in future analysis.

On the other hand, a typical distribution of hit number vs event number is shown in Figure 4.21. It clearly indicates that the noises on ch 61, 65, and 66 on WC2 suddenly appeared from the specific event number and the high hit-rate was sustained continuously across the run. It is considered that the baselines of these strips were changed at the specific event by external reason. At first the baselines had been generated when the measurement condition was changed as mentioned in Section 4.1.2. We updated the procedure of baseline creation to prepare for every run. As a result, the hit distribution of the following run became flat as shown in Figure 4.22. On the other hand, the sudden change of baseline itself is still alive in the specific run that

the problem had been happened. These remained noises are expected to be eliminated by the coincidence method. Coincidence hits on each plane are searched to obtain the candidates of tracks before track fitting analysis. The coincidence analysis is performed in that step so that the effect of these noisy strip is considered to be suppressed without additional cut condition.
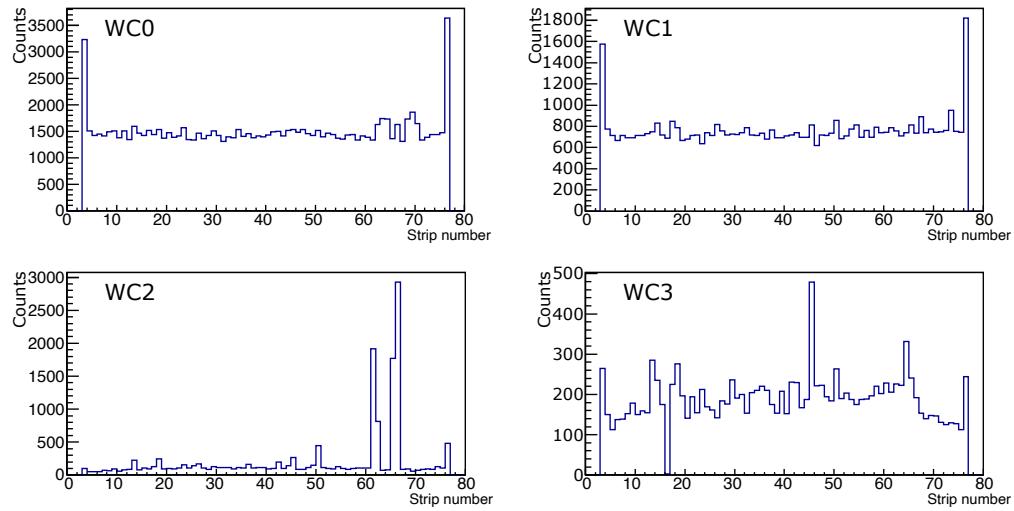
Figure 4.14: The distributions of the hit position obtained by the clustering and hit-finding method on WC0–3 X-plane.
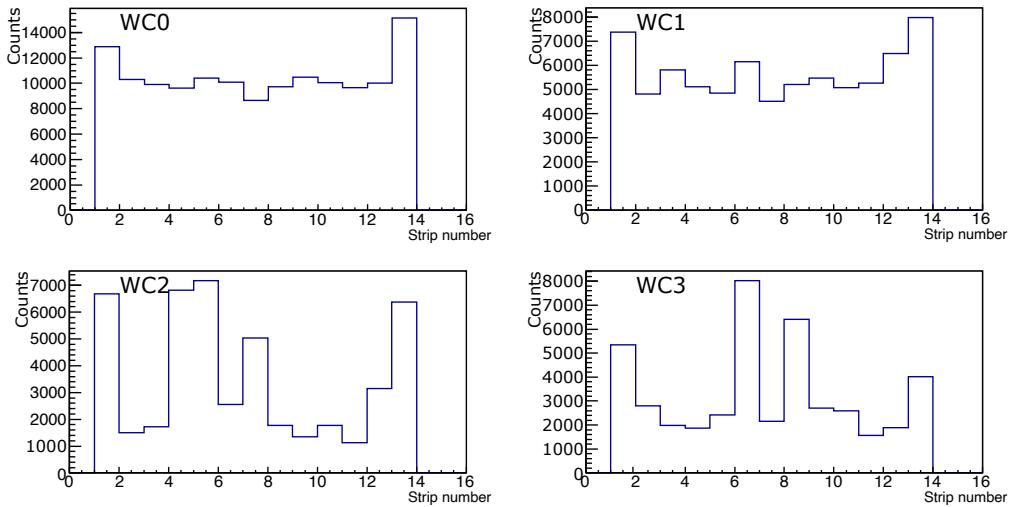
Figure 4.15: The same distributions of Figure 4.14 but Y-plane.
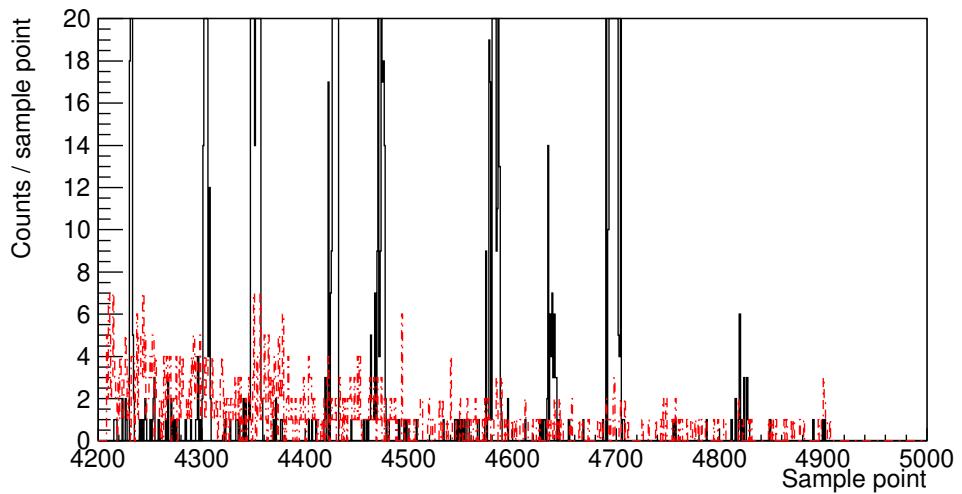
Figure 4.16: The time distributions of hits on WC2 ch66 (noisy strip) in solid black line and WC2 ch30–40 summation (calm strips) in red broken line.

71
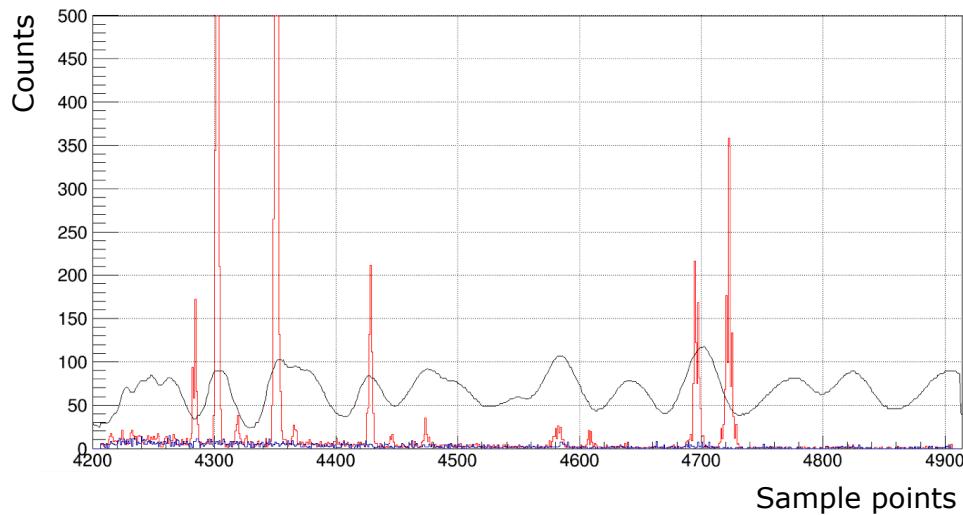
Figure 4.17: time distributions of hits on WC2 ch61, 66 (solid blue and red line, respectively) and the baseline waveform of WC2 ch61 (black line).
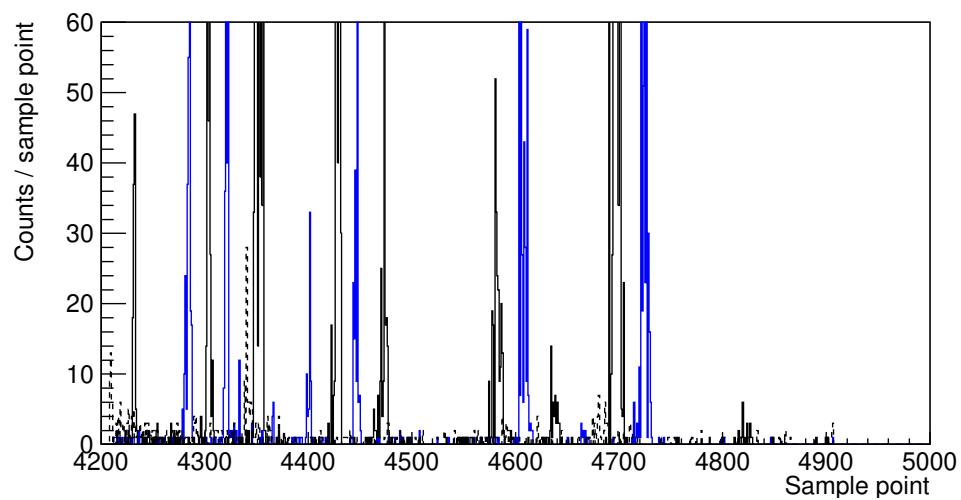
Figure 4.18: The time distributions of hits on WC2 ch61, 66 (solid blue and black line, respectively), and WC3 ch45 (black broken line).
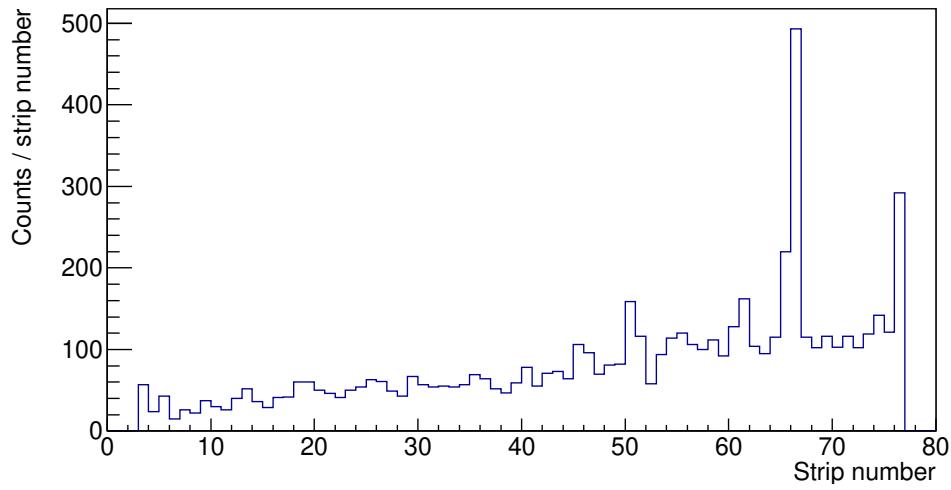
Figure 4.19: The distribution of the hit position on WC2 with X-Y plane coincidence.
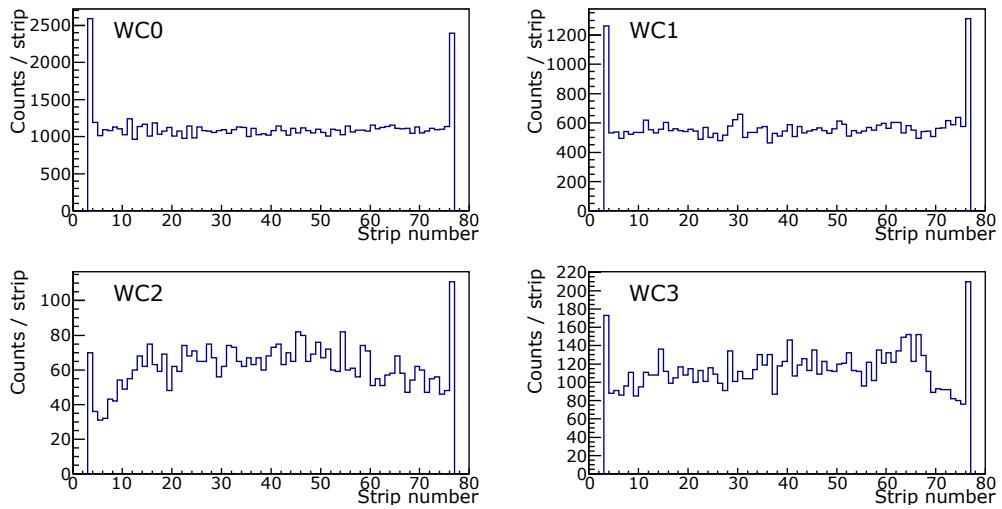
Figure 4.20: The distributions of the hit position in 2019 data with X-Y plane coincidence analysis.
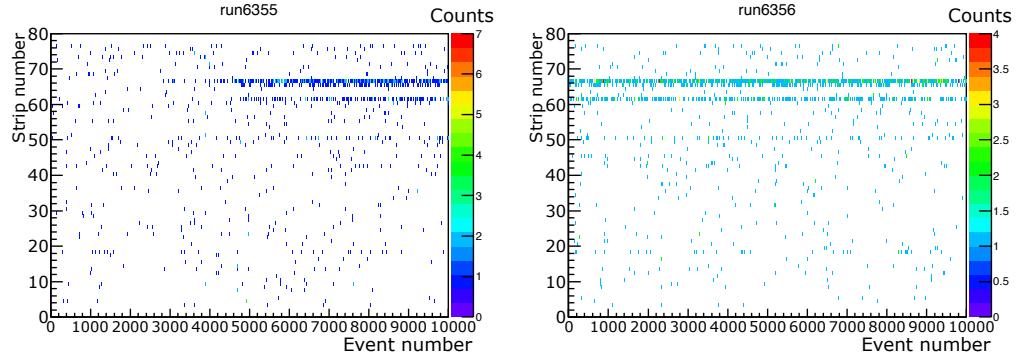
Figure 4.21: The hit distribution on event number vs. strip number of run6355–6356 on WC2.
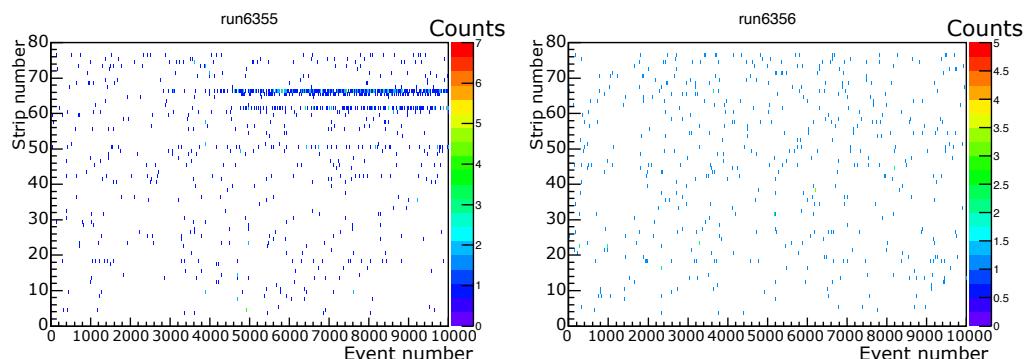
Figure 4.22: The hit distribution of run6355–6356 on WC2 with generating baseline for all run.

4.1.9 Spurious hits

As shown in Figure 4.23, it had been observed that a hit induced by a real particle produces several spurious hits. It is considered that the spurious hits are due to the common noise reduction in the clustering method. Figure 4.24 shows the process how spurious hits rise. When a particle passes through a strip i, the values of $c_{i\pm3,j}$ become negative or enough small in the positive part of a pulse ($a_{i,j} > 0$), whereas an undershoot of a pulse raises $c_{i\pm3,j+\alpha}$ because of $a_{i,j+\alpha} < 0$, where α is a length from start of a pulse to undershoot. As a result, several spurious hits are produced after a hit. Due to their nature, the spurious hits appear near the real hit, so that the track is duplicated by the spurious hits. The region in which the spurious hits appear is very specific as shown in Figure 4.25. If any pair of hits whose distance is [3,4] strips and [100, 360] ns are found, the later hit in the pair is removed.
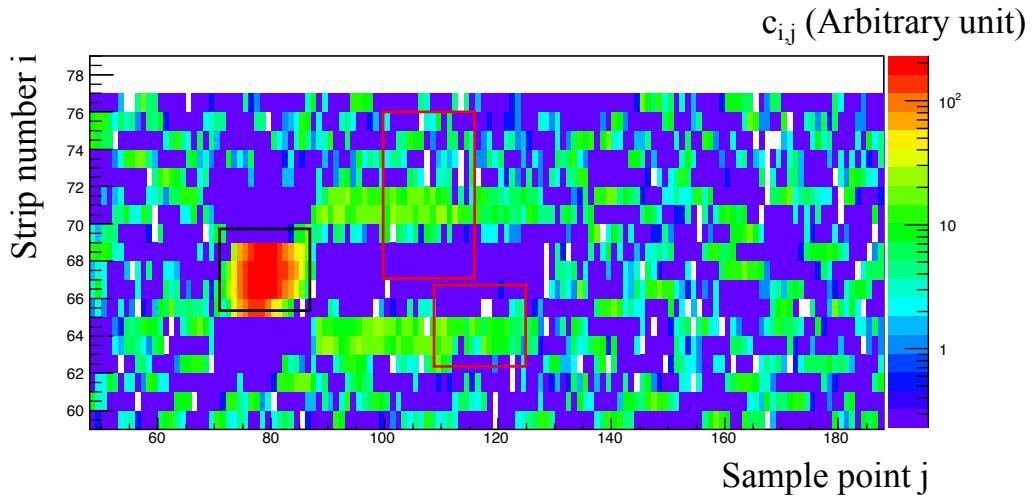
Figure 4.23: The typical event display including the spurious hits.
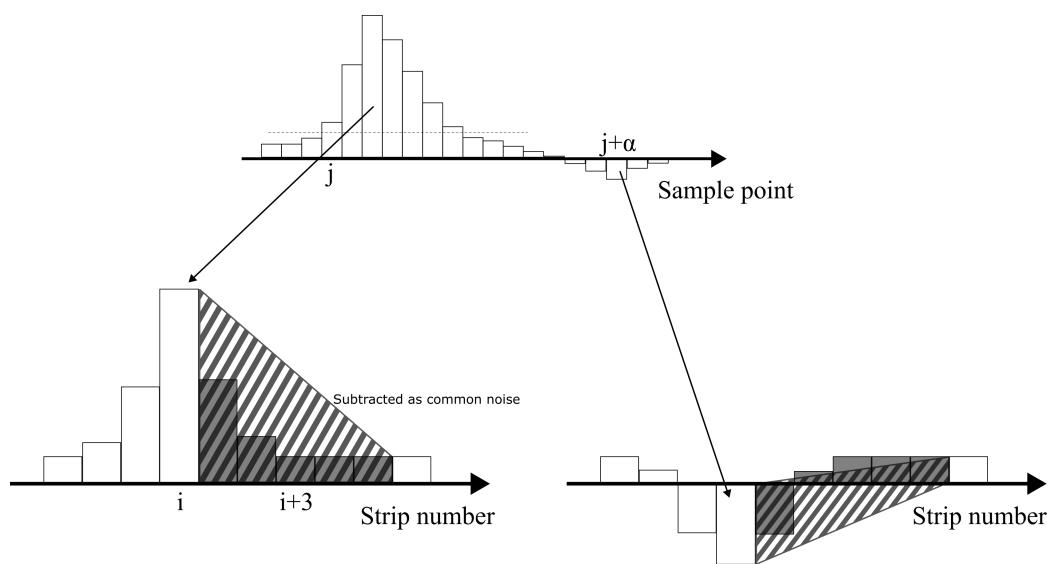
Figure 4.24: A schematic view of the process of generating spurious hits.
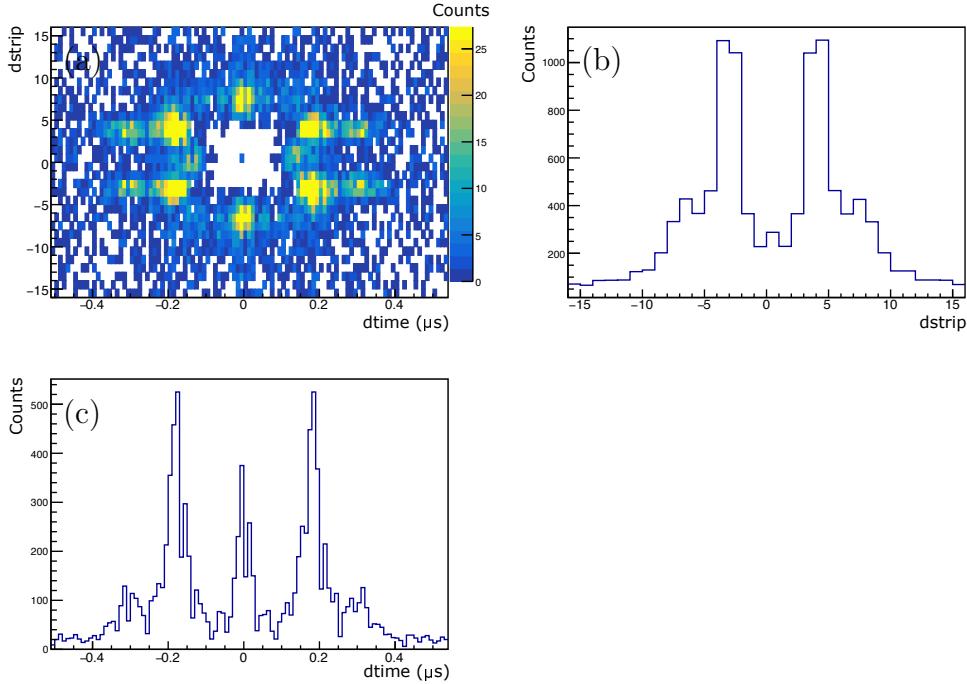
Figure 4.25: (a) A 2D histogram of dtime vs dstrip, where dtime and dstrip are the difference of hit time and strip number of any two hits. From the multiple hits on WC2, any two hits were selected, and the differences in their hit times and hit positions were calculated as dtime and dstrip for all combinations of hits. Note that combinations with swapped order were not excluded, resulting in pairs that are point-symmetrical. Specifically, the peaks at dstrip=4 and dtime=-180 ns is the same combination with dstrip=-4 and dtime=180 ns. (b, c) Projections along the X and Y axis, respectively.

4.2　Track reconstruction

GENFIT is used for the tracking analysis. It is a generic toolkit for various high energy physics experiments [38]. The track fitting algorithm is the Extended Kalman Filter.

4.2.1　Kalman filter

Kalman filter is one of recursive processing digital filter. It is usually used for the dataset with the discrete sample points. This algorithm defines the state vector x_k which contains some suitable track parameters for a system, where k is the index of a sample point. Note that x_k is the *true* state vector so that x_k itself is unknown. To obtain good approximation of x_k is the goal of Kalman filter. There are two steps to estimate x_k; one is **prediction step** to calculate a *predicted* state vector $x_{k|k-1}$ and the other is **filtering step** to calculate a *filtered* state vector $x_{k|k}$. When the estimation of the k-th sample point, the predicted state vector $x_{k|k-1}$ is calculated by using the filtered state vector in previous one step $x_{k-1|k-1}$ which includes all measurement information up to $k-1$. Then in the filtering step, the state vector is updated to $x_{k|k}$ by using predicted state vector $x_{k|k-1}$ and k-th measurement vector m_k. The measurement vector m_k is expressed by using true state vector x_k as

$$m_k = H_k x_k + v_k, \tag{4.7}$$

where H_k is the linear transformation matrix from the vector space of x_k to that of m_k, and v_k is the noise of the position measurement. The dimension of H_k is $\dim(\mathrm{m_k}) \times \dim(\mathrm{x_k})$. The errors of predicted and filtered state vectors are expressed by using covariance matrices. The predicted covariance matrix $C_{k|k-1} = Cov(x_k - x_{k|k-1})$ contains effects from multiple scattering and energy loss straggling.

　　The updated state vector $x_{k|k}$ is calculated as below,

$$x_{k|k} = x_{k|k-1} + K_k r_{k|k-1} \tag{4.8}$$

Where K_k is called Kalman gain. The Kalman gain K_k, filtered covariance matrix $C_{k|k}$, a residual vector $r_{k|k-1}$, and a covariance of the residual R_k are

$$
\begin{aligned}
K_k &= C_{k|k-1} H_k^T R_k^{-1}, \tag{4.9} \\
C_{k|k} &= (I - K_k H_k) C_{k|k-1}, \tag{4.10} \\
r_{k|k-1} &= m_k - H_k x_{k|k-1}, \tag{4.11}
\end{aligned}
$$

and

$$R_k = H_k C_{k|k-1} H_k^T + V_k, \tag{4.12}$$

where I is identity matrix and V_k is covariance of the measurement noise v_k.

The χ_k^2 of the k-th hit is

$$\chi_k^2 = r_{k|k}^T (V_k - H_k C_{k|k} H_k^T)^{-1} r_{k|k}. \tag{4.13}$$

Then, total χ^2 is calculated

$$\chi^2 = \sum_{k=0}^{K} \chi_k^2. \tag{4.14}$$

4.2.2 Tracking procedure

Track reconstruction code include track-parametrization and track-extrapolation codes and they are based on a Runge-Kutta extrapolator. The predicted state vector $x_{k|k-1}$ and predicted covariance matrix $C_{k|k-1}$ are obtained in the extrapolation process.

The state vector is 5-dimensional and contains two hit coordinates, two direction of momentum, and a kind of magnitude of momentum $q/|\vec{p}|$, where q is the charge of the particle and $\vec{p}$ is the 3-momentum of the particle. The covariance V_k is 1×1 matrix and it is equivalent to the position resolution of our detector σ_x for X-plane and σ_y for Y-plane. When obtaining the predicted covariance matrix, the material properties are used to calculate the material effect of detectors for example ionization energy loss, multiple scattering, and Bremsstrahlung. An adaptive step-size for the extrapolation is calculated in the track representation code and its minimum and maximum values are set to 1×10^{-5} cm and 1×10^{-2} cm respectively in this analysis.

The above Kalman-filtering procedure can be processed from WC0 to WC3 or from WC3 to WC0 and they are named *forward tracking* and *backward tracking* respectively. The track fitting process goes and returns many times even if it starts from forward or backward. The definitive track information is the mean of the forward and backward tracking results.

The coincidence hits as the candidates of tracks are searched from X- and Y-planes of WC0–3 in a time window of 20 sample point width (=200 ns). At least five planes are required for track fitting to compute 5-dimensional the state vector. While the number of planes containing the coincidence hit

are denoted as n_X^{plane} for X-plane n_Y^{plane} for Y-plane, $n_X^{\text{plane}} + n_Y^{\text{plane}} > 5$ and $n_X^{\text{plane}} \geq 3$ are required. Note that the X-direction information is much more important to estimate the momentum than Y-direction.

The spectrometer information such as B field and MWPC position and structure is used in the tracking analysis to calculate the momentum and the material effects. In addition, a dummy plane is set in $45°$ of the sector magnet as shown in Figure 4.26. This plane is a virtual detector whose resolution is large enough to ignore its effect. The GENFIT tracking procedure does not work without the dummy plane. It is considered that the extrapolator can not reach to next plane owing to $90°$ angle between WC1 and WC2 as shown in Figure 4.27.

There are two type of tracking analysis, one is usual tracking with 4-MWPCs and the other is tracking with 3-MWPCs (3WC tracking). The 3WC tracking is used to analyze the efficiency and resolution of any one MWPC. The minimum number of required plane in trackfit is five as already mentioned, so that trackfit is able to be executed with X and Y hit position information of only three MWPCs. The reconstructed track is able to be extrapolated to an unused MWPC in tracking and the obtained position on the MWPC is called *extrapolated position*. The extrapolated position is compared with the hit position detected by the hit finding on the unused MWPC for analysis of the MWPC itself such as the threshold optimization, resolution estimation, and detection efficiency estimation as explained in later sections.

4.2.3 Material effect

GENFIT can estimate the material effect of detectors. In this analysis, muon is utilized as the tracking particle to avoid the over estimation of material effect for electron.

All materials on the tracking axis such as aluminum foil and wires as shown in Table 2.1 are converted to equivalent thickness of kapton. Total thickness of each MWPC is equivalent to 0.18 mm of kapton. The spectrometer had been set up in air so that the effect of air between each detector is included to each detector. Table 4.2 shows the converted thickness of the air between each plane and total thickness.
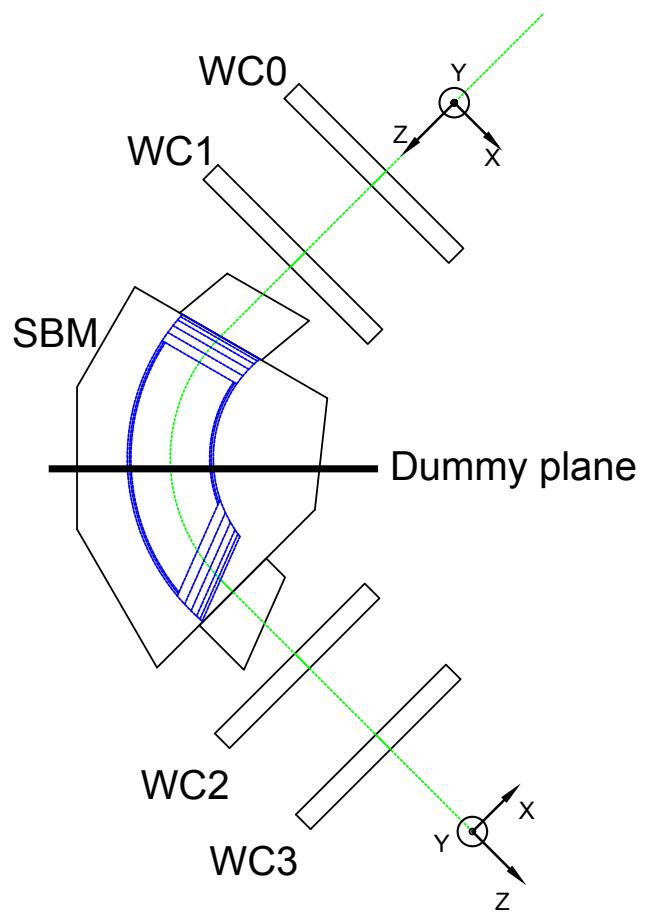
Figure 4.26: The geometry in tracking analysis including the dummy plane.
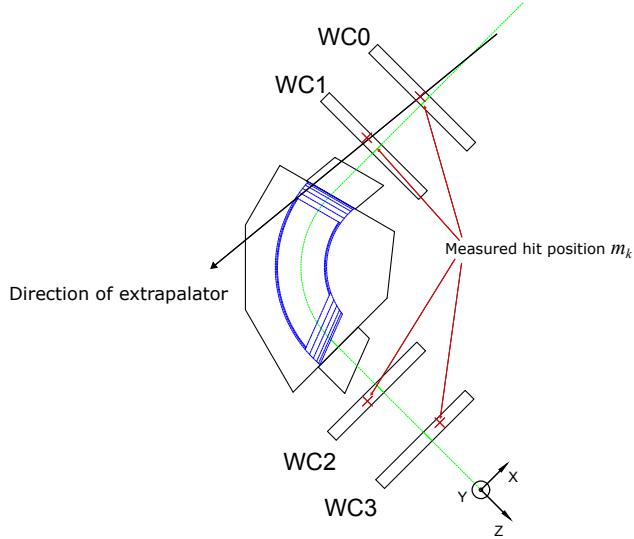
Figure 4.27: The illustration of the misdirection of the extrapolator without the dummy plane.

4.3 Tracking performance

Validation for the tracking process is performed by using pull function, p-value, the position fitted on each plane, and the hit time distribution.

4.3.1 Position residual and pull function

In order to check the discrepancy between the measured hit position x_m and fitted position x_f, the residual r is defined as $r = x_f - x_m$ which corresponds to Equation (4.11).

The pull function is a probe of goodness of a track fitting and it is defined as r/σ, where $\sigma = \sqrt{\sigma_m^2 - \sigma_f^2}$, σ_m is a deviation of x_m, and σ_f is that of x_f. The distribution of the pull function is a Gaussian with mean ~ 0 and deviation ~ 1 ideally.

The r distributions are shown in Figure 4.28 and the pull function distributions are shown in Figure 4.29. The resolution is set as $\sigma_x = 0.7$ mm and $\sigma_y = 3.5$ mm in this analysis. The biased structures are appeared in both the measurement and the MC generated data. It is considered to be caused not by the track model but by the tracking algorithm. The shortage of the

Table 4.2: Converted thickness of the WC0–3 including the air between each detector.

	Air thickness (mm)	Kapton-equivalent thickness (mm)	Total thickness (mm)
WC0	540	0.76	0.94
WC1	400	0.56	0.74
Dummy	1280	1.8	1.8
WC2	280	0.40	0.57
WC3	400	0.56	0.74

detector planes is suspected with Kalman-filter. However, for the moment, the track fitting is performed with this tracking algorithm in this analysis because the behavior of the pull functions of both data and MC are the same.

4.3.2 p-value

The probability p is defined with χ^2 as

$$p = \int_{\chi^2}^{+\infty} \frac{1}{\Gamma(n_d/2)2^{n_d/2}} x^{n_d/2-1} e^{-x/2} dx, \tag{4.15}$$

where n_d is number of degree of freedom (NDF). The distribution of p-value is considered to be flat if the track model agree with data.

The histogram p-value distribution for fitted track is shown in Figure 4.30. According to this histogram, the probability cut is applied to less than 0.1.

4.3.3 Time distribution

The time distribution of reconstructed tracks is shown in Figure 4.31. Due to the time dependence of the detection efficiency caused by amplifier saturation, region of 0–3 μs is unstable. Exponential fitting was applied to Figure 4.31 in the region from 3 μs to 7 μs and the lifetime was evaluated 2.227 ± 0.005 μs.

The structure in 0–3 μs was considered to be caused by the instability of the detection efficiency with the former preamplifiers. Therefore, the track
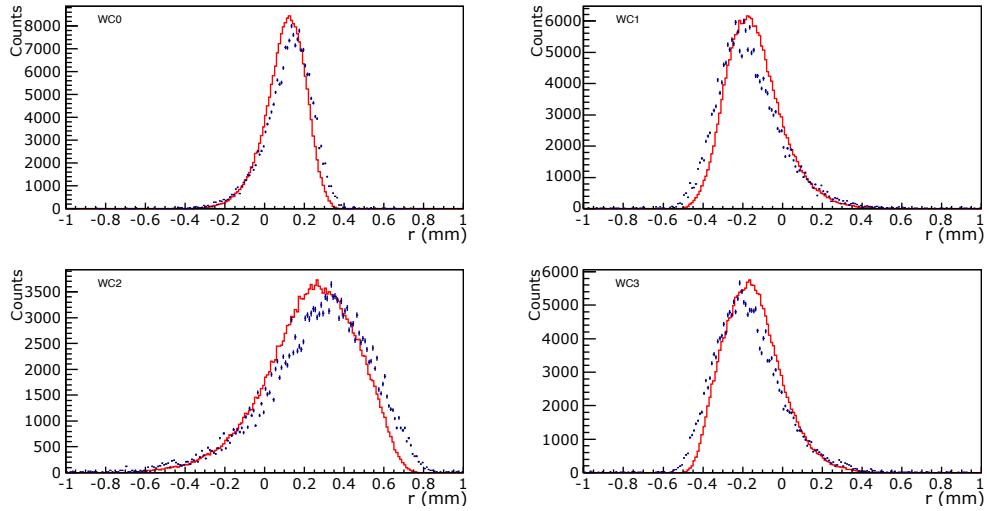
Figure 4.28: The residual r distribution with 4-MWPC tracking, where the blue points with error bar and red line show the measured data and simulation data respectively.
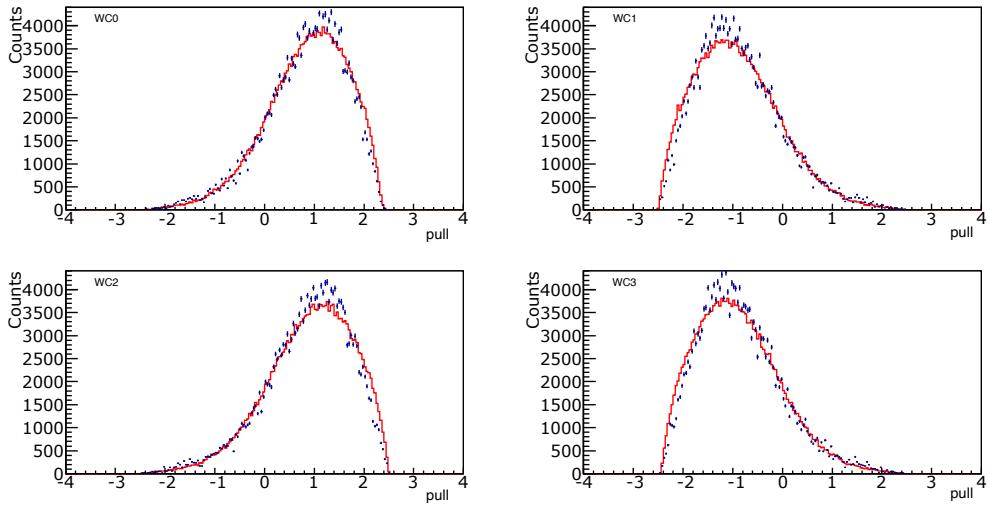
Figure 4.29: The pull function distribution, where the blue points with error bar and red line show the measured data and simulation data respectively.
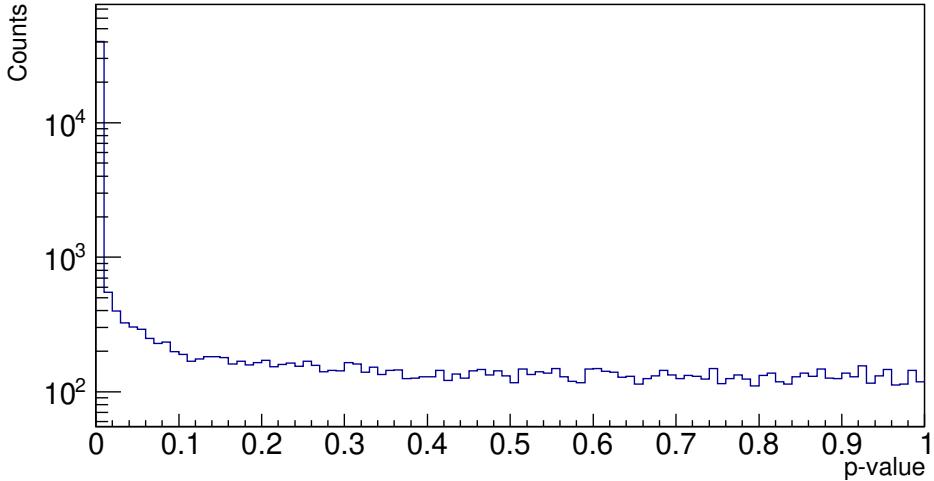
Figure 4.30: The p-value distribution.

time distribution was also expected to be improved in 0–3 μs with the up-dated preamplifiers in 2018. However, that of 2019 data taken by using these preamplifiers were not improved as much as we expected. The structure is also appeared in 0–3 μs of the hit time distribution of each detector as shown in Figure 4.32. The structure is already observed in the hit finding process as shown in Figure 4.33. Therefore, the hit number fluctuation is happened before the tracking process. Figure 4.34 shows the total charge comparison between the hits in the top and bottom region of the fluctuation. In addition, the shape of hit time fluctuation synchronizes with the oscillation of the law waveform as shown in Figure 4.35. It is considered that either the gas gain of the MWPC itself fluctuated or the signal amplification rate varied in syn-chronization with the baseline. If the gas gain of the MWPC fluctuated, it would mean that the HV applied to the wires fluctuated synchronizing with the baseline vibration. However, in that case, the same fluctuation should oc-cur during the bench test mentioned in Section 2.3.2, which would contradict the stable detection efficiency observed during the bench test. Similarly, the possibility of signal amplification rate fluctuations seems inconsistent with the bench test results, as the same MWPC, preamplifier, and FADC were used. On the other hand, one difference between this experiment and the bench test is the hit rate in the MWPC. In the bench test, the detection efficiency was measured by sandwiching a single MWPC between trigger de-

85

tectors, and the hit rate was only a few hits per trigger. In this experiment, the hit rate ranged from a few hits to several tens of hits per trigger in WC0–1, and about one hit per trigger in WC2–3. As shown in Figure 4.33, the degree of oscillation in WC2–3, where the hit rate is similar to that of the bench test, is smaller compared to WC0–1, where the hit rate is higher. It is suggested that the gain may fluctuate in synchronization with the baseline when the hit rate exceeds a certain level, and this possibility needs to be investigated in future research. From another point of view, it implies that the gain calibration in time direction may solve this problem. In this analysis framework, the gain correction only for individual strips can be performed. If the gas gain or signal amplification varies along time direction, the gain correction along time may be able to cancel the time dependence of the gain.
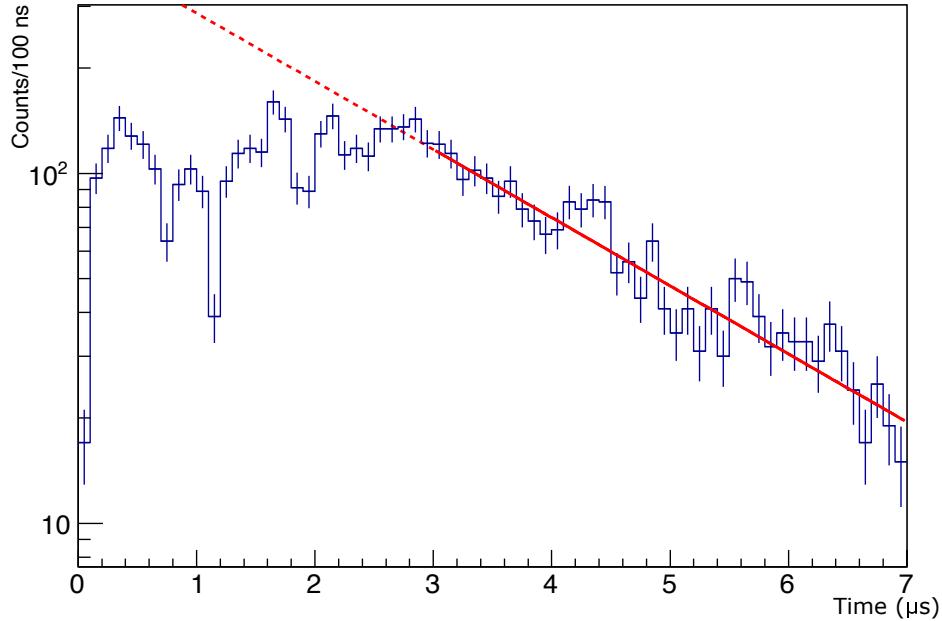
Figure 4.31: The time distribution of the reconstructed tracks, where the vertical axis is logarithmic scale. The red line shows the exponential fit.
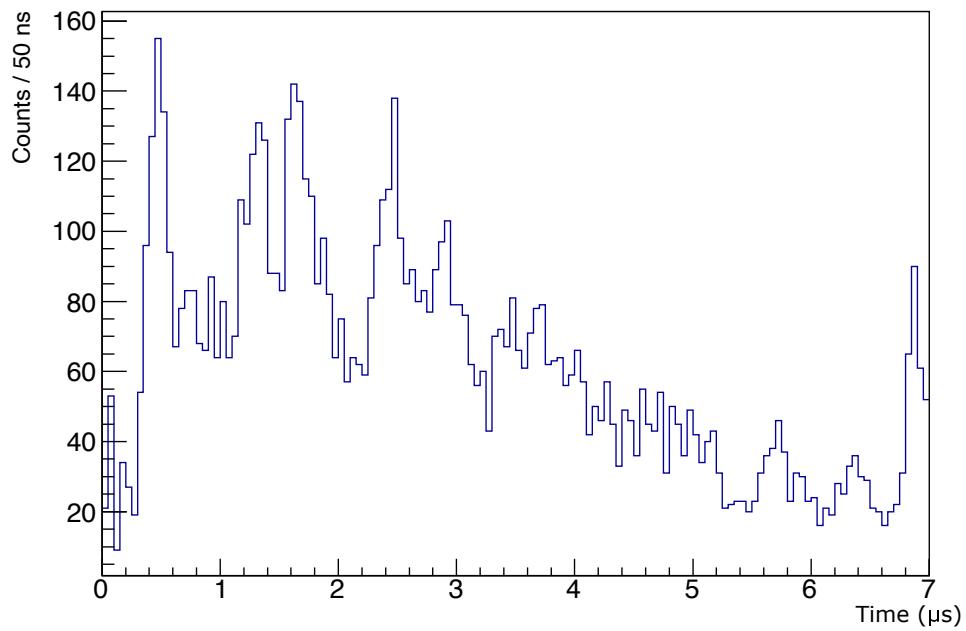
Figure 4.32: The track time distribution of 2019 data. The filled entries are the track reconstructed by the tracking.
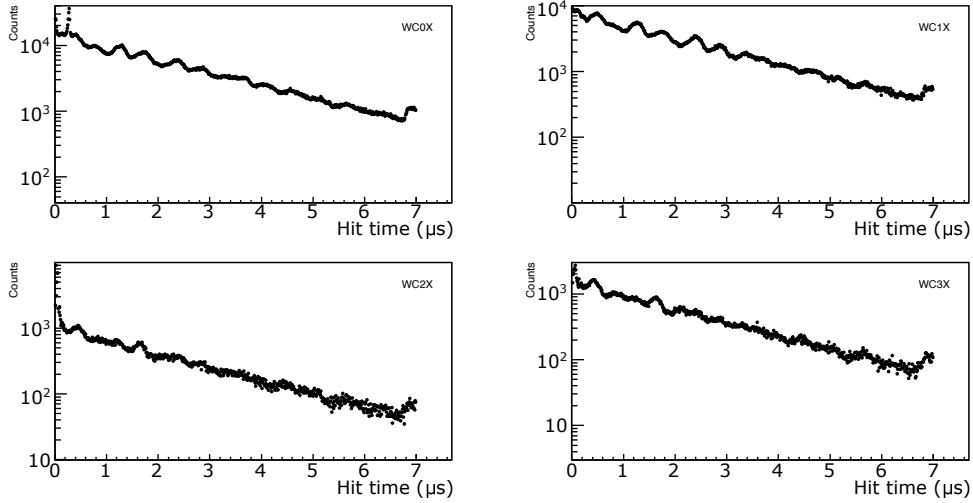
Figure 4.33: The time distributions of 2019 data. The filled entries are the hit number reconstructed by the hit finding method.
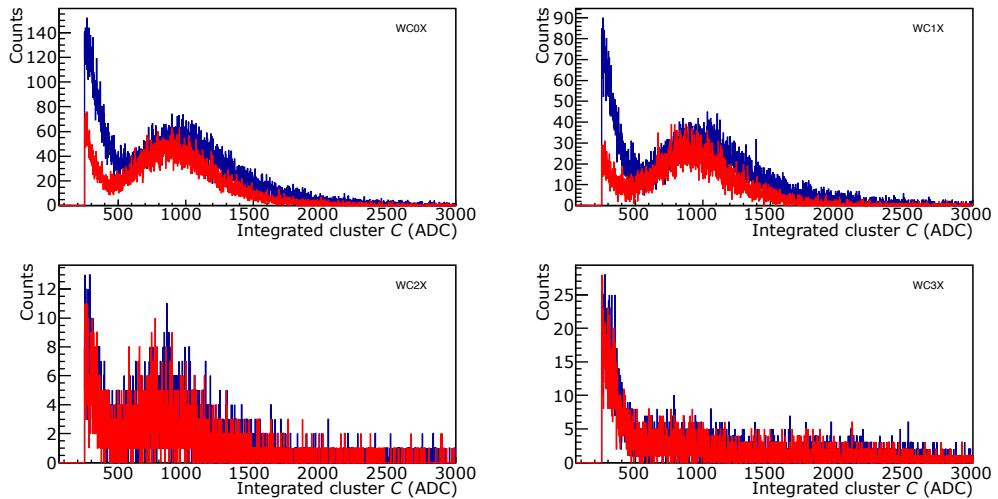
Figure 4.34: The C distribution in each detector, where the blue and red histogram show that of 1.28–1.33 μs and 1.45–1.50 μs, respectively.

88
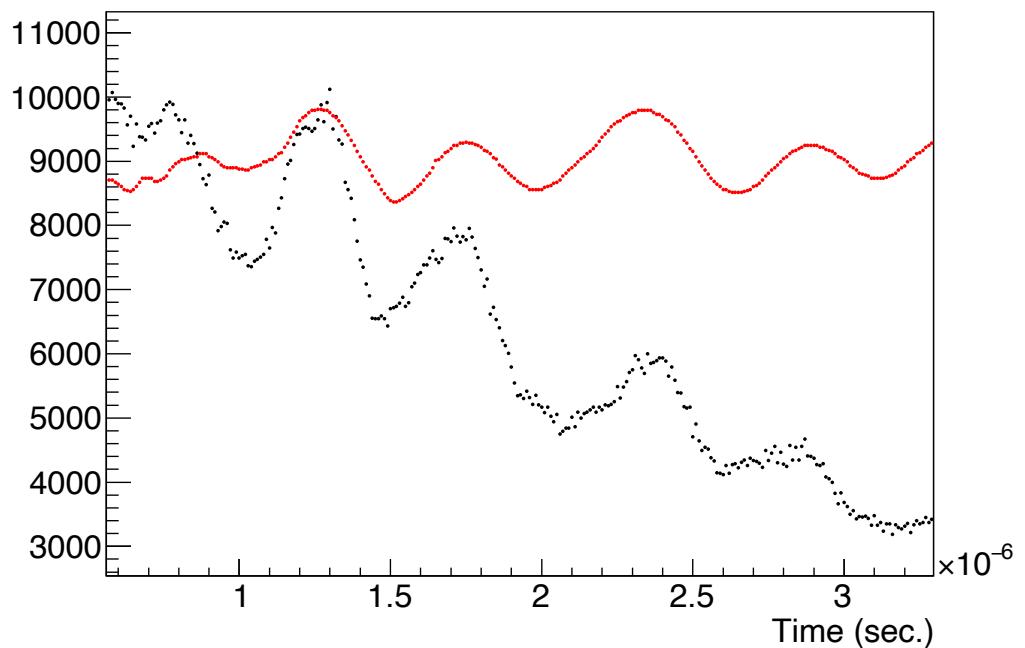
Figure 4.35: The hit time distribution of WC0 (black) and a baseline template of a strip in WC0 (red), where the baseline is magnified by arbitrary factor.

4.3.4 Fitted position

The positions on target and dummy plane are able to be extrapolated by track fitting as shown in Figure 4.36.

The comb-like structure can be seen in Y-plane in Figure 4.37. This structure is considered to reflect the Y-strip size because the repetition distance of each spike is 1.5 cm.

A detailed explanation will be provided in Section 5.5, the tails of the momentum distributions of measured and MC were significantly differed especially in DIO data, and it was considered to be raised from a deviation between the calculated magnetic field and the actual one outside the magnetic poles of SBM. To reject the tracks passing through locations distant from the magnetic poles, restrictions based on the fitted positions on the dummy plane are implemented. Specifically, the fitted position on the dummy plane is restricted within the range of [-15.5 cm, 15.5 cm].
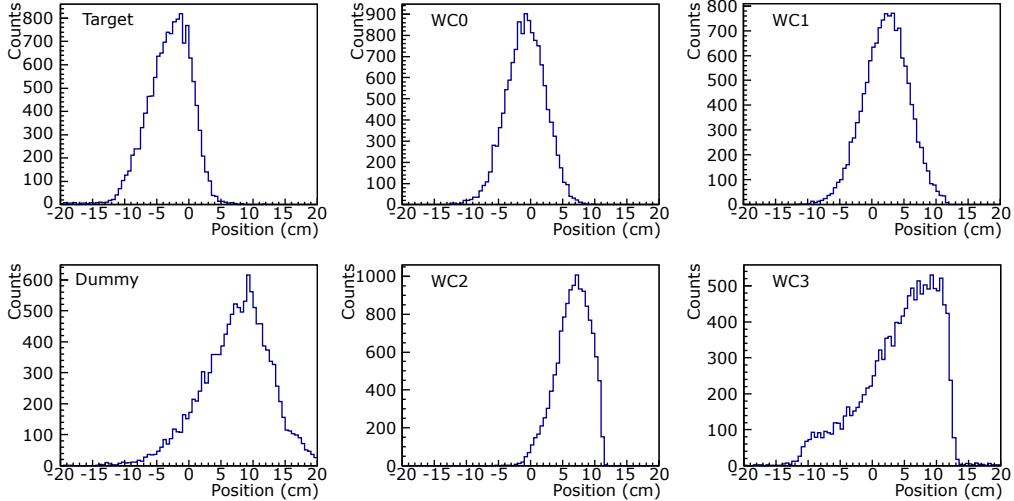
Figure 4.36: The fitted X-position on each plane.

4.4 Threshold optimization

The threshold values for hit finding were optimized by tagging analysis, which is performed by 3WC tracking, in order to be determined by independent way
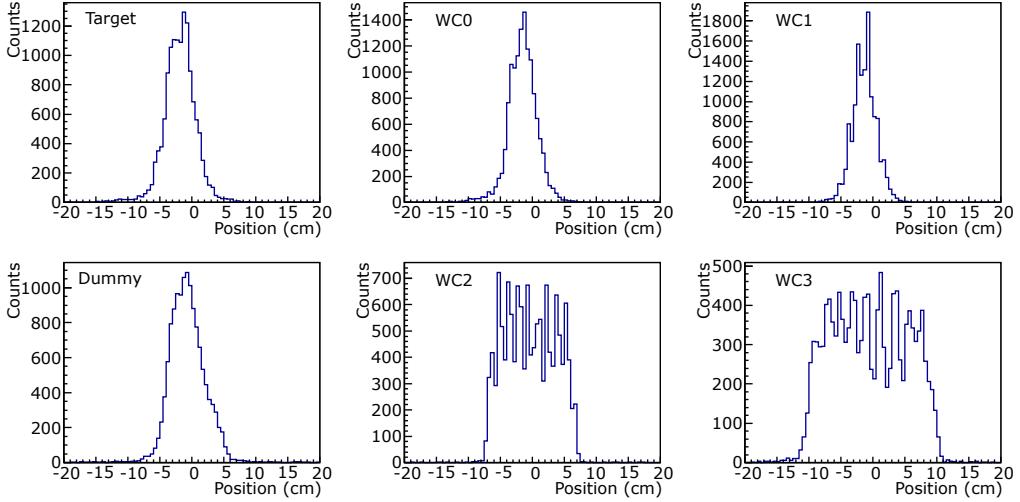
Figure 4.37: The fitted Y-position on each plane.

from the threshold itself. In tagging analysis, the extrapolated position is utilized as a center of search window in the $c_{i,j}$ map as Figure 4.38. The highest $c_{i,j}$ is searched from inside of the window, where window size is 20 sample points times five or two strips for X-plane or Y-plane respectively.

Figure 4.39 shows the histograms of the tagged $c_{i,j}$ to confirm validity of the threshold. The histograms with red line in that figure shows the pedestal. These pedestals are the maximum values searched from 6 μs $\pm$ 10 ns of all strips except the strips that have one or more hits in 6 μs $\pm$ 1 μs.

The threshold C_{thr} is also confirmed in the same way of the confirmation of c_{thr} as Figure 4.40. As a results, the thresholds for each MWPC is set as Table 4.1. The applied HV to MWPC-724 had been lower than MWPC-713, it is considered the reason of the different gas gain between WC0,1 and WC2,3.
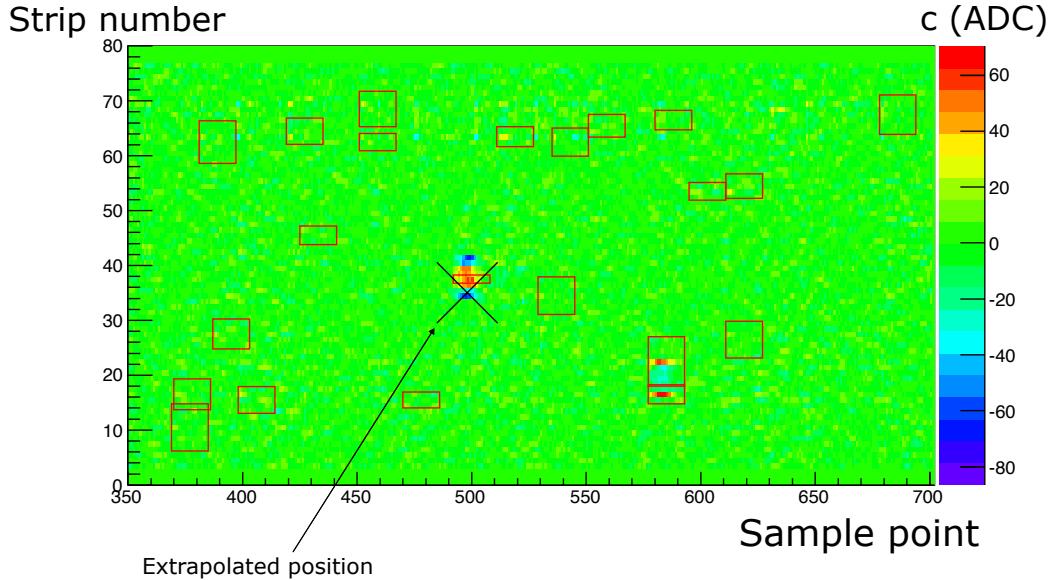
Figure 4.38: A typical event display of tagging analysis. The point shown by a cross is the position extrapolated from 3WC tracking to this plane and the boxes with red line are the reconstructed hits. The highest $c_{i,j}$ is searched around this point by the tagging analysis.
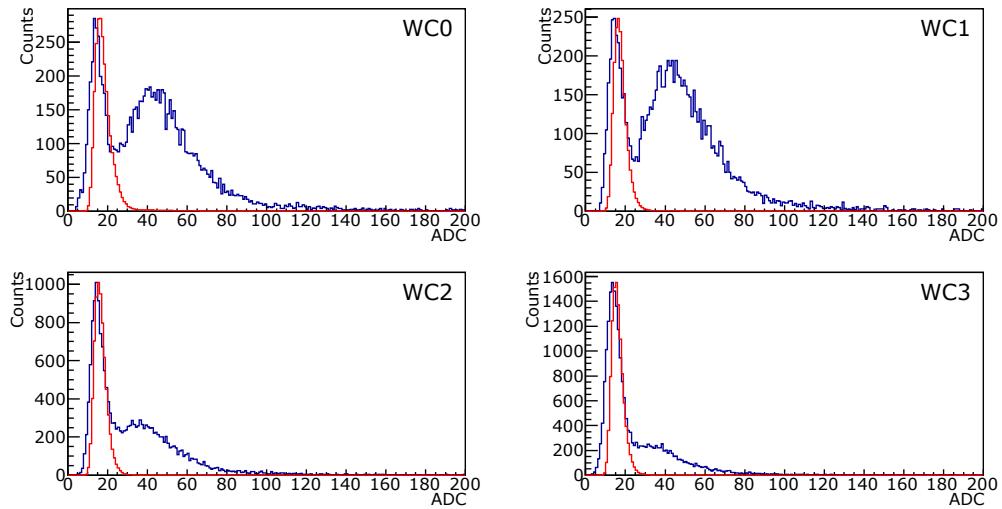
Figure 4.39: The threshold confirmation for c_{thr} of X-strip by tagging analysis. Blue line is the tagged hit and red is pedestal.
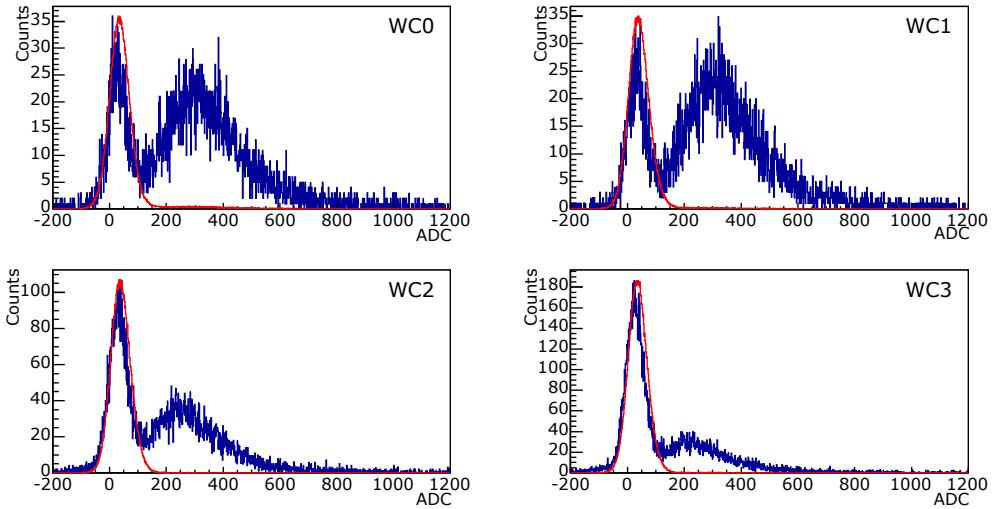
Figure 4.40: The threshold confirmation for C_{thr} of X-strip by tagging analysis. Blue line is tagged hit and red is pedestal.
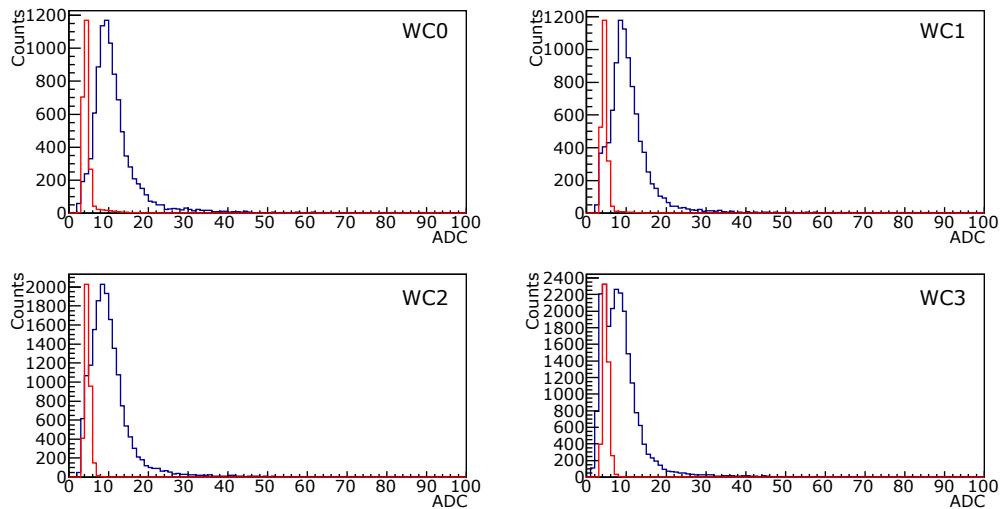
Figure 4.41: The threshold confirmation for c_{thr} of Y-strip by tagging analysis. Blue line is tagged hit and red is pedestal.
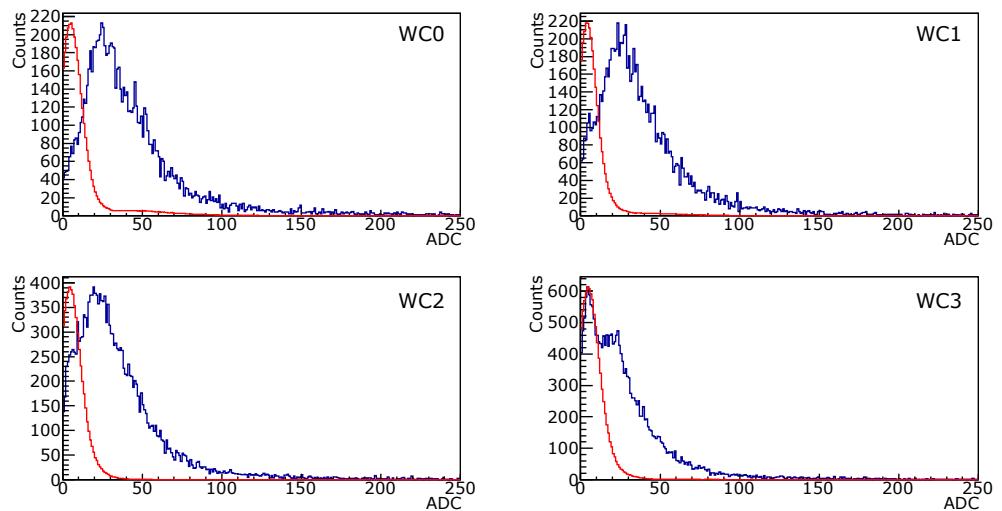
Figure 4.42: The threshold confirmation for C_{thr} of Y-strip by tagging analysis. Blue line is tagged hit and red is pedestal.

4.5　Tracking resolution

The resolution of WC0–3 is analyzed by 3WC tracking. The distribution of distance between an extrapolated position and the nearest hit to the extrapolated position is defined as a kind of resolution we named *tracking resolution*. Note that these resolutions are not the MWPCs' pure position resolution σ_x and σ_y. It is considered that multiple scattering by the air is dominant in the tracking resolution.

The dx and dy distributions are shown in Figure 4.43 and Figure 4.44 respectively. The tracking resolutions of each plane are evaluated by the central peak fitting with Gaussian distribution.

When σ_0 and σ_1 are the tracking resolution of WC0 and WC1 respectively, the tracking resolution for the target plane σ_{target} can be calculated geometrically by considering that the track fitted positions are shifted $\pm\sigma_0$ and $\mp\sigma_1$ from true hit positions as Figure 4.45. Note that this is a definition of the σ_{target} and this is not the variance of Gaussian distribution.

As a result, the tracking resolutions of each plane including the target is shown in Table 4.3. The tracking resolution at the target plane is used for the fiducial cut for the stopping muon distribution.

Table 4.3: The tracking resolution of each MWPC. Note that this value is not true position resolution of the MWPCs.

	σ_x	σ_y
target	24.7 mm	33.5 mm
WC0 (724)	6.3 mm	8.7 mm
WC1 (724)	5.3 mm	6.9 mm
WC2 (713)	7.2 mm	6.6 mm
WC3 (713)	10.0 mm	10.0 mm

4.6　Detection efficiency

The detection efficiency of the MWPCs is evaluated by tagging analysis. The detection efficiency is estimated as the ratio of the entry number in $|dx| < 3$ cm of dx histogram shown in Figure 4.43 to total track number.
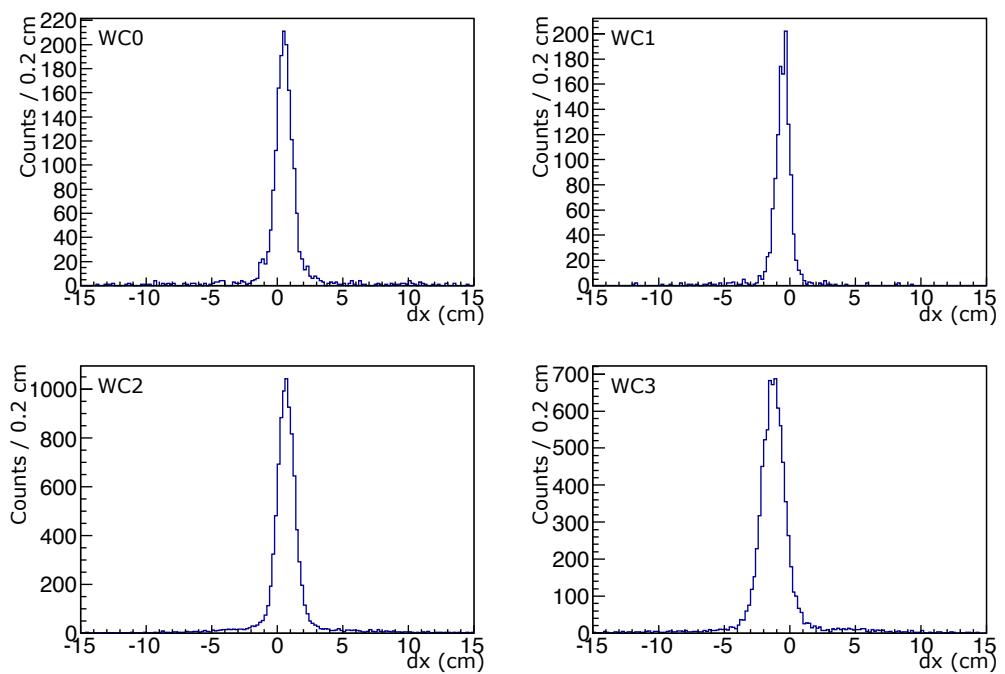
Figure 4.43: The distribution of the dx for each MWPC analyzed with 3-MWPC tracking method.
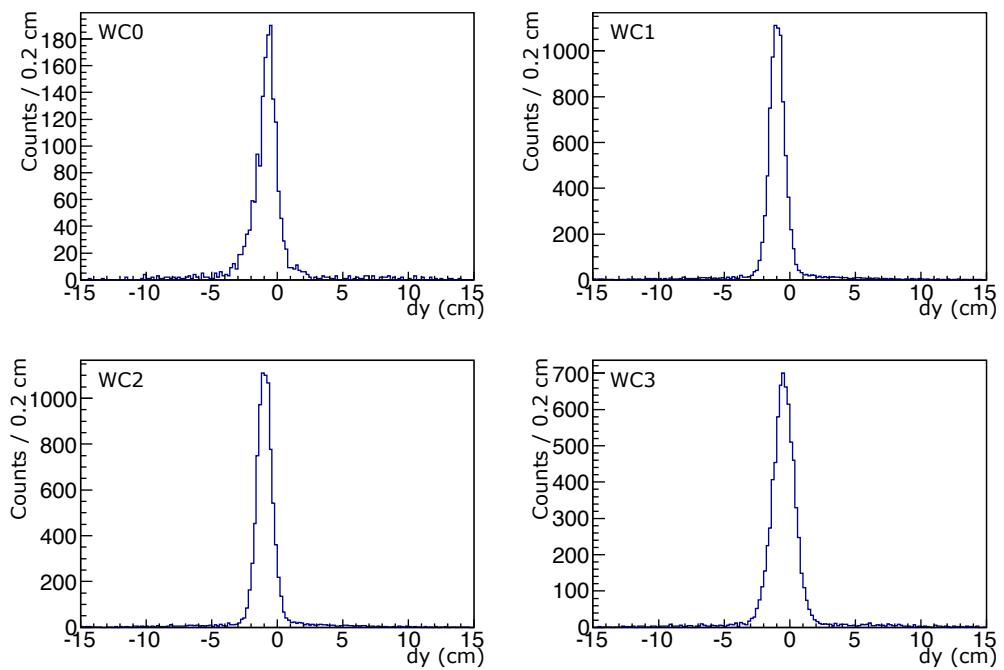
Figure 4.44: The distribution of the dy for each MWPC.
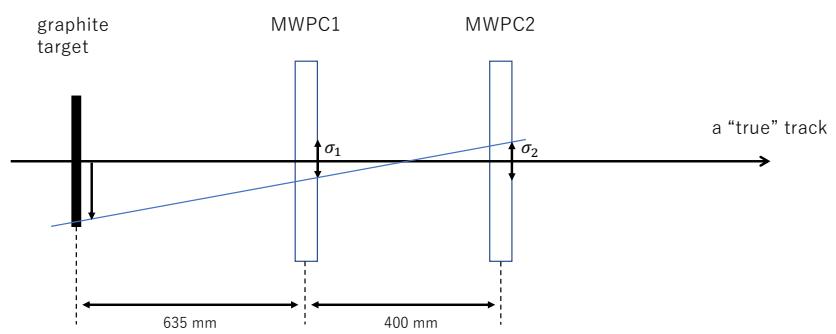
Figure 4.45: σ_{target} calculation.

The detection efficiency of each MWPC can be calculated as Table 4.4. As a result, total detection efficiency is 74 %.

Table 4.4: Detection efficiency

	hit	total tracks	Efficiency
WC0	4386	5479	92%
WC1	4498	6193	96%
WC2	4216	6880	92%
WC3	1836	2654	90%

Position Dependence

The X-hit positions correlate with the momentum, especially at downstream. If the detection efficiency has position dependence, the momentum spectrum as a result of tracking analysis is also distorted. In this experiment, the momentum spectra of measured data are compared with that of MC. Therefore, the position distribution of the detection efficiency should be consistent with that of MC.

The procedure to analyze the position dependence of the detection efficiency is generally the same as previous section. In addition, to calculate the efficiency on a strip, one more condition that the hit position is on the focused strip is required. In other word, each dx histogram are divided in 80 histograms according to the strip reconstructed by 3-MWPC tracking.

Figure 4.46 shows the efficiency distributions of WC0–3. The same distributions of MC simulation performed in the next section are overlaid in the figure. The flatness of each histograms are consistent to MC simulation including the error bar. In addition, the behavior of distributions are consistent with MC, especially at both end in WC0–1 because the tracks which can be correctly reconstructed hardly pass the side of upstream detectors. The assurance of the flatness of efficiency is given in the same way for the H-line experiment in future.
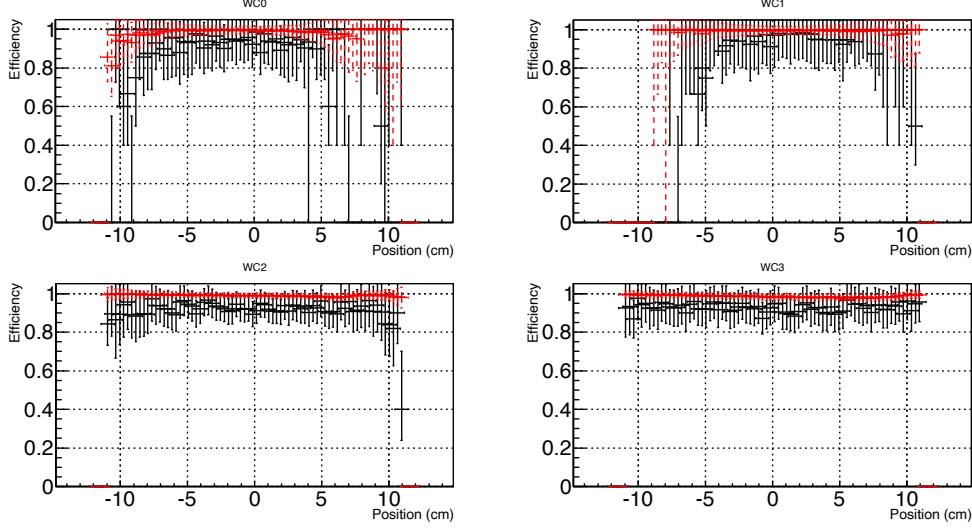
Figure 4.46: The distributions of position dependence of the detection efficiency for WC0–3, where black and red points show data and MC respectively.

4.7 Momentum calibration

The momentum calibration is done By using Edge data. The Michel edge 52.8 MeV/c is used for calibration. The complementary error function (erfc) defined as

$$\text{erfc}(x) = \int_x^{+\infty} \frac{1}{\sqrt{2\pi\sigma^2}} e^{-(x'-\mu)^2/2\sigma^2} dx', \tag{4.16}$$

where μ is median and σ is variance, is fitted to the measured edge. Fitting function is

$$f(x) = n \times \text{erfc}(x), \tag{4.17}$$

where fitting parameters are n, μ, and σ, and the fitting region is [51 MeV/c, 60 MeV/c]. In this step, the value of μ is adjusted to the Michel edge by modifying the scaling factor of the magnetic field map r_{Edge} in the track fitting step. Note that the magnetic field can be linearly scaled as mentioned in Section 3.2.3.

The result of fitting to Michel edge measurement data is shown in Figure 4.47. As a result, the fitted parameters of the error function are determined as $n = 34.8 \pm 1.4$, $\mu = (5.27 \pm 0.006) \times 10^{-2}$ GeV/c, and $\sigma =$

100

$(6.15\pm0.80)\times10^{-4}$ GeV/c. The scaling factor is determined to $r_{\text{Edge}} = 1.041$. The momentum distribution of Figure 4.47 will be compared with that of MC generated data as will be mentioned in Section 5.3. The energy deposit of emitted electron in the muon stopping target is included in the MC simulation so that the correction of the energy deposit is performed in the comparison between the measured and MC generated data.

Once r_{Edge} defined, the other factors for Body and DIO data are determined by r_{Edge} and the typical B strength shown in Table 3.6 as below;

$$r_{\text{Body}} = r_{\text{Edge}} \times \frac{B_{\text{Body}}}{B_{\text{Edge}}} = 0.892, \tag{4.18}$$

$$r_{\text{DIO}} = r_{\text{Edge}} \times \frac{B_{\text{DIO}}}{B_{\text{Edge}}} = -1.090. \tag{4.19}$$

The momentum spectrum of Body data is utilized for confirmation of momentum acceptance of the spectrometer in this measurement and MC simulation so that the comparison between measurement and MC generated data will be discussed in Section 5.4.
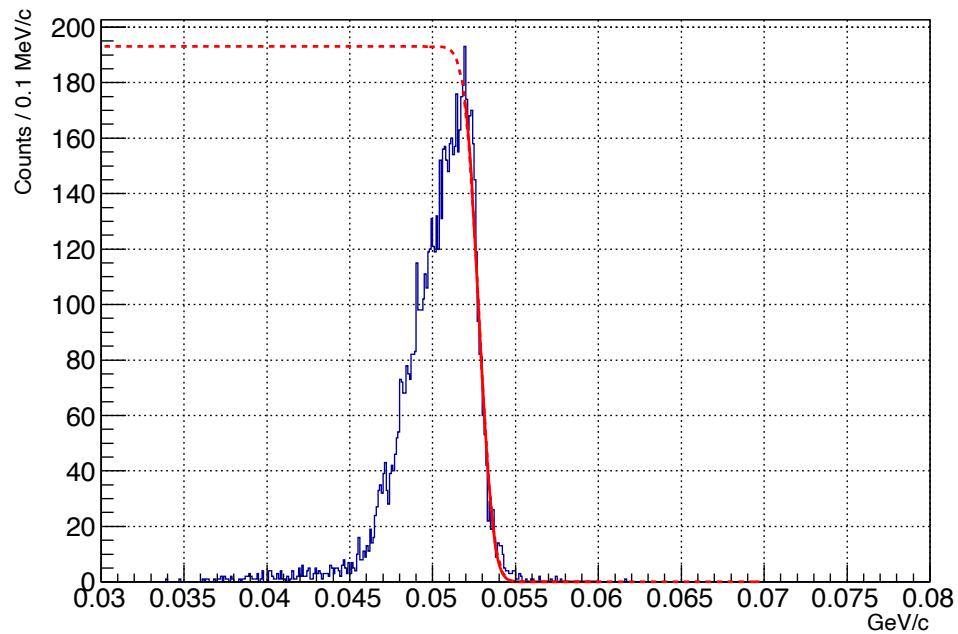
Figure 4.47: Momentum distribution of the Michel edge measurement data. The red line shows the fitted error function.

Chapter 5

Monte-Carlo simulation

The DIO spectrum around the endpoint $E_{\mu e}$ is important to evaluate the total number of the muonic atoms formed in the production target for the step of μ-e conversion measurement. In DeeMe experiment, the DIO yield and spectrum detected by the spectrometer are compared with the theoretical curve by using Monte-Carlo simulations (MC). To demonstrate it, the MC simulation generation and comparison with the measured data are performed in this chapter.

5.1 Monte-Carlo simulation

In order to compare DIO spectrum with theoretical model, MC simulations were carried out by G4beamline [39].

G4beamline is a single-particle simulation program based on the Geant4 and it is optimized for beam line simulation. The physics process is implemented in G4beamline from Geant4 such as Coulomb scattering, Bremsstrahlung, and ionization in order to reproduce the effect of multiple scattering to emitted electron.

5.1.1 Geometry

The simulation setup is shown in Figure 5.1. G4beamline coordinate system is Cartesian and right handed. Z axis is along beam direction, X is horizontal and orthogonal to Z axis, and Y is vertical direction in this simulation.

Included elements are the stopping target, the WC0-3, and the SBM,

where the WC0-3 are reproduced as the composite elements of field and potential wires, wire frame, and chamber body. The other space is filled with the air in this simulation. Note that it will be replaced by the helium gas in H-Line simulation.

In order to understand the acceptance of spectrometer, the model of SBM was constructed as detailed as possible including its field clamp. The magnetic field map calculated with Opera-3D was used for the field of SBM and the map was scaled for each momentum setting. The scale factor was determined by the momentum of Michel edge as described in Section 5.3.

In G4beamline, The initial particles are defined by a "gun file" which contains information of initial particles such as start position (x, y, z), 3-momentum (p_x, p_y, p_z), and particle ID. The initial particles of this simulation were the decay electrons from the muonic atom in the target. The distribution of muon stop position in X, Y, and Z coordinate was assumed Gaussian with $(\mu_x, \mu_y, \mu_z, \sigma_x, \sigma_y, \sigma_z) = (0 \text{ mm}, 0 \text{ mm}, 0 \text{ mm}, 24.7 \text{ mm}, 17.5 \text{ mm}, 0.07 \text{ mm})$. Note that the target was set 45° angle to the beam axis, the X distribution expands and the thickness of the target contracts by a factor of $\sqrt{2}$.

In H-Line simulation, gun files will be also utilized but the initial beam will be generated from another simulation through beamline.

5.2 Comparison between measured and MC data

In order to evaluate consistency of the MC simulation, these MC data were compared with measured data.

5.2.1 Position residual and pull function

The residual and pull distributions of MC simulation have been already shown in Section 4.3.1. The residual and pull-function distributions are also drifted to left and right alternately in both MC and measured data. It is observed in both measured and MC generated data commonly so that it is considered not to be any flows related to the detector response.
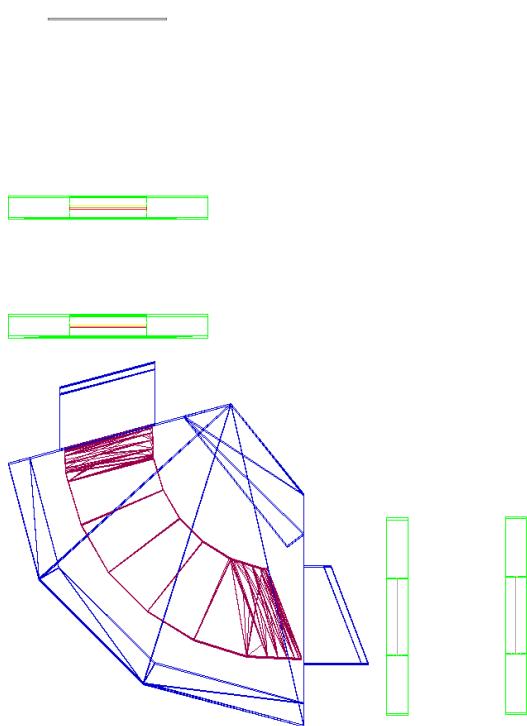
Figure 5.1: G4beamline eventdisplay

5.2.2　P-value

The p-value of MC data is shown in Figure 5.2. The $p < 0.1$ region is cut from the following all MC data.
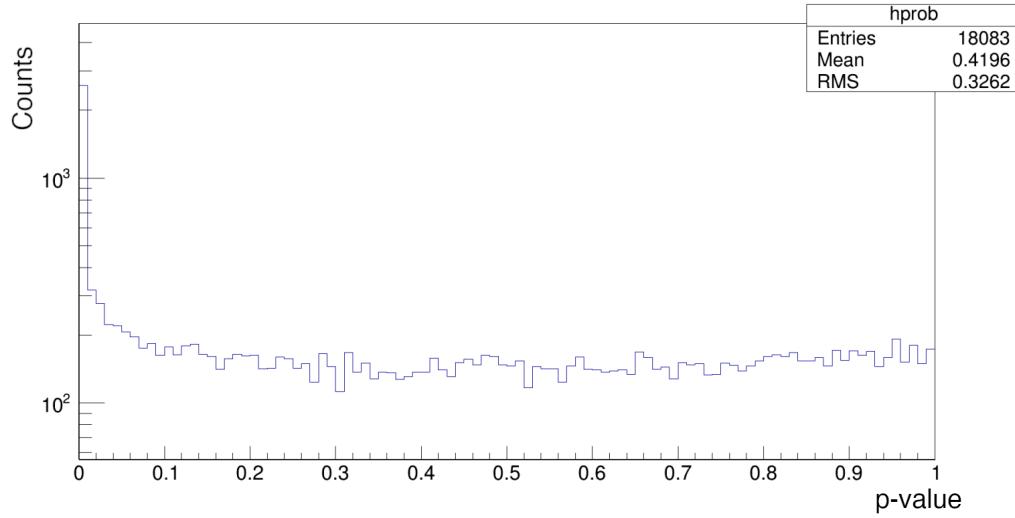
Figure 5.2: The p-value histogram of the Body data of MC.

5.2.3　Fitted position distribution

The fitted position distributions on each plane including dummy and target are shown in Figure 5.3.

5.3　Momentum calibration

In Section 4.7, the scale factors of the magnetic field of SBM had been determined for the track fitting analysis. Then the optimization of the scale factors for the G4Beamline MC simulation is described in this section.

The momentum calibration for MC simulation is performed to find the scale factor on G4Beamline simulation that best matches the Michel edge of the measured data while keeping the scale factors for the track fitting fixed to the value determined in Section 4.7. If there is a discrepancy in the energy loss in the target between the MC simulation and the measurements, the value of the Michel edge varies in each momentum spectrum. Therefore, an
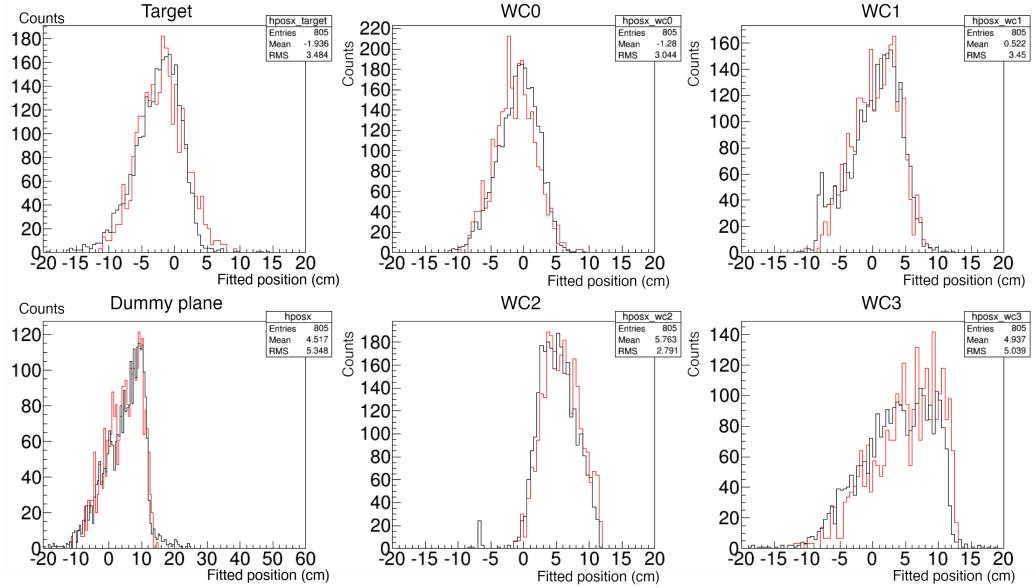
Figure 5.3: The distribution of fitted position on each plane (Black: measured data, Red: MC data).

evaluation of the energy loss in the target is necessary to be exact. However, with the above-mentioned method, calibration can be performed, including uncertainties between the experiment and simulation.

Figure 5.4 shows the momentum spectrum of MC simulation of Edge mode. The scaling factor $f_{\mathrm{MC}}^{\mathrm{edge}}$ had been roughly determined by the error function, then it was optimized by scaling the MC spectrum to minimize the χ^2 with the data. The Edge momentum spectrum of MC simulation was scaled up and down little by little and the χ^2 was calculated from the data spectrum and each scaled MC spectrum to find a scale factor minimizing the χ^2. The obtained χ^2 distribution is fitted by a quadratic function. As a result, the best scale factor and the calibration accuracy was evaluated to -1.0097 ± 0.0007 and the systematic error from the scaling is equivalent to $\sigma = 0.04 \text{ MeV}/c$.

The scaling factors f_{MC}^{Body} and f_{MC}^{DIO} for Body and DIO data sets respectively are scaled with the magnitude of B field measured in the experiment as already mentioned in section 3.3 and Table 3.6. They are calculated as

107

below;

$$f_{\rm MC}^{\rm edge} \quad = \quad -1.0097, \tag{5.1}$$

$$f_{\rm MC}^{\rm body} \quad = \quad f_{\rm MC}^{\rm edge} \times \frac{B^{\rm body}}{B^{\rm edge}} = -0.865, \tag{5.2}$$

$$f_{\rm MC}^{\rm DIO} \quad = \quad f_{\rm MC}^{\rm edge} \times \frac{B^{\rm DIO}}{B^{\rm edge}} = +1.057. \tag{5.3}$$
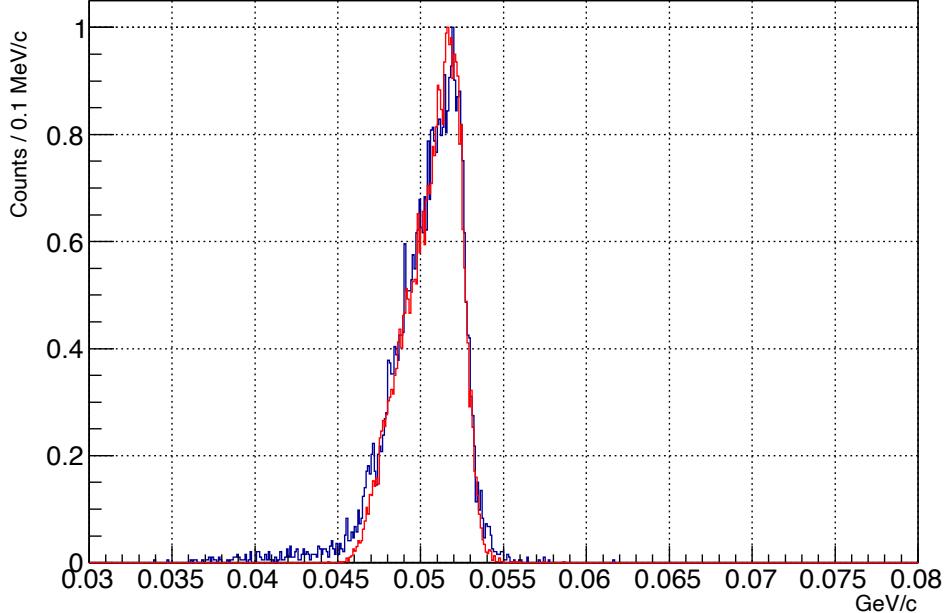
Figure 5.4: The momentum spectra of data (blue) and MC (red) with the 52.5 MeV/c setup.

5.4 The momentum spectrum of the Body data

The body data were taken for the purpose of evaluating the consistency of momentum acceptance between the measurement and MC simulation. The momentum spectra of the Body data are shown in Figure 5.5, where the MC

histogram is scaled by minimizing χ^2 with respect to the measured data. The ratio R of the MC spectrum to the measured spectrum is shown in Figure 5.6. They agree within the region 40 MeV/c – 50 MeV/c, considering the statistical error. It should be noted that the range of 40-42 MeV has large statistical errors. However, it is not inconsistent to consider the distribution as constant so that the MC acceptance distribution is adopted in this analysis. The reliable acceptance regions corresponding to 40 MeV/c – 50 MeV/c for Body dataset are 47 MeV/c – 58 MeV/c for Edge and 49 MeV/c – 61 MeV/c for DIO.
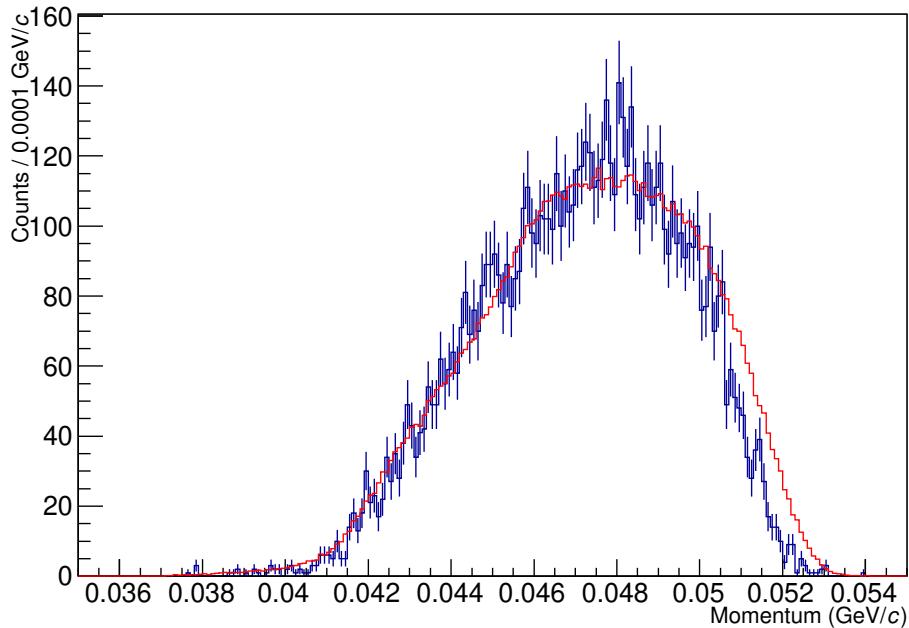
Figure 5.5: The momentum spectra of Body dataset (blue: measurement, red: MC simulation).
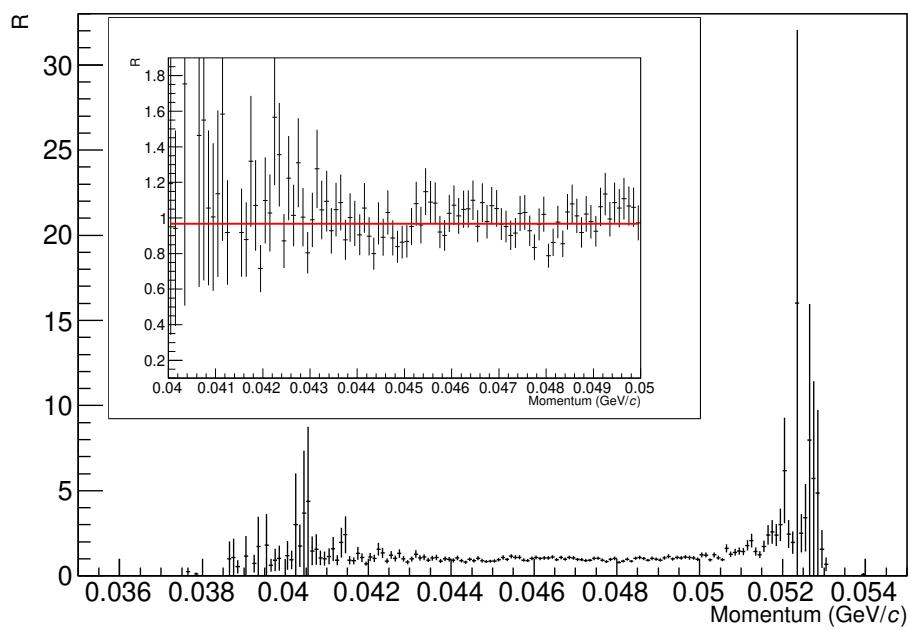
Figure 5.6: The ratio R distribution. The frame shown in top left is a zoom view in the range of 40 MeV/c – 50 MeV/c and the red line is a constant value (0.97).

5.5   DIO momentum analysis

The reliable momentum region for DIO dataset was determined to 49 MeV/c – 61 MeV/c in Section 5.4. The momentum spectra of DIO dataset from measurement and MC simulation are compared in this region.

The method of MC simulation and analysis for the DIO measurement is almost the same as Edge and Body analysis except the momentum distribution of the initial electrons and the scaling factor of the magnetic field. The Czarnecki spectrum of carbon atom was adopted in the gunfile as Figure 5.7. After G4Beamline event generation, the trackfitting was done with the same configuration of the measured DIO data analysis. Note that an additional cut condition should be introduced into the hit position at dummy plane so that it is mentioned first of all.
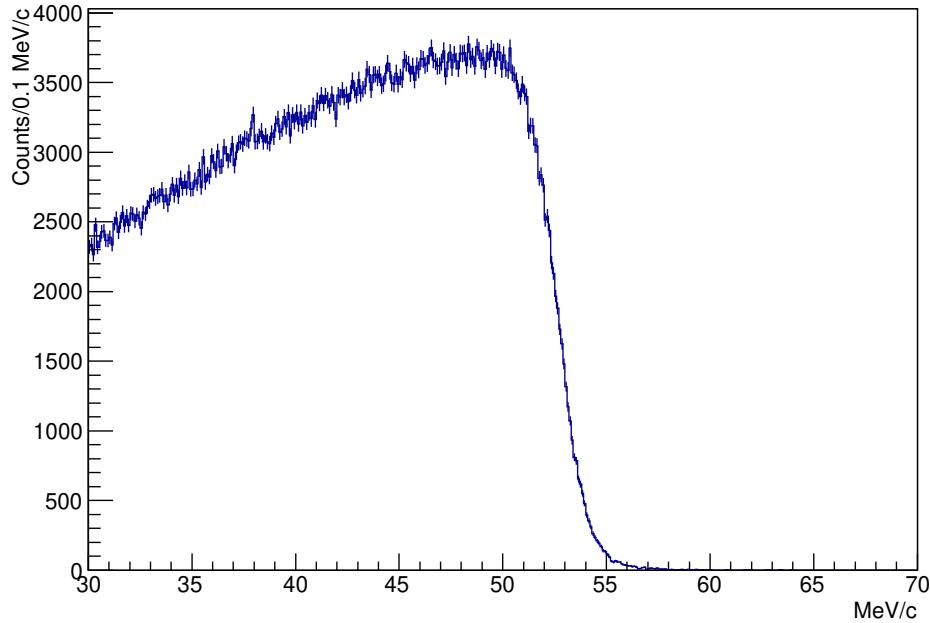
Figure 5.7: The momentum distribution of initial electron in the gunfiles.

5.5.1 Track cut

As already mentioned in Section 4.3.4, the deviation between measured and MC data had been observed at low momentum tail in the DIO momentum spectra without the fitted position cut in the dummy plane as shown in Figure 5.8. The main component tracks of the tail were found as the tracks out of the magnet pole, within the inner side of the rotating arc, as shown in Figure 5.9. The region on the magnet pole is -15 cm $\leq x \leq 15$ cm on the dummy plane so that the cut condition of $x <15$ cm on the dummy plane is expected to suppress the tail. In addition, the resolution of the fitted position on the dummy plane should be taken into account to determine the cut condition. Figure 5.10 shows histograms of DIO momentum distributions with several cut conditions in the dummy plane. The distribution of measured data remains stable but the low momentum tail of MC histograms decreases according to the cut range. Therefore, several DIO momentum spectra with slightly different cut conditions were prepared and compared with the measured data to select a condition giving minimum χ^2 as shown in Figure 5.11. As a result, the allowed region on the dummy plane was set to [-15.5 cm, 15.5 cm]. The momentum spectra analyzed with the definitive cut condition on the dummy plane is shown in Figure 5.12.

5.5.2 Momentum acceptance estimation

The momentum acceptance for DIO was estimated by the MC simulation. Using the same setup of G4beamline, the events were generated with the special gunfile in which the beam energy distributed from 40 MeV to 110 MeV uniformly. The distribution of the other parameters in the gunfile (x, y, z, p_x, p_y, and p_z) are the same as that for DIO simulation. The MC simulation was generated with using this gunfile and the other process was the same as μ^- 55 MeV MC simulation. The momentum acceptance spectrum of this MC simulation is shown in Figure 5.13.

The uncertainty of the momentum acceptance should be confirmed with the Michel body measurement. The systematic error derived from the uncertainty between the measured and MC data will be discussed in the next section.
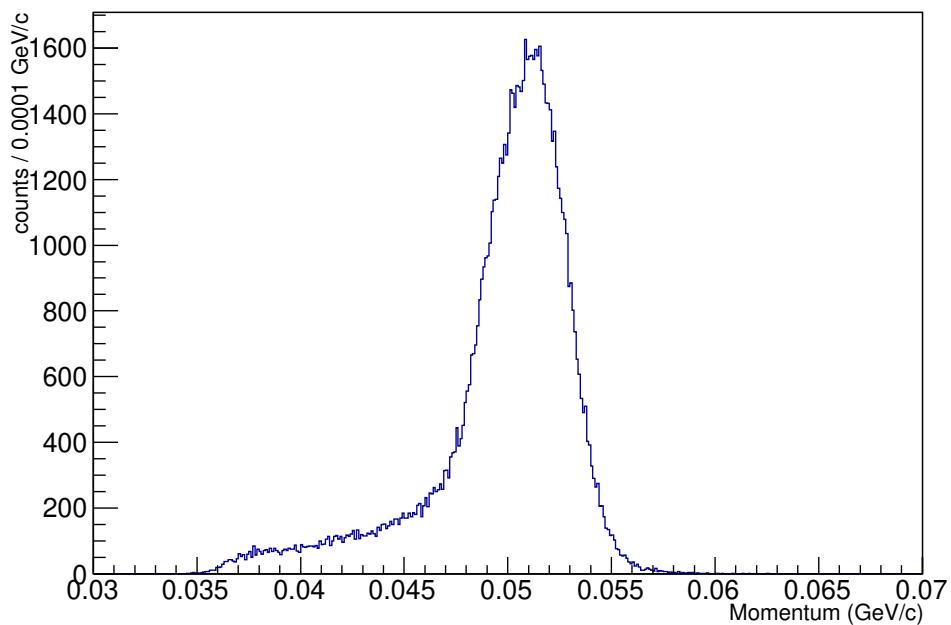
Figure 5.8: The momentum spectrum produced by MC simulations for DIO data without the fitted position cut in the dummy plane.
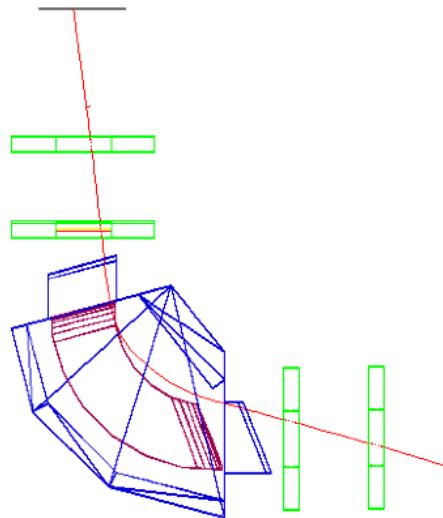
Figure 5.9: A typical track of G4Beamline simulation giving a low momentum entry.
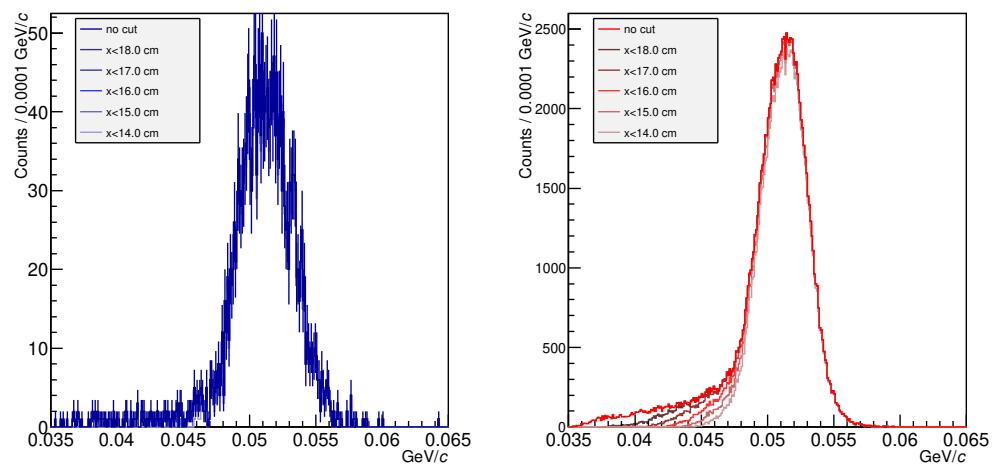
Figure 5.10: Several DIO momentum spectra with different cut conditions. These for the measured data are shown at left and these for MC are shown at right.
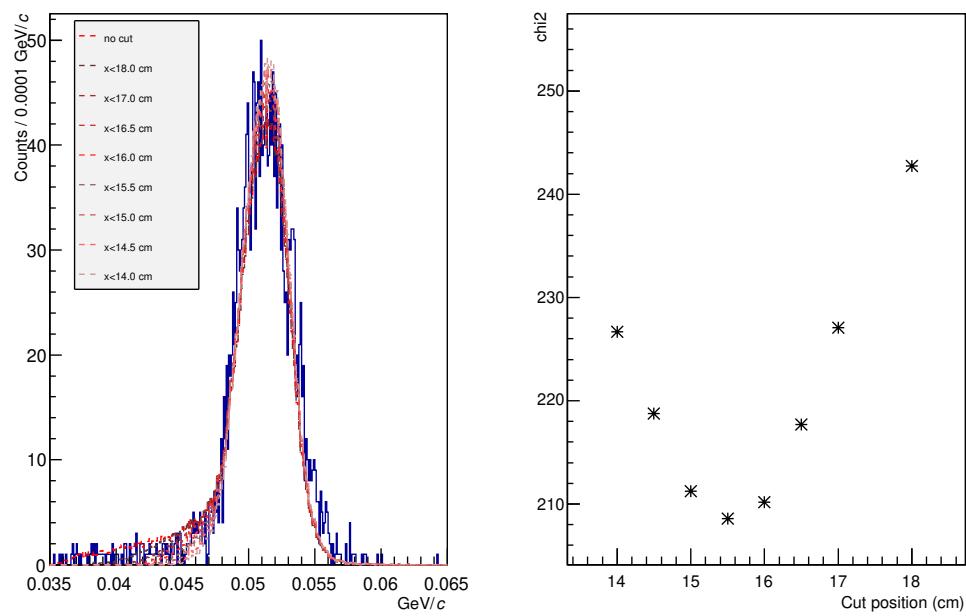
Figure 5.11: The DIO momentum spectra for MC with different cut conditions (dotted line) are shown at left, where these MC spectra are scaled to minimize the χ^2 compared to the measured histogram (blue solid line). The graph on the right shows the distribution of χ^2 with different cut conditions.
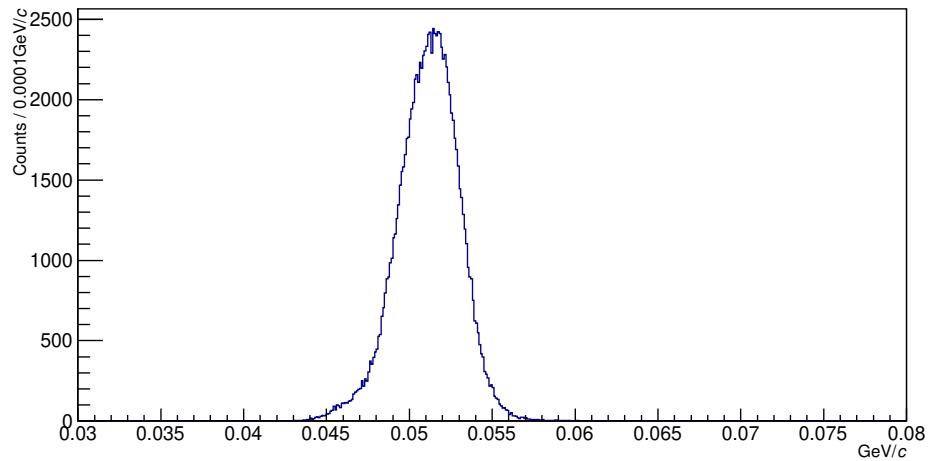
Figure 5.12: The DIO momentum spectrum of MC simulation with the definitive cut condition on the dummy plane.
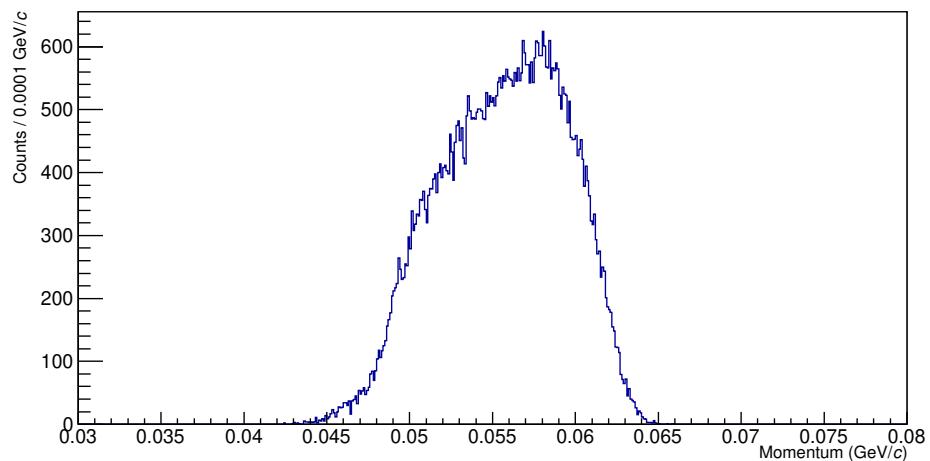
Figure 5.13: The momentum acceptance spectrum generated from G4Beamline simulation.

5.5.3 DIO data analysis

The acceptance, observed, and MC generated momentum distributions are shown in Figure 5.14, where the MC spectrum is fitted to the measured one by minimizing the χ^2 in the region 50-60 MeV/c. The DIO-MC spectrum and the measured DIO spectrum are not inconsistent with p-value of 0.83. Additionally, the acceptance distribution is generally consistent with the expected momentum range.
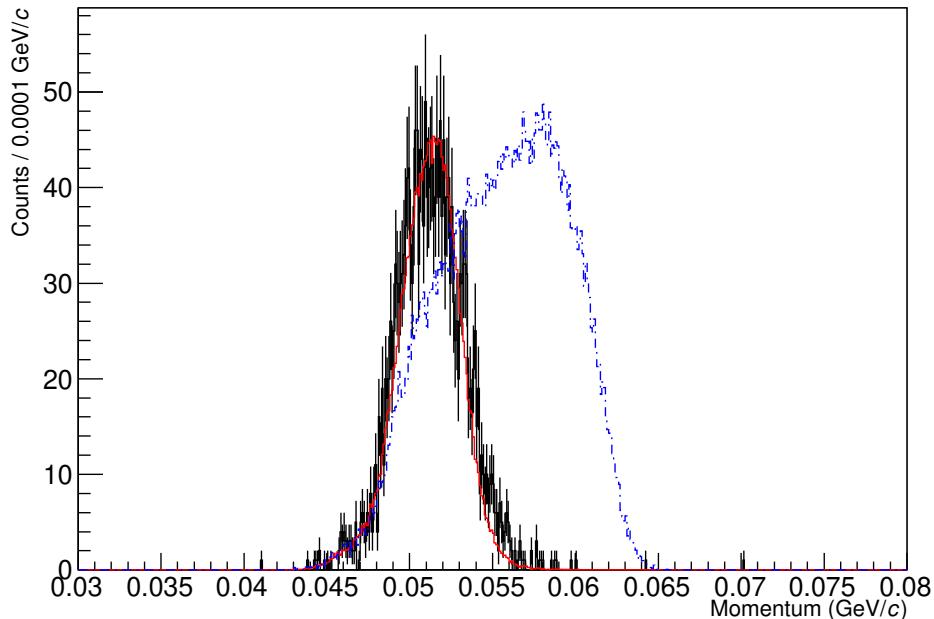
Figure 5.14: The reconstructed momentum spectrum of DIO-Mode. The black solid line with error bar shows the measured spectrum in this performance test. The red line shows the MC-generated spectrum. The blue dash-dotted line shows the MC-generated acceptance curve.

Chapter 6

Systematic Errors

In the Chapter 4 and 5, only the statistical error was considered for DIO spectrum. In the following sections, the systematic errors will be discussed.

6.1 Magnetic Field inconsistency

As mentioned in the Section 3.2.3, the magnetic field map of the SBM included in the MC simulation and tracking analysis was generated by OPERA-3D. The consistency between the calculated field map and real one should be confirmed and the systematic error from its inconsistency should be evaluated.

The measured momentum spectrum is calibrated by fitting of the Michel edge to generated spectrum in MC simulation so that the momentum gap between data and MC is expected to be adjusted. Whereas the momentum spectrum is considered to be distorted if the momentum deviation has dependence on the momentum. In other word, to evaluate the momentum spectrum distortion from the fringe field, the momentum dependence uniformity should be confirmed.

6.1.1 Magnetic Field measurement

The magnetic field scan was performed by using a 3-axis NMR probe (Lake Shore Model 460) fixed on a scanning robot.

The pole shape of the PACMAN is simple rectangular so that it is very easy to scan fill region, but On the other hand, that of the SBM is bent 90

degree and covered by the return yoke except the entrance and exit apertures. Therefore, the scanning full region along with its yoke was difficult for the utilized measurement instruments. It is considered that the main source of the inconsistency of momentum analysis is from the fringing field at upstream and downstream apertures. Thus, we focused on this fringing field to evaluate inconsistency of the calculated field map in this magnetic field measurement.

The measurement region and the measured points in the orthogonal plane to Z-axis are shown in Figure 6.1. The measurement was performed sequentially along the Z-axis as below;

1. $\boldsymbol{B}$ was measured along Z-axis with fixing the coordinate (x, y).

2. After once linear measurement finished, the position in X-Y plane was moved to the next point.

3. The processes 1 and 2 were iterated for every 50 mm in $-150 \leq x \leq 150$ mm and $y = 0, 30, 50$ mm plane,

4. where the points in the region $y < 0$ were not measured because it is considered that B_y distribution is symmetric respect to $y = 0$ plane.

5. After upstream iteration was finished, the instrument was moved to downstream.

The measured points are shown in Figure 6.1. The results in the measurement planes $y = 30$ mm and $y = 50$ mm were substituted for $y = -30$ mm and $y = -50$ mm planes. The rotation angle of the probe around Z-axis was set to maximize B_y on the magnet yoke. The magnetic field strength at a point is measured 15 times and these average value were taken.

In this section, the field map based on only the OPERA calculation is defined as $\boldsymbol{B}$ and the map modified by the field scan data is defined as $\boldsymbol{B'}$, where $\boldsymbol{B'}$ is basically the same as $\boldsymbol{B}$ but points in the region shown in Figure 6.1 are replaced by the measured field. Figure 6.2 shows the typical $\boldsymbol{B'}$, $\boldsymbol{B}$, and these residual along Z-axis at $(x, y) = (0, 0)$. Note that the field points in $\boldsymbol{B'}$ are linearly interpolated from the measured points.

6.1.2 Evaluation of momentum spectrum distortion from fringe field

To estimate the effect from the difference between $\boldsymbol{B}$ and $\boldsymbol{B'}$, two types of MC simulation was performed by using $\boldsymbol{B}$ and $\boldsymbol{B'}$. The setups of these two
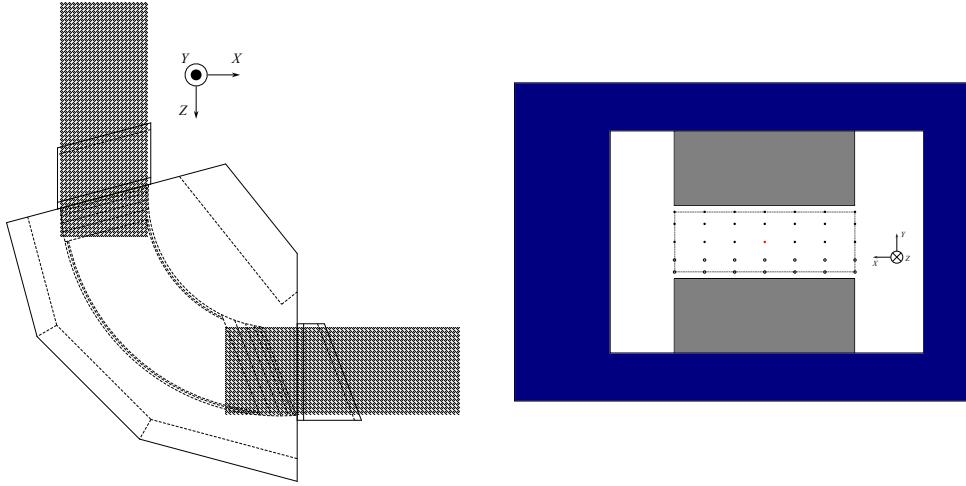
Figure 6.1: The measured region in Z-X plane (left) and X-Y plane (right). In the right figure, blue and gray regions show the return yoke and magnet pole respectively. The dots in the broken line show the measurement points. The central red dot is the point $(x, y) = (0, 0)$. The circles under $y = 0$ plane show the points mirrored from $y = 30, 50$ planes.

simulations were also the same except the field map at the SBM.

In order to evaluate the difference of momentum acceptance between two field maps, 11 ideal gunfiles which contained particular momentum electron beam of every 1 MeV/c from 50 MeV/c to 60 MeV/c was prepared as shown in Figure 6.3. Two types of systematic errors are considered as follows; 1) occurred from the difference between reconstructed and initial momentum, 2) occurred from the momentum dependence of the tracking efficiency by changing the field map in the MC simulation.

For the case 1, if the momentum calibration and tracking reconstruction work ideally, the relation between reconstructed momentum p_{reco} and initial momentum p_{init} is expected to be $p_{\text{reco}} = p_{\text{init}}$. However, it can be practically modified to a linear function as $p_{\text{reco}} = ap_{\text{init}} + b$. In this experiment, the parallel transition b is negligible because of the momentum calibration by the Michel edge. On the other hand, when the factor a does not equal to 1, the reconstructed momentum spectrum is distorted depending on the momentum as if the bin width changes according to a. In this analysis, which compares the measured and simulated momentum spectrum, the difference of a between measurement and simulation is important rather than a itself.
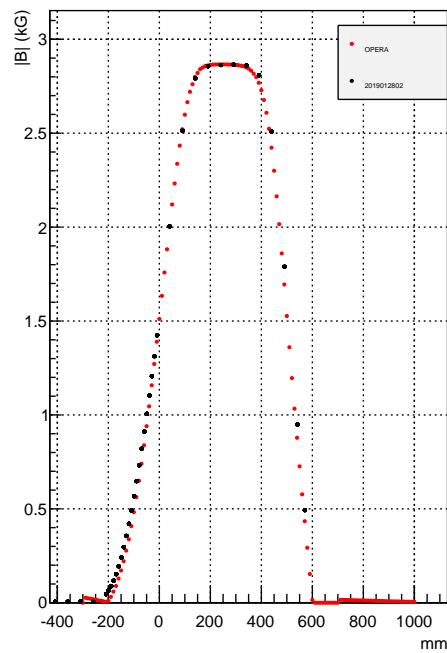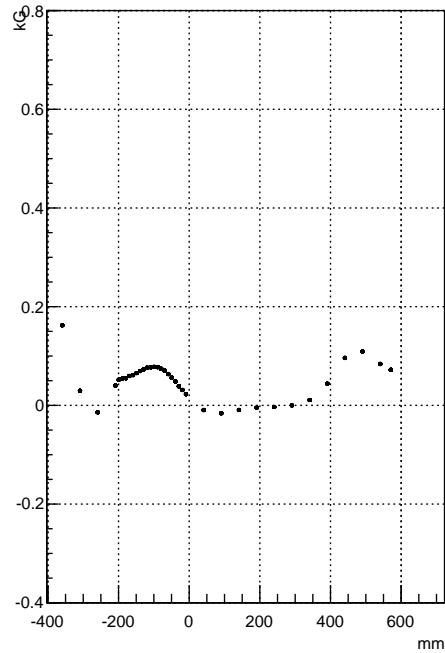
Figure 6.2: The left figure shows the magnetic field distribution of $\boldsymbol{B}$ (red dots) and $\boldsymbol{B'}$ (black dots) along Z-axis at $(x,y) = (0,0)$ pointed by a red dot in Figure 6.1). The right one shows these residual.

The initial momentum p_{init} is the same in both simulations but the factor a and reconstructed momentum p_{reco} are not, so that a and p_{reco} are used for the simulation with $\boldsymbol{B}$ and a' and p'_{reco} for $\boldsymbol{B'}$. The difference Δp_{reco} is considered as

$$\Delta p_{\text{reco}} = p'_{\text{reco}} - p_{\text{reco}} = (a' - a)p_{\text{init}}. \tag{6.1}$$

For the case 2, ratio of the number of reconstructed events to that of initial events indicates the momentum acceptance distribution. The difference between two acceptance distributions of the MC simulations with $\boldsymbol{B}$ and $\boldsymbol{B'}$ produces another systematic error. When the acceptance distributions are approximated as any function $A(p)$ and $A'(p')$ for the MC simulations with $\boldsymbol{B}$ and $\boldsymbol{B'}$ respectively, the ratio $A'(p)/A(p)$ is ideally constant.

These MC simulations were analyzed by the same way as Chapter 5. The results of 11×2 times MC simulations are shown in Figure 6.4.

In the case 1, the obtained mean values of momentum spectra as results of the tracking analysis were compared with the initial momenta given in the G4BL simulations as shown in Figure 6.5. The systematic error occurred from $a' - a$ is evaluated to be 1 %.

In order to estimate the case 2, the acceptance curves are fitted by Gaussian[1] as shown in Figure 6.6. The ratio of these functions is shown in the bottom of Figure 6.6 with red line.

In all cases, the systematic errors are comparable to the statistical errors. The way to evaluate the systematic errors shown here should be applied to the main experiment thus this type of systematics can be well undercontrol.

---

[1]There is no reason of Gaussian based on physics. It is adopted because Gaussian seems to be fit the histograms.
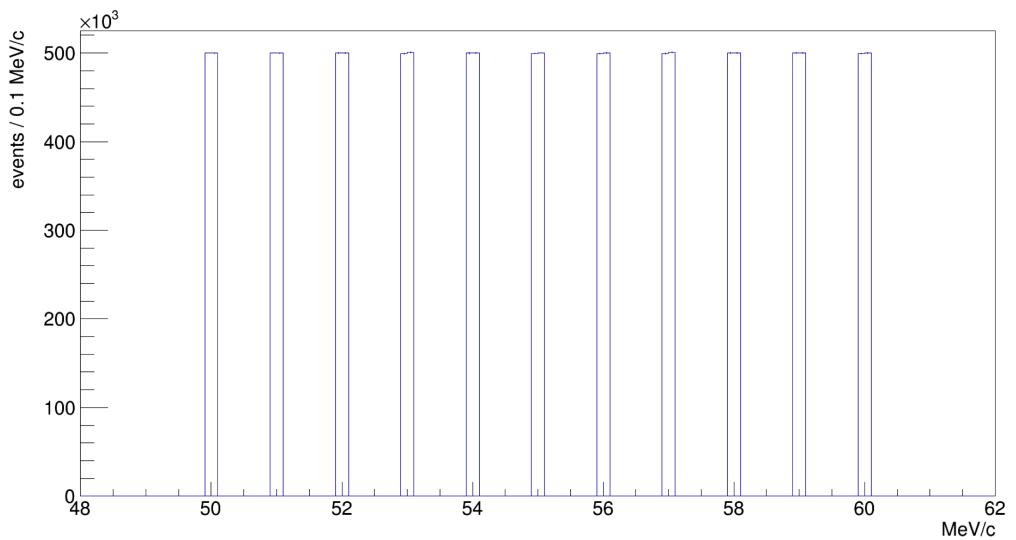
Figure 6.3: The momentum distribution of initial electrons in the magnetic field inconsistency simulation.
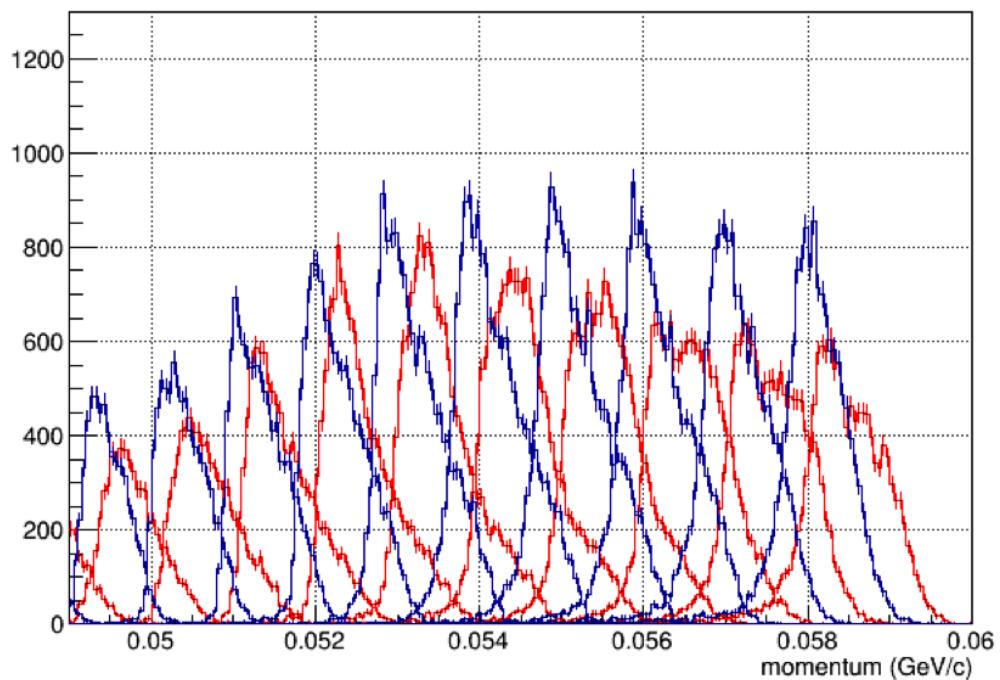
Figure 6.4: The reconstructed momentum distributions produced by the MC simulation and track reconstruction. The blue histograms are produced by the MC with $\boldsymbol{B}$, and the red lines are with $\boldsymbol{B'}$.
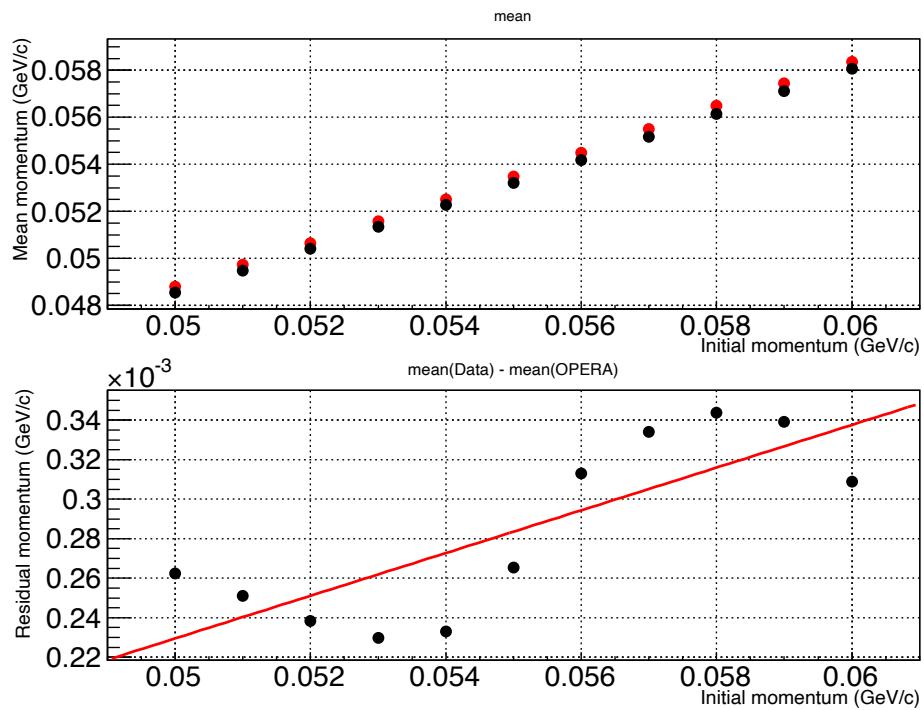
Figure 6.5: (Top) the mean values of each monochromatic momentum distribution in Figure 6.4, where horizontal axis shows the initial momentum in the G4BL MC simulation. (Bottom) the residual between the mean values of B and B'.
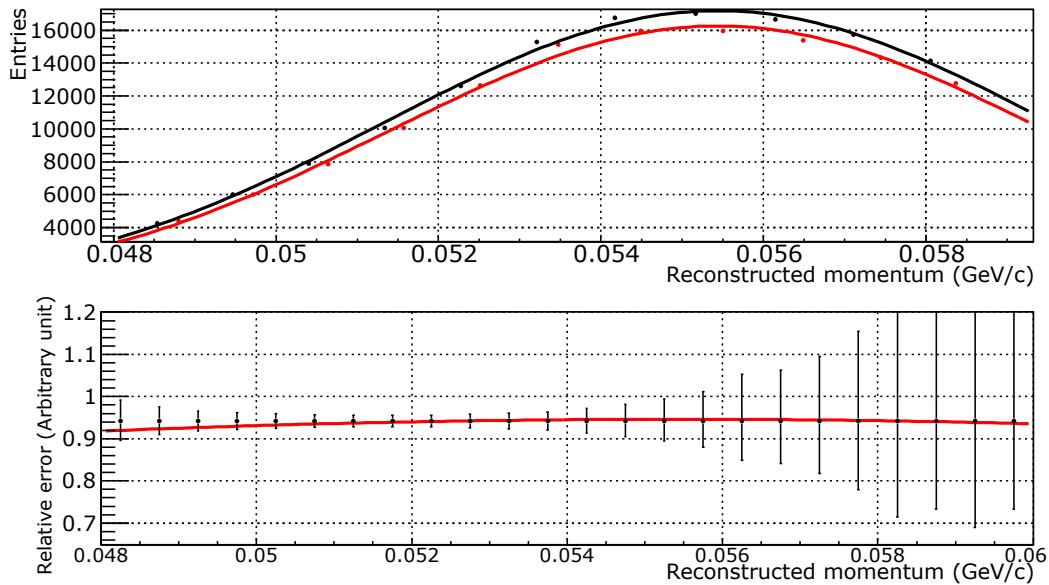
Figure 6.6: (Top) the number of entries of each monochromatic momentum distribution in Figure 6.4, where horizontal axis shows the mean momentum of each distribution. The red and black dots show the result with B and B' respectively, and the red and black lines is Gaussian fit. (Bottom) The red line shows the ratio of fitting in top figure and the black dot with error bar show the relative statistic error of DIO measurement spectrum, where the values of all black dot are the same.

6.2 Accidental coincidence background

In this experiment, the average number of hits per trigger in a MWPC is about 20. This makes a background which imitates a particle track by accidental coincidence. The same situation is expected in the μ-e data taking. Therefore, the procedure to evaluate the effect of the accidental coincidence is developed. The details of it is described in this section.

6.2.1 Estimation of the accidental tracking rate

In general, random pulse of detector causes the accidental coincidence. The coincidence conditions in this analysis are $|\Delta t| < w$ and $|\Delta x| < 1.5$ cm, where $\Delta t = t_m - t_f$, $\Delta x = x_m - x_f$, $w = 50$ ns is the half width of coincidence time window, (t_m, x_m) are time and position of measured hit, and (t_f, x_f) are these of track fitting. Note that the hit position in Y-plane does not affect to the momentum so that accidental hit only in X-plane is considered in this chapter. Figure 6.7 shows a conceptual illustration of an expected histogram of the time difference Δt with $|\Delta x| < 1.5$ cm. It shows that the random pulse with constant hit rate can be a background when a particle passes a detector without inducing a pulse.

We evaluate a probability P of accidental background in the case that one accidental hit on any MWPC is included in a track. The probability P can be calculated by using the probabilities p_i of an accidental hit appeared in the coincidence time window of WCi X-plane as

$$P = \sum_{k=0}^{3} p_k. \tag{6.2}$$

6.2.2 Background hit rate

In order to evaluate the probabilities p_i, the background hit rate was analyzed with 3-MWPC tracking. The random pulses generally independent from the hit times of real pulses so that they distribute uniformly in dx histograms. Therefore, the rate r_i of the random pulse can be estimated from the constant component outside of coincidence time window of the dx distributions shown in Figure 6.8. The probabilities p_i is explained as

$$p_i = 2wr_i(1 - \epsilon_i). \tag{6.3}$$

127

where ϵ_i is the detection efficiency of WCi estimated in Section 4.6 and shown in Table 4.4. The results are summarized in Table 6.1 and the probability P is 0.4 %. Note that the cases that a track contains two or more accidental hits can be negligible because $p_i \simeq O(10^{-3})$ and the probability with two accidental hits is approximate to $p_i^2 \simeq O(10^{-6})$.
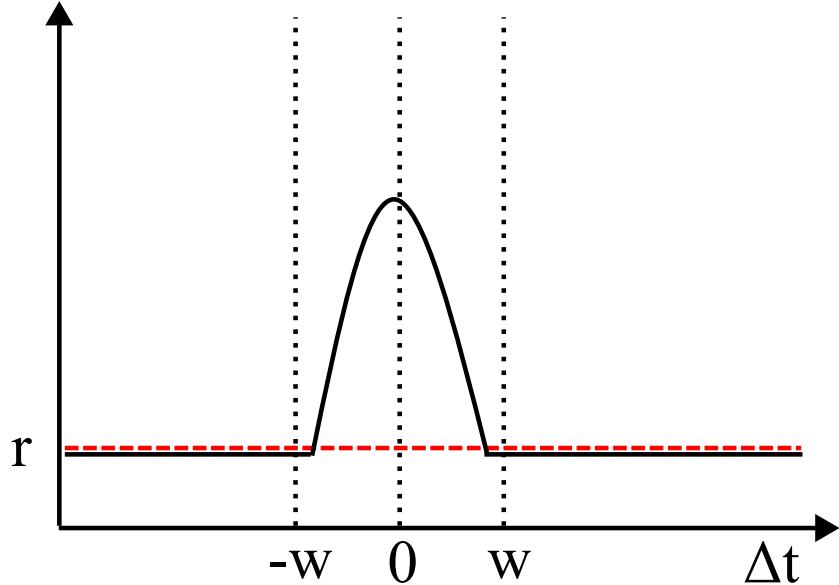
Figure 6.7: The schematic of Δt distribution.

Table 6.1: The parameters for accidental track analysis.

	r_i (/ns)	ϵ_i	p_i
WC0	1.7×10^{-4}	0.92	1.48×10^{-3}
WC1	1.6×10^{-4}	0.96	0.67×10^{-3}
WC2	0.8×10^{-4}	0.92	0.70×10^{-3}
WC3	1.4×10^{-4}	0.90	1.56×10^{-3}

6.2.3   Analysis

Figure 6.9 shows the momentum spectrum of accidental track (accidental spectrum) by accidental coincidence tracking, which is the tracking with

128
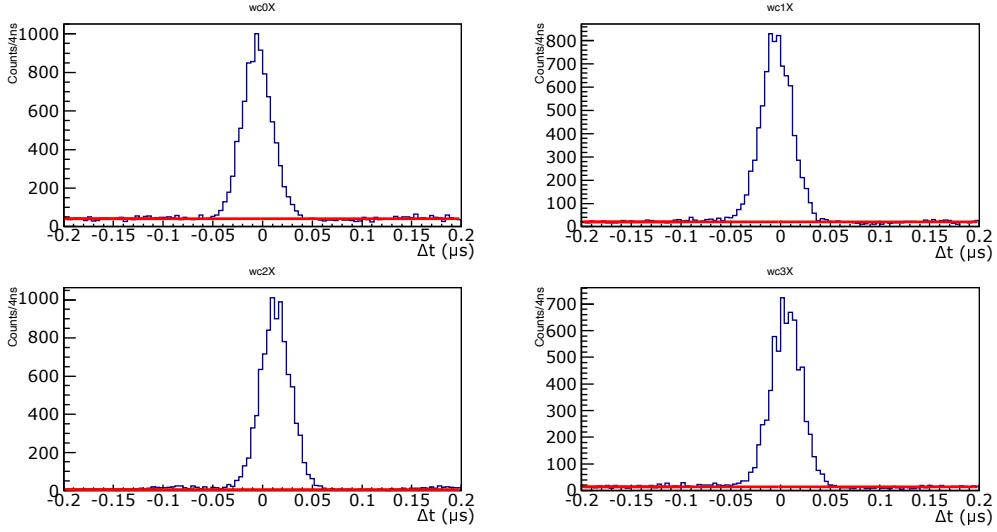
Figure 6.8: The Δt distribution for X-plane.

delaying a coincidence window of any one detector as shown in Figure 6.10. Due to the way of estimation, four accidental spectrum can be obtained. They are merged according to p_i into one histogram shown in Figure 6.9. The accidental spectrum is smaller than the statistic error of the DIO spectrum in the current data. The same procedure can be applied for the main data to evaluate the accidental coincidence effect. As long as the number of hits per single chamber in a single trigger is smaller than a few ten, the expected distortion to the spectrum shape will be only a level of 5 %.

6.3 Error from geometrical uncertainty of MW-PCs

The position of each detector and the sector magnet had been measured with the error ∼0.1 mm for X and Y direction as mentioned in Chapter 3. In this section, the effect to the momentum distribution from the detectors geometrical position uncertainty evaluated by MC simulation is discussed.
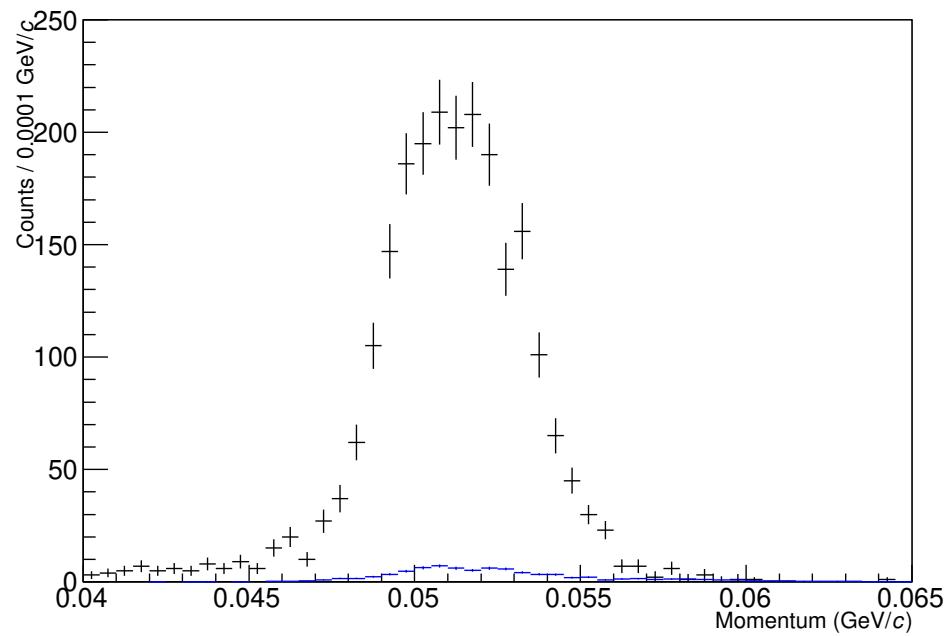
Figure 6.9: The momentum distribution of normal tracking (black line) and accidental coincidence tracking (blue line).
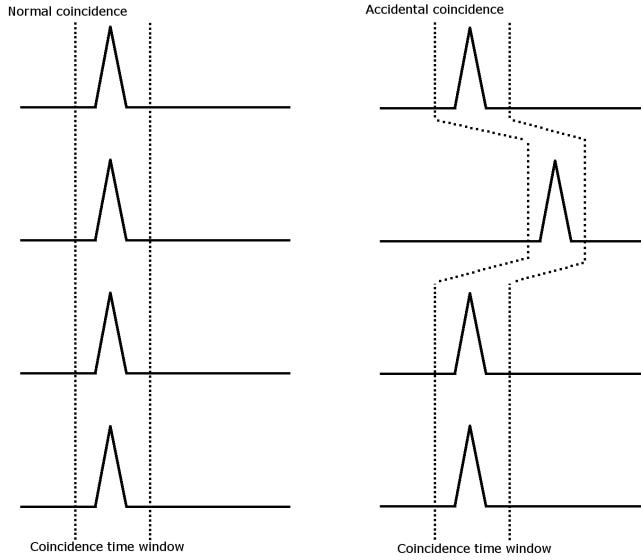
Figure 6.10: The method of accidental background analysis.

6.3.1 Error estimation

The geometry of the detectors had been measured based on the center line of the sector magnet. The laser was projected across the bottom of the magnet and the base of MWPC are used as a guide line indicating the magnet axis. The guide line was adjusted to as parallel to the axis as possible by measurement of the distance between the laser and the points signified by the markers which indicate the axis on the magnet as shown in Figure 6.11. The d_1 and d_2 in Figure 6.11 also include the measurement error δ so that the error of the geometrical position of the MWPCs were multiplied proportional to the distance from the magnets. The position errors of MWPCs δ_i (i=0, 1, 2, 3; the number of WC0-3) derived from measurement error of d_1 and d_2 are calculated as Table 6.2.

6.3.2 Modeling

In order to evaluate the effect to momentum spectrum by the MWPC position uncertainty, the MC simulation data was analyzed with MWPC position shifted slightly in the tracking analysis, i.e. any one MWPC's X-coordinate was independently changed from the original position at the tracking step.

131
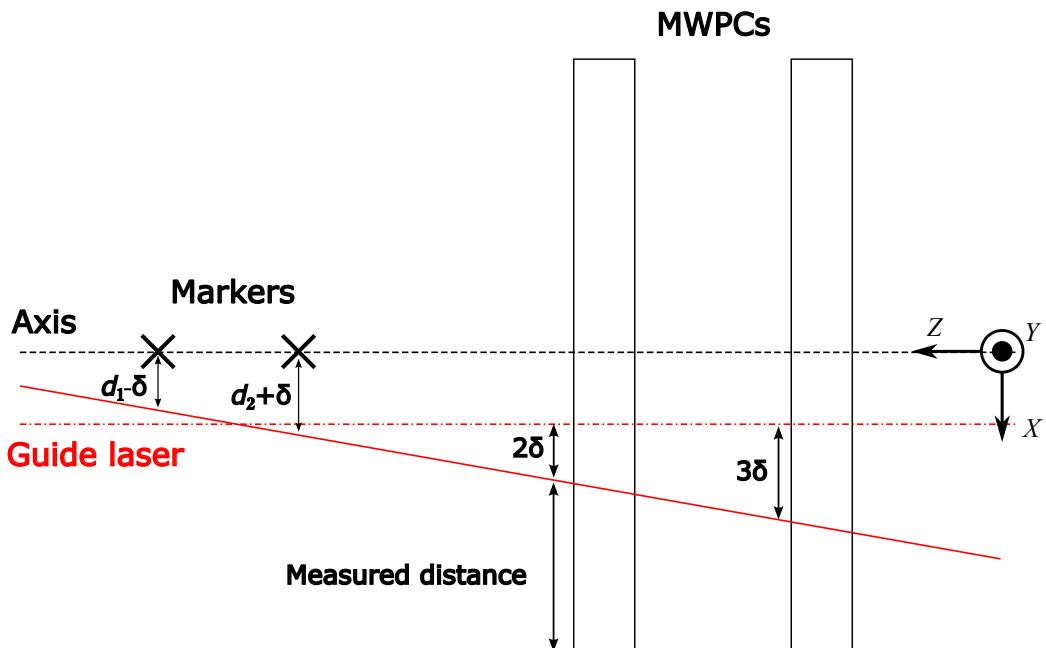
Figure 6.11: The schematic view of the MWPC position measurement and evaluation of the error of the MWPC position measurement. The distance between the guide laser and markers d_1 and d_2, and the laser is placed where d_1 equals to d_2. The δ in the figure is the measurement error $\delta \sim 0.1$ mm.

Table 6.2: The error at each detector derived from the center line measurement error $\delta = 0.1$ mm.

Plane	Error	Value
WC0	δ_0	0.35 mm
WC1	δ_1	0.22 mm
WC2	δ_2	0.19 mm
WC3	δ_3	0.31 mm

Then the momentum spectrum $N_i(x + \Delta x_i; p)$ with the position shifted by Δx_i was divided by the spectrum $N_i(x; p)$ of the original position. The result spectra for the WC0 are shown in Figure 6.12 with $\Delta x_i = -0.5$ mm. They are well fitted from 40 MeV/c to 50 MeV/c by a liner function

$$\frac{N_i(x + \Delta x_i; p)}{N_i(x; p)} = a_i(\Delta x_i)(p - 45 \text{ MeV}/c) + b, \tag{6.4}$$

where the constant term b only implies overall reduction of efficiency. The component distorting the spectrum is most important for this estimation so that the constant term b is ignored. The slope $a_i(\Delta x_i)$ for each Δx_i is shown in Figure 6.13. where $a_i(\Delta x_i)$ is fitted by linear function as below;

$$a_i(\Delta x_i) = a_i' \times \Delta x_i. \tag{6.5}$$

The values of a_i' are shown in Table 6.3.

The Δx_i and a_i for each MWPC are considered to be Gaussian distribution $G(\mu, \sigma^2)$ with a mean μ and a standard deviation σ and to be independent of each other as below;

$$\Delta x_i = G(0, \delta_i^2) \tag{6.6}$$
$$a_i = G(0, \sigma_i^2), \text{ where } \sigma_i = a_i' \delta_i. \tag{6.7}$$

Four independent Gaussian-distributed parameters a_i are able to be merged into a variable a_{merged} as

$$a_{\text{merged}} = a_1 + a_2 + a_3 + a_4$$
$$= G(0, \sigma_{\text{merged}}^2), \tag{6.8}$$

where the deviation σ_{merged} of a_{merged} is

$$\sigma_{\mathrm{merged}} = \sqrt{\frac{1}{\frac{1}{\sigma_1^2} + \frac{1}{\sigma_2^2} + \frac{1}{\sigma_3^2} + \frac{1}{\sigma_4^2}}} = 0.71 \ /\mathrm{GeV}/c. \tag{6.9}$$

As a result, the distortion function $D(p)$ of a momentum spectrum can be evaluated as

$$D(p) = a_{\mathrm{merged}}(p - 45 \ \mathrm{MeV}) + 1. \tag{6.10}$$
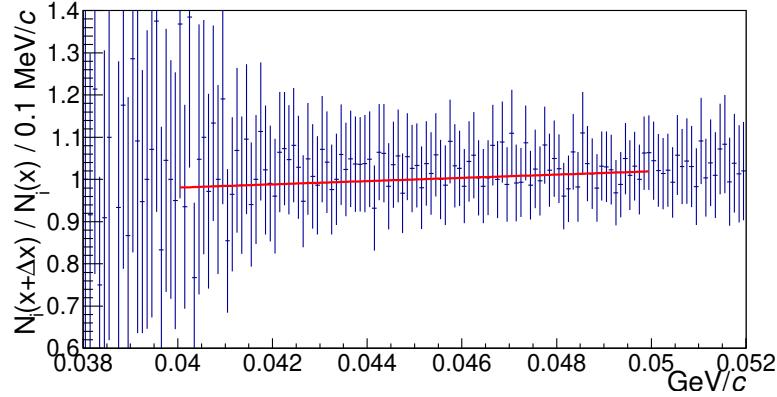
Figure 6.12: A typical plots of $N_i(x + \Delta x; p)/N_i(x; p)$ for WC0 with $\Delta x = -0.5$ mm.

Table 6.3: The values of a_i'.

	a_i' /(mm MeV/c)	σ_i mm
WC0	-7.45	2.6
WC1	10.7	2.4
WC2	-7.25	1.4
WC3	3.03	0.94
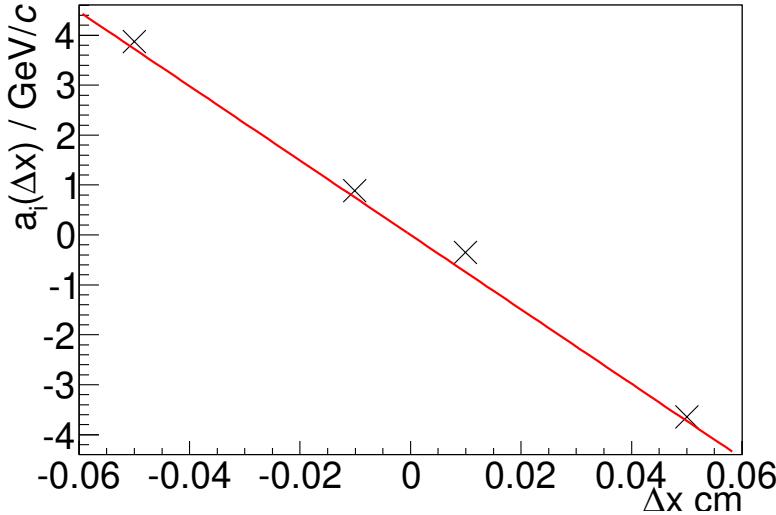
Figure 6.13: The plots of $a(\Delta x)$ fitted by a liner function for WC0.

6.3.3 Evaluation

The four independent errors of the detectors' position are merged into one parameter a_{merged}. In order to evaluate the distortion of the momentum spectrum, the relative statistic error of the momentum spectrum of the μ^+ 45 MeV/c data was compared with

$$D^+ = a^+_{\mathrm{merged}}(p - 45 \text{ MeV}) + 1 \text{ and} \tag{6.11}$$

$$D^- = a^-_{\mathrm{merged}}(p - 45 \text{ MeV}) + 1, \tag{6.12}$$

where $a^{\pm}_{\mathrm{merged}} = \pm 1\sigma_{\mathrm{merged}}$ as shown in Figure 6.14. The effect from $D(p)$ is $< 0.5 \%$ and smaller than the statistical error by $O(10^{-1})$ in this data. For H-Line analysis, the procedure explained in this section can be applied.

6.4 Summary

I validated the potential systematic errors and developed analysis techniques for them. The low statistics of this experiment may make them negligible, though these methods themselves can also be applied to the experiment at H-Line.
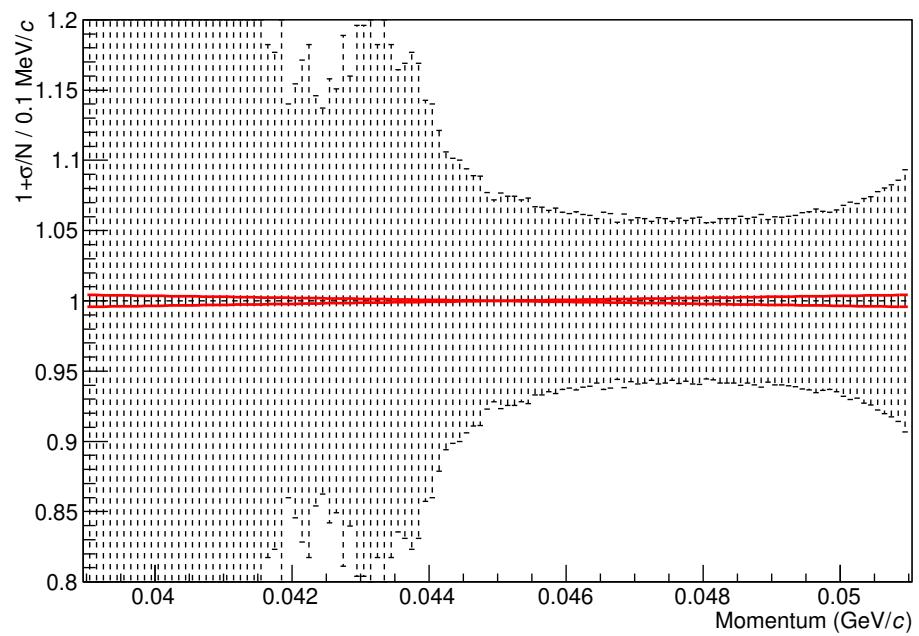
Figure 6.14: The relative statistic error of 45 MeV/c momentum spectrum of measured data (broken line) and $D^{\pm}$ (red).

The magnetic field distribution of PACMAN is totally different from that of SBM that can be measured only in a portion of its entrance and exit. The PACMAN electromagnet has a simpler structure than SBM so that continuous measurements of its magnetic field are possible, and it had done. It is considered that the modification of field map of PACMAN by field measurement is much easier than that of SBM.

The methodology of accidental coincidence analysis can be directly applied to H-Line measurements. It should be noted that the preamplifier currently in use exhibits an improved time-dependent detection efficiency compared to the one employed in this analysis. Consequently, an overall enhancement in detection efficiency is anticipated, leading to the further suppression of accidental coincidence.

The geometry of the MWPC in this experiment differs from the experimental setup in the H-Line; however, it can be estimated using a similar approach. Assuming a deviation of a similar magnitude to that of this experiment, the discrepancy is expected to be below 0.5%, and it can be neglected in bins with fewer than 40000 events when compared to statistical errors. In the case of μ-e conversion measurement, the signal region may not have a significant number of hits.

Chapter 7

Discussions and Conclusion

7.1 Gas gain fluctuation

As mentioned in Section 4.3.3, the time distribution of reconstructed tracks appears to fluctuate with baseline variations. If indeed the MWPC gain exhibits time dependence, it would be necessary to introduce a new calibration method beyond the current gas gain calibration implemented on a run-by-run basis. Calibrating the gas gain along the time axis could potentially resolve this issue.

On the other hand, reports of bench tests [3] indicate a high stability of detection efficiency over time as mentioned in Section 2.3.2, which contradicts the analysis in this paper. Currently, it remains unclear whether the time dependence originates from software or hardware. Therefore, in the μ-e conversion experiment, attention should be paid to the hit time distribution. It is desirable to introduce the new calibration method mentioned above and conduct further investigation into the underlying causes.

7.2 Tracking algorithm

As seen in the pull function distribution, the uncertainty in the track fitting remains to be clarified but we suspect an issue in the tracking algorithm. The Kalman filtering is usually applied in the experiments containing large number of measurement points. In DeeMe experiment, however, the number of the measurement planes is just 6-8. It will be required to install straight-line or general broken lines (GBL) algorithm into the Genfit framework.

Although by using Kalman filter, not best algorithm, we have confirmed the Michel-like and DIO-like momentum spectrum. The tracking-algorithm can be improved independently from the data taking process and the waveform analysis so that the detectors, DAQ system, and the analysis framework are expected to be able to be utilized in the H-Line experiment without any other improvement for the moment.

7.3   Systematic errors

We discussed about the systematic error from geometrical uncertainty in Section 6.3 and the verification was focused solely on the distortion of the spectrum. However, in the H-Line measurement, it is considered that the DIO electrons at the endpoint may contaminate to the signal region. Addressing this concern could involve conducting a similar analysis on Michel edge measurement data to evaluate the shift of the edge. In any case, considering the slope at 45 MeV/c, it is anticipated that the deviation will not exceed the momentum resolution.

We also suspected that one of the reason that leads the disagreement of the acceptance distribution between MC and real data is the particles extracted from the SBM by scattered on the walls both inside and outside the orbit. In H-Line experiment, these particles are expected to be reduced with the PACMAN magnet because of its structure. However, acknowledging the possibility without complete certainty, it is considered to place veto counters in regions where particle scattering.

7.4   Majoron emission in orbit

If lepton number is spontaneously broken globally, the associated Goldstone boson, Majoron (J), appears. If J exists, it can be observed by using muon decay as

$$\mu \rightarrow e + J. \tag{7.1}$$

The muon bound in orbit of an atom decays

$$\mu^- + (A, Z) \rightarrow e^- + J + (A, Z) \tag{7.2}$$

and the momentum of the emitted electron can reach $E_{\mu e}$. The momentum distribution of the emitted electron is shown in Figure 7.1[40]. Therefore,

the comparison of the measured and theoretical DIO spectrum can give limit to this majoron emission in orbit (MEIO) process. Current upper limit of MEIO is given by TWIST experiment as 8.4×10^{-6} for Al [41].

We tried to obtain the limit for MEIO by comparison of measured and MC-generated DIO spectrum. Figure 7.2 shows the distribution of these difference. As a result of this analysis, we obtained the limit for MEIO as

$$B(\mu + C \rightarrow e + J + C) < 0.07. \tag{7.3}$$
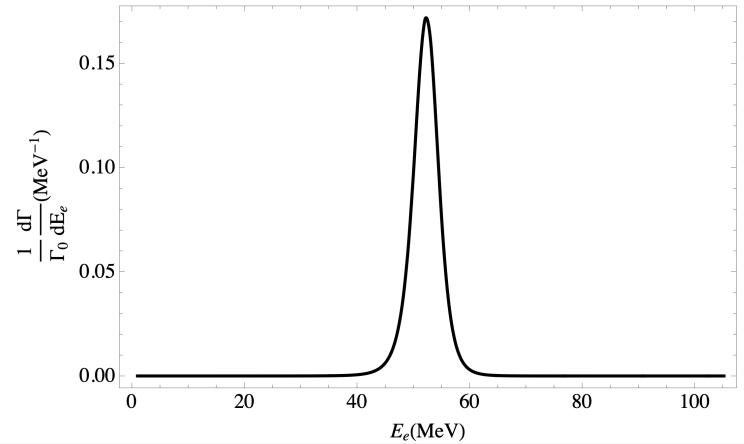
Figure 7.1: The MEIO spectrum for Al [40].

7.5 Conclusion

The μ-e conversion is a good probe of the new physics beyond the SM. DeeMe is an experiment to search the μ-e conversion in J-PARC MLF.

We developed the burst-tolerant MWPCs to avoid saturation of the detector caused by the prompt burst electron. After the development has finished successfully, we have conducted an experiment to confirm that the detectors work as a spectrometer for the DeeMe experiment. As a result, the developed MWPCs and the DAQ system have worked well.

The oscillated baseline caused by HV switching was suppressed by the most frequent waveform and signals in the waveform including baseline oscillation can be found by the waveform analysis. In addition, the particle tracks can be reconstructed by Genfit's Kalman-filter algorithm. The problem in
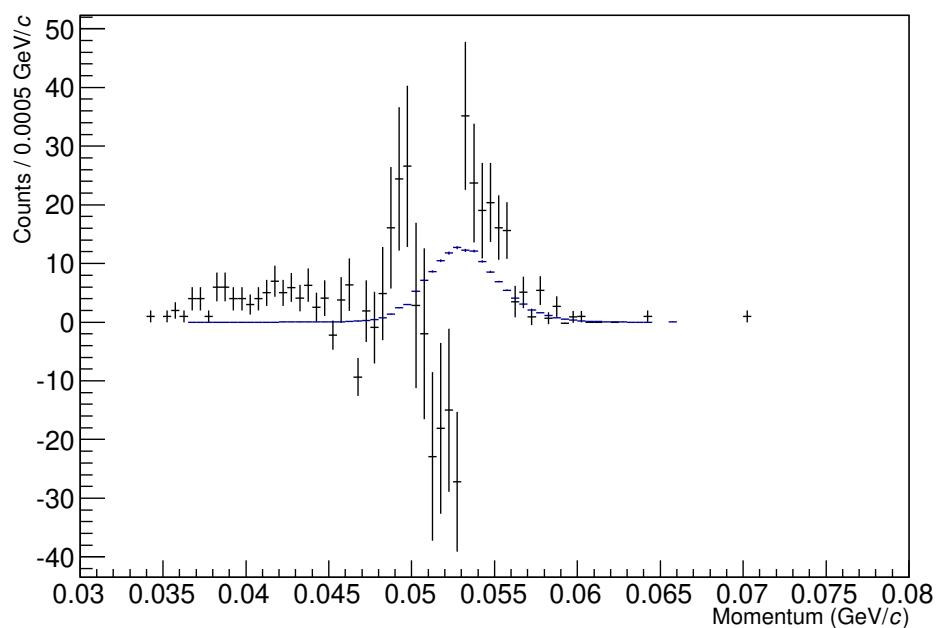
Figure 7.2: The measured DIO spectrum subtracted MC spectrum from (black with error bar) and the MEIO spectrum (blue), where the MEIO spectrum is modified the acceptance of our spectrometer and the MEIO spectrum for Al atom is used.

transportation between WC1 and WC2 was resolved by a dummy plane at the center of the bending corner. As a result, we obtained particle tracks from recorded waveforms without event trigger detectors. It is expected to realize the data taking including large hit rate of prompt burst at H-Line. The 3WC tracking also works at a certain level to obtain the information of the dependence on hit position on the detectors.

The momentum spectrum of DIO electron have been obtained for the first time. The reliability of the theoretical DIO spectrum for graphite, whose tail will be utilized to evaluate the yield of muonic atoms in the H-Line experiment, has been greatly enhanced.

The differences of the setup between this experiment and the μ-e conversion measurement in H-Line can be summarized in two points: (1) the spectrometer magnet, and (2) the sources of electrons. The differences in the spectrometer magnet lead to variations in acceptance and corresponding systematic errors. In this study, the use of the SBM limited the magnetic field measurements to specific regions and left some concerns, such as the scattering by the return yoke, unresolved. However, the magnet to be used in the H-Line has a simpler rectangular pole, which is expected to result in smaller systematic errors. Regarding the incident beam, in this study, decay electrons emitted from the target were measured directly, while in the H-Line experiment, the decay electrons will be transported through the beamline before measurement. As a result, in the H-Line, in addition to the detector acceptance, there will also be acceptance effects due to the beamline, which will require evaluation using MC simulations. On the other hand, the detectors WC0-3, DAQ system, and triggers will be the same in both experiments. Therefore, the developed analysis system, including waveform analysis, momentum reconstruction, and detector evaluation by 3WC tracking, will be the same with this study.

For momentum analysis, momentum calibration using the Michel spectrum will be also performed in the H-Line. In this analysis, calibration was performed by comparing only the shape of the momentum distribution with the MC, using relative scaling. However, in the H-Line experiment, the yield of muonic atoms is crucial, so absolute scaling will be necessary. This further emphasizes the importance of MC simulations for the electrons transported through the H-Line.

Bibliography

[1] R. Watanabe, M. Fukui, H. Ohtsubo, and M. Morita. Angular Distribution of Electrons in Bound Muon Decay. *Prog. Theor. Phys.*, 78:114–122, 1987.

[2] A. Grossheim, R. Bayes, J. F. Bueno, P. Depommier, W. Faszer, M. C. Fujiwara, C. A. Gagliardi, D. R. Gill, P. Gumplinger, M. D. Hasinoff, R. S. Henderson, A. Hillairet, J. Hu, D. D. Koetke, G. M. Marshall, E. L. Mathie, R. E. Mischke, K. Olchanski, A. Olin, R. Openshaw, J.-M. Poutissou, R. Poutissou, V. Selivanov, G. Sheffer, B. Shin, T. D. S. Stanislaus, R. Tacik, and R. E. Tribble. Decay of negative muons bound in ^{27}Al. *Phys. Rev. D*, 80:052012, Sep 2009.

[3] N. Teshima et al. Development of a multiwire proportional chamber with good tolerance to burst hits. *Nucl. Instrum. Meth. A*, 999:165228, 2021.

[4] B. Pontecorvo. Inverse beta processes and nonconservation of lepton charge. *Zh. Eksp. Teor. Fiz.*, 34:247, 1957.

[5] Ziro Maki, Masami Nakagawa, and Shoichi Sakata. Remarks on the Unified Model of Elementary Particles. *Progress of Theoretical Physics*, 28(5):870–880, 11 1962.

[6] S. T. Petcov. The Processes $\mu \rightarrow e + \gamma, \mu \rightarrow e + \overline{e}, \nu' \rightarrow \nu + \gamma$ in the Weinberg-Salam Model with Neutrino Mixing. *Sov. J. Nucl. Phys.*, 25:340, 1977. [Erratum: Sov.J.Nucl.Phys. 25, 698 (1977), Erratum: Yad.Fiz. 25, 1336 (1977)].

[7] S.M. Bilenky, S.T. Petcov, and B. Pontecorvo. Lepton mixing, $\mu \rightarrow e + \gamma$ decay and neutrino oscillations. *Physics Letters B*, 67(3):309 – 312, 1977.

[8] W.J. Marciano and A.I. Sanda. Exotic decays of the muon and heavy leptons in gauge theories. *Physics Letters B*, 67(3):303–305, 1977.

[9] Lorenzo Calibbi and Giovanni Signorelli. Charged Lepton Flavour Violation: An Experimental and Theoretical Introduction. *Riv. Nuovo Cim.*, 41(2):71–174, 2018.

[10] Yoshitaka Kuno and Yasuhiro Okada. Muon decay and physics beyond the standard model. *Rev. Mod. Phys.*, 73:151–202, 2001.

[11] Toshinori Mori. Final Results of the MEG Experiment. *Nuovo Cim. C*, 39(4):325, 2017.

[12] K. Afanaciev et al. A search for $\mu^+ \to e^+\gamma$ with the first dataset of the MEG II experiment. 10 2023.

[13] Wilhelm H. Bertl et al. Search for the Decay $\mu^+ \to e^+e^+e^-$. *Nucl. Phys. B*, 260:1–31, 1985.

[14] Technical design of the phase i mu3e experiment. *Nuclear Instruments and Methods in Physics Research Section A: Accelerators, Spectrometers, Detectors and Associated Equipment*, 1014:165679, 2021.

[15] Wilhelm H. Bertl et al. A Search for muon to electron conversion in muonic gold. *Eur. Phys. J. C*, 47:337–346, 2006.

[16] C. Dohmen et al. Test of lepton flavor conservation in mu —> e conversion on titanium. *Phys. Lett. B*, 317:631–636, 1993.

[17] S. Ahmad et al. Search for Muon - Electron and Muon - Positron Conversion. *Phys. Rev. D*, 38:2102, 1988.

[18] Manabu Moritsu. Search for Muon-to-Electron Conversion with the COMET Experiment †. *Universe*, 8(4):196, 2022.

[19] Stefano Miscetti. Status of the Mu2e experiment at Fermilab. *EPJ Web Conf.*, 234:01010, 2020.

[20] Stefano Di Falco. The Mu2e Experiment. *Moscow Univ. Phys. Bull.*, 77(2):108–111, 2022.

[21] O. Shanker. High-energy electrons from bound-muon decay. *Phys. Rev. D*, 25:1847–1853, Apr 1982.

[22] Andrzej Czarnecki, Xavier Garcia i Tormo, and William J. Marciano. Muon decay in orbit: spectrum of high-energy electrons. *Phys. Rev. D*, 84:013006, 2011.

[23] Andrzej Czarnecki, Matthew Dowling, Xavier Garcia i Tormo, William J. Marciano, and Robert Szafron. Michel decay spectrum for a muon bound to a nucleus. *Phys. Rev. D*, 90(9):093002, 2014.

[24] Kazami Yamamoto, Michikazu Kinsho, Naoki Hayashi, Pranab Kumar Saha, Fumihiko Tamura, Masanobu Yamamoto, Norio Tani, Tomohiro Takayanagi, Junichiro Kamiya, Yoshihiro Shobuda, Masahiro Yoshimoto, Hiroyuki Harada, Hiroki Takahashi, Yasuhiro Watanabe, Kota Okabe, Masahiro Nomura, Taihei Shimada, Takamitsu Nakanoya, Ayato Ono, Katsuhiro Moriya, Yoshio Yamazaki, Kazuaki Suganuma, Kosuke Fujirai, Nobuhiro Kikuzawa, Shin-Ichiro Meigo, Motoki Ooi, Shuichiro Hatakeyama, Tomohito Togashi, Kaoru Wada, Hideaki Hotchi, Masahito Yoshii, Chihiro Ohmori, Takeshi Toyama, Kenichirou Satou, Yoshiro Irie, Tomoaki Ueno, Koki Horino, Toru Yanagibashi, Riuji Saeki, Atsushi Sato, Osamu Takeda, Masato Kawase, Takahiro Suzuki, Kazuhiko Watanabe, Tatsuya Ishiyama, Shinpei Fukuta, Yuki Sawabe, Yuichi Ito, Yuko Kato, Kazuo Hasegawa, Hiromitsu Suzuki, and Fumiaki Noda. Design and actual performance of j-parc 3 gev rapid cycling synchrotron for high-intensity operation. *Journal of Nuclear Science and Technology*, 59(9):1174–1205, 2022.

[25] Wataru Higemoto, Ryosuke Kadono, Naritoshi Kawamura, Akihiro Koda, Kenji M. Kojima, Shunsuke Makimura, Shiro Matoba, Yasuhiro Miyake, Koichiro Shimomura, and Patrick Strasser. Materials and life science experimental facility at the japan proton accelerator research complex iv: The muon facility. *Quantum Beam Science*, 1(1), 2017.

[26] K. Shimomura. Muonium in j-parc; from fundamental to application. *Hyperfine Interactions*, 233(1):89–95, 2015.

[27] M. Abe et al. A New Approach for Measuring the Muon Anomalous Magnetic Moment and Electric Dipole Moment. *PTEP*, 2019(5):053C02, 2019.

[28] Naritoshi Kawamura, Masaharu Aoki, Jacob Doornbos, Tsutomu Mibe, Yasuhiro Miyake, Fumiaki Morimoto, Yohei Nakatsugawa, Masashi Otani, Naohito Saito, Yoshihiro Seiya, Koichiro Shimomura, Akihisa Toyoda, and Takayuki Yamazaki. New concept for a large-acceptance general-purpose muon beamline. *Progress of Theoretical and Experimental Physics*, 2018(11), 11 2018. 113G01.

[29] Yuko Furuya. Magnetic field analysis and performance study of the spectrometer magnet used in the deeme experiment searching for muon-to-electron conversions.

[30] Midas.

[31] F. Morimoto. ミューオン・電子転換過程探索実験 deeme に おける 単一事象感度およびミューオン decay-in-orbit バックグラウンドの評 価 (estimation of the single-event sensitivity and the muon decay-in-orbit background for the deeme experiment searching for muon-electron conversions).

[32] Takuya Takahashi. μ - e 転換過程探索実験 deeme に用いられる 高レー ト耐性 mwpc の充填ガス最適化および 単一事象感度の評価 (optimization of filling gas for mwpcs with high rate tolerance and estimation of the single-event sensitivity for the deeme experiment searching for muon-electron conversions).

[33] Kawamura N Koda A Kojima KM Makimura S Matoba S Miyake Y Shimomura K Strasser P. Higemoto W, Kadono R. Materials and life science experimental facility at the japan proton acc. *Quantum Beam Sci.*, 1(11), 2017.

[34] D.F. Measday. The nuclear physics of muon capture. *Physics Reports*, 354(4):243 – 409, 2001.

[35] Opera-3D. http://operafea.com.

[36] H. Yoshinaka. Calibration of readout electronics for deeme experiment by target irradiation data by j-parc muon beam.

[37] J. Chiba, H. Iwasaki, T. Kageyama, S. Kuribayashi, K. Nakamura, T. Sumiyoshi, and T. Takeda. Study of position resolution for cathode readout mwpc with measurement of induced charge distribution.

Nuclear Instruments and Methods in Physics Research, 206(3):451–463, 1983.

[38] Johannes Rauch and Tobias Schlüter. GENFIT — a Generic Track-Fitting Toolkit. *J. Phys. Conf. Ser.*, 608(1):012042, 2015.

[39] http://g4beamline.muonsinc.com.

[40] Xavier Garcia i Tormo, Douglas Bryman, Andrzej Czarnecki, and Matthew Dowling. Bounds on majoron emission from muon to electron conversion experiments. *Phys. Rev. D*, 84:113010, 2011.

[41] R. Bayes. Measurement of the decay parameter ρ and a search for non-standard model decays in the muon decay spectrum. *Ph.D. thesis*, University of Victoria, 2010.